This is to certify that the

thesis entitled

Origin of the Chemical Variation in
El Valle Central, Costa Rica

presented by

Rachel Susan Hannah

has been accepted towards fulfillment
of the requirements for

MS degree in Geological Sciences

Leonard A. Wood

Major professor

Date March 30, 2000

ORIGIN OF THE CHEMICAL VARIATION IN THE VALLE CENTRAL TUFF, COSTA RICA

By

Rachel Susan Hannah

A THESIS

Submitted to
Michigan State University
in partial fulfillment of the requirements
for the degree of

MASTERS OF SCIENCE

Department of Geological Sciences

2000

ABSTRACT

ORIGIN OF THE CHEMICAL VARIATION IN THE VALLE CENTRAL TUFF, COSTA RICA

By

Rachel Susan Hannah

Costa Rican magmatism is somewhat unusual because of the occurrence of high-silica volcanic deposits in an area where a continental crust is absent. However, the ash-flow deposit of the Valle Central, Costa Rica consists in part of high-silica deposits. The Valle Central Tuff covers about 785 km^2 and has a volume of about 22 km^3. Based on analyses of pumice fragments, the tuff can be divided into three chemical groupings: a low-silica group (54-62 wt. % SiO_2), a high-silica group (63-69 wt. % SiO_2), and a mingled group (56-65 wt. % SiO_2). Different Eu/Eu*, MREE, and HREE trends in the high and low-silica groups show that these groups can not be related to each other through fractional crystallization. The low-silica magma represents a mantle melt that has undergone fractional crystallization, producing continuous variation in silica, ranging from 53 wt % to 63 wt % SiO_2. The high-silica magmas represent melting of amphibolite at the based of a thickened oceanic crust. However, based on uniform potassium enrichments and low variation of REE patterns, the high-silica magma and the low-silica magma are related, and have a common source. We suggest that the high-silica melts resulted from partial melting of a meta calc-alkaline rocks, which were similar to the low-silica group within El Valle Central Tuff. The mingled group represents the physical and chemical mixing between these two end-members.

ACKNOWLEDGEMENTS

I would never have finished (much less begun) this thesis without the help and support of many people. First and foremost, family deserves kuddos for giving me endless love and support. Mom and Dad, my sister Eleanor and her family, Drew and Shaw, my brother John and his family, Patty, Katherine and Victoria, and last-but not least- my sister Mary.. I love you all very, very much.

My friends helped with the grind of daily life. Maya Doe-Simki, Sarah Miltz, Sarah Bork, and Natalia Hernandez-Gardiol gave me plenty of hugs, kisses, and parties, (not to mention the odd romance novel) to bolster my spirits and offer distractions. Abe Cambier became a treasured dinner and travel companion, and one of my best friends. Marcin Kociuba dropped in and out for good wine and good conversation, and Ryan Birkenfield commeserated on the joys and heartaches of a geologist from afar.

And perhaps most importantly, my advisors from Michigan State University. Thomas A. Vogel taught me how to act and think like a scientist. Lina C. Patino offered endless professional advice and support. Micheal Velbel, Duncan Sibley, and Bill Cambray were always around to buy me a cup of hot chocolate. I also owe lots of gratitude for our newcomer, Gary Wiessmann, in helping me figure out what to do next.

Finally, I would like to acknowledge the National Science Foundation, the Geological Society of America, and Michigan State Honors College for providing me the funding that made this project possible.

TABLE OF CONTENTS

LIST OF TABLES

LIST OF FIGURES

regardless of silica content. The Valle Central Tuff samples plot within the range of isotopic variation seen throughout the Valle Central.

Figure 12. A. Photomicrograph of clinopyroxene phenocrysts from a black pumice clast (54 wt. % SiO_2 within the low-silica group. **B.** Photomicrograph of plagioclase phenocryst from the same sample; the pock-marked texture of the crystal is referred to as "sieve" texture. **C.** Rounded vesicules in the brown glass, especially evident in nearly aphyric samples of 62 wt. % SiO_2. In all photomicrographs, the bar scale represents 1 mm. UXP= Uncrossed polars, or plane-polarized light. XP= View using crossed polars.

Figure 13. Phenocryst contents and variations in low-silica group black pumice. Dashed lines in vertical axis indicates a change in scale.

Figure 14. A. Photomicrograph of a glomopheric clot from a white pumice clast from the high-silica group. **B.** Photomicrograph of glass from an aphyric, white pumice clast from the high-silica group. Note the stretched and collapsed vesicules within the glass. In all photomicrographs, the bar scale represents 1 mm. UXP= Uncrossed polars, or plane-polarized light. XP= View using crossed polars.

Figure 15. A. Photomicrograph of banded pumice fragments with abundant rotated and broken phenocrysts. **B.** Photomicropgraph of remnant glomopheric clot surrounded by white glass, typical of white pumice of the high-silica group, surrounded by brown glass typical of the low-silica group **C.** Photomicrograph of glass in banded pumice fragments. Note that the brown glass (59-60 wt. % SiO_2) retains well rounded vesicules while the white glass (69-70 wt. % SiO_2) has stretched and collapsed vesicules. In all views, the scale bar represents 1 mm. UXP= Uncrossed polars, or plane-polarized light. XP= View using crossed polars.

Figure 16. Ternary diagram for feldspar. Note the decrease in anorthite content of phenocrysts with increasing silica content in the whole pumice sample.

Figure 17. Pyroxene quadrilateral for the Valle Central phenocrysts. Low-silica group and high-silica group augite phenocrysts have very similar compositions. High-silica group pumice clasts have orthopyroxene. Rims on orthopyroxene crystals from mingled pumice clasts are enriched in Fs.

Figure 18. A. Plots of Fs content in pyroxene phenocrysts with silica content in whole pumice samples. The Fs content of pyroxenes in the low-silica group (55 wt.% SiO_2) is identical for clinopyroxene phenocrysts in the high-silica group (67 wt. % SiO_2). Rims from mingled pumice samples are enriched in Fs. **B.** K_d values for all clinopyroxene phenocrysts versus silica content in whole pumice samples. Some phenocrysts in black, grey, and banded pumice clasts from the low-silica group are in equilibrium with the liquid. Phenocrysts in white and light gray pumice clasts are not in equilibrium with a basaltic liquid, with K_d values well below equilibrium values of 0.22 ± .02.

Figure 19. A. Photomicrograph in plane polarized light of a cluster of orthopyroxene phenocrysts within a banded pumice fragment. **B.** Photomicrograph using backscattered electron imaging to see reaction rims around the orthopyroxene phenocrysts. The phenocryst cores are depleted in Fe and enriched in Mg compared to the phenocryst rims.

Figure 20. TAS classification of LeBas et al. (1986) for the Central American Volcanic arc, including the Valle Central Tuff. CAVZ indicates basalts, basaltic andesites, andesites, and rhyolites from CENTAM database, and from Kempter (1997). Note that the Valle Central Tuff is enriched in K compared to other volcanic products from along the Central American Volcanic arc.

Figure 21. Plots of SiO_2 vs. selected trace elements. CAVZ indicates basalts, basaltic andesites, andesites, and rhyolites from CENTAM database and from Kempter (1997). Note that El Valle Central Tuff is enriched compared to other volcanic products from along the Central American Volcanic arc.

Figure 22. A. Liquid lines of decent for batch fractional crystallization models. =Low-silica Group. =High-silica Group. **B.** Spider diagram of observed and calculated (based on multiple linear regression) for Steps A and B in A. **C.** Spider diagram of observed and calculated (based on multiple linear regression) for Step C. **D.** Spider diagram of observed and calculated (based on multiple linear regression) for Step D.

Figure 23. A. Plot of Eu/Eu* versus SiO_2. Symbols as before. Note that the low-silica group and **A.** Plot of Eu/Eu* versus SiO_2. Symbols as before. Note that the low-silica group and the high silcia group plot in two distinct trends, implying that fractional crystallization is not the controlling process on magma differentiation. Lines represent a best fit line for each group. **B.** Ce is representative of other light rare earth elements, incompatible in both the low and high silcia groups. **C.** Sm is representative of the middle rare earth elements; incompatible in the low-silica group liquid, but behaving as a more compatible element in the high-silica group liquid. **D.** Rb/Hf variation between the two groups could indicate a crustal source for the high-silica group.

Figure 24. Element ratio-ratio plots as a test for magma mixing. Symbols as before. **A and C.** Plots of Sr/Y vs Ti/P and Ta/Ti vs. Y/Sm. Ta/Ti ratios are multiplied by 1000 for easier plotting. All the banded samples fall on a hyperbola defined by mixing the high and low silica extreme compositions. **B and D.** Plots of Sr/Y vs. P/Y and Y/Sm vs. Ti/Sm. All plots support magma mingling for the Mingled group. 10C and 10D do not support magma mingling for the low or high silica group. Tic marks represent mixing increments of 20%.

Figure 25 Schematic model of the evolution of El Valle Central Tuff

INTRODUCTION

1.1 Purpose

The production of silicic magmas in island arc settings has long been an enigma. In most island arcs, high-silica igneous rocks are uncommon due to the absence of continental crust (Hildreth, 1983; Fournelle et al., 1994). However, there are some exceptions, including some regions in the Aleutians (which contains silicic rocks in the absence of continental crust; Singer et al., 1992) and Costa Rica. Abundant silicic magmas were produced in the late Miocene and Pliocene in Costa Rica and erupted as ash-flow sheets. These silicic ash-flows are exposed several thousand square kilometers in Costa Rica, yet few petrological studies have been done (Alvarado et al., 1992). One of these silicic ash-flow sheets is in the Valle Central, and is the subject of this investigation.

1.2 Background

Ash-flow tuffs are ideal in studying the origin of compositional variation in volcanic systems because they represent an instantaneous partial evacuation of a magma chamber. Therefore, any variation present in a magma chamber is preserved unaltered on the earth's surface. In any series of lava flows, the genetic relationship of the magma compositions has to be inferred, but in an ash-flow sheet there is no doubt of the original composition within the magma chamber.

The common occurrence of compositionally and mineralogically zoned ash-flow sheets provides strong evidence that large chemical, mineralogical, and thermal ranges

are common characteristics of magma bodies (for reviews see Smith, 1979; Hildreth, 1981; de Silva and Wolff, 1995; Mills et al., 1997). Much of the effort of recent studies has been to evaluate the origin and evolution of zoned magma bodies by studying the ash flow sheets. In almost all studies of zoned ash flow sheets, the inferred trend towards the top of the parental magma bodies is increasing silica, decreasing temperature and decreasing phenocryst content. Because of the effects of magma withdrawal processes (Spera et al., 1986) and topography (Valentine et al., 1992) on compositional zonation in ash flow sheets, it is not clear if the zoned ash flow sheets reflect the presence of continuous chemical gradients or discrete layers in the magma body. Any conclusions about thermal and compositional gradients in an ash-flow sheet, and subsequent inferences about the origin and evolution of a magma body, is model dependent. Workers have used models ranging from fractional crystallization of a basaltic andesite to melting of previously emplaced island arc plutons to explain high-silica rocks in an island arc setting (Sisson and Grove, 1993; Roberts and Clemens, 1993; Feeley and Davidson, 1994; Borg et. al., 1998).

Fractional crystallization models are difficult to apply to the origin of high-silica magmas because they require large amounts of fractional crystallization. For example, to produce the high-silica magma from a basaltic liquid would require 65% fractional crystallization. Cumulate rocks would be produced by such high degrees of fractional crystallization. In Costa Rica, it is difficult to test this model for young high-silica deposits, as coarse-grained cumulate products would be produced at depth within the crust and have not yet been exposed at the surface.

Several models for the origin of chemically and thermally zoned magma bodies have been presented in previous studies. Most models that involve large-scale differentiation of a homogeneous magma are generally based on sidewall crystallization (cf. Mittlefield and Miller, 1983; McBirney et al., 1985; Baker and McBirney, 1985; de Silva and Wolff, 1995). At the opposite end of the conceptual spectrum are models that involve controls by partial melting and melt extraction, which were first proposed by Marsh (1984) and expanded upon by Bergantz (1989) and Sawyer (1994). There is recent petrologic evidence, reviewed in Mills et al. (1997), that many magma bodies may have had distinct compositional groups that cannot be related by fractionation processes. Chemically distinct magma batches that are unrelated by fractionation processes can result from melting and extraction processes (Sawyer, 1994). Crystal fractionation, assimilation and magma mixing processes can subsequently modify these magma batches, and if enough time is available, the magma batches can become stratified in the magma chamber according to their densities. An extreme case of the combining of magma batches is the underplating of a silicic magma body by an independently generated mafic magma (Wiebe, 1994; Coleman et al., 1995; Metcalf et al., 1995).

Brophy et al. (1999) has proposed a model that could explain gaps in a fractional crystallization trend (such as in silica content), even though fractional crystallization is the dominant process controlling the differentiation of a magma. They propose that the calc-alkaline series might originate by fractionation near the crust-mantle boundary. As the solidification front descends through a magma body, high-silica liquids get trapped within the crystal mush behind the solidification front. As convection ceases, the crystal mush begins to behave as a solid, and fractures. High-silica magmas drain from the

interstitial boundaries of the crystals and migrate upwards, leaving behind the crystals. This process can occur several times, leaving cumulate products of crystal fractionation behind at a depth at which they seldom get exposed to the surface (such as in Costa Rica) and explaining potential gaps a fractionating trend.

Most silicic calc-alkaline rocks are associated with continental arcs with thickened continental crust and not island arc settings. In many of these continental arcs there is evidence that melting the lower crust produces felsic calc-alkaline magmas. Borg and Clynne (1998) suggested that the majority of the felsic rocks in the composite volcanic centers from the southern Cascades are due to partial melting of lower crust that is compositionally similar to the calc-alkaline basalt in the region. Roberts and Clemens (1993) have discussed the difficulty of generating high-K calc-alkaline silicic rocks from mantle sources because the K_2O content of mantle melts is too low to produce fractionation in the high-K field. However, Price et al. (1999) use a combination of melting of the lower crust and slab derived processes to explain the presence of high K rocks at Edgemont Volcano, New Zealand. Singer et al. (1992) have shown that the high-silica magmas from the Seguam volcanic center are produced by crystal fractionation in a strongly extensional environment. These studies provide a framework in which to evaluate the origin of the high-silica volcanic rocks from Valle Central Tuff.

The purpose of this study is to document and explain the chemical variation in the Valle Central Tuff, Costa Rica. Pumice samples collected from The Valle Central tuff, Costa Rica, have a distinctive chemistry and provide us with an opportunity to address the origin of a silicic magma in a mature island arc system. This study uses major and trace element data, phenocryst composition and content, and Sr and Nd isotopes from

The Valle Central Tuff to provide insights on the magma genesis of high-K, high-silica magmas in a mature island arc environment. A parallel thesis, completed by Wendy Pérez at the University of Costa Rica, investigates the physical volcanology of the Valle Central Tuff, and its possible source.

1.3 Geological Setting and extent of Silicic Volcanism in Costa Rica

Subduction of the Cocos Plate under the Caribbean Plate produces the Central American volcanic arc (e.g. DeMets et al., 1990; Figure 1). The Chorotega block includes the southern part of the Central American arc, and extends from northern Costa Rica to central Panama (de Boer et al., 1995). This part of the arc developed on oceanic crust. The mature island arc crust is approximately 35 km thick under central Costa Rica (Carr, 1984). The angle of subduction in the Chorotega block is steeper in the northwest and shallower in central Costa Rica (Protti et al., 1995). In central Costa Rica the angle of subduction is estimated to be 35°. The shallower subduction angle in central Costa Rica is due to the subduction of the Cocos Ridge. The aseismic Cocos Ridge is interpreted to contain traces of the Galapagos hot spot (Feigenson et al., 1993). It is subducted to the south of the Valle Central of Costa Rica and the north of the Panama Fault Zone (Kolarsky et al, 1995).

In Costa Rica during the Cenozoic, most silicic volcanism was of limited extent. In northwestern Costa Rica (Guanacaste volcanic belt; Figure 2) during the Plio-Pleistocene, voluminous high-silica magmas were erupted as ash-flow sheets (Bagaces, Rio Colorado, and Libera tuffs), which covered an area of 1600 km^2 and preceded the modern andesitic volcanic chain (Chiesa et al., 1992; Kussmaul et al., 1994; Kempter,

1997). These deposits were erupted from caldera sources now buried by the modern stratovolcanos (Chiesa et al., 1992; Kempter, 1997). Based on the congruency of the major and trace element data for the silicic and andesitic rocks at Rincón de la Vieja (Figure 2), Kempter (1997) suggested that the silicic rocks were dominated by crystal fractionation of a common source, perhaps by repeated fractionation and replenishment of discrete magma bodies. In central Costa Rica (Central volcanic belt; Figure 2) during the Pleistocene, silicic magmas were erupted along the western flank of Platanar volcano (Alvarado and Carr, 1993) and in the Valle Central (Fig. 2; Kussmaul et al., 1994).

The Valle Central Tuff covers about 785 km^2 and is roughly 22 km^3 in volume (Figure 3A) (Perez, in prep). The Valle Central lies in the center of Costa Rica between the Cordillera de Talamanca and the Tilaran Range. There are five volcanoes northwestern side of the tuff: Platanar (dormant), Poás (active), Barva (dormant), Irazú (active), and Turrialba (active) (Figure 3A). These volcanoes are to the northwest of the Cordillera de Talamanca and are the southernmost volcanoes of the Central American Volcanic Arc. South of these volcanoes the shallow subduction of the Cocos Ridge prevents further volcanism (Alvarado et al., 1992). Therefore, volcanic products from this area, in particular those from the Valle Central, are useful in studying the effects of a shallowly dipping subduction zone, and the possible effects of the Cocos ridge subduction on magma chemistry.

THE VALLE CENTRAL TUFF

2.1 Previous Work

This ash-flow sheet has not been intensively studied. Williams (1952) published the first work describing the overall geology of the Valle Central. He identified the ash-flow tuffs and called them "glowing avalanche deposits." Echandi (1981) renamed the ash-flow deposits as Formación Tiribí and Kussmaul and Speachman (1982) refer to the deposits as the Avalanche Ardiente formation, following Williams' work. Within this formation Echandi defined three members: (1) El Miembro Nuestro Amo, characterized by "hot mud flows" (2) El Miembro la Caja, characterized by an ash-flow tuff that is poorly welded and (3) El Miembro Electriona, characterized by highly welded ash-flow tuffs. However, Echandi presented little data on pumice types, and no chemical analysis to support his subdivisions. The formation Orotína, a fine, light blue-gray tuff appears to be the distal part of the Valle Central Tuff (Marshall et al., 1999; Perez, in prep). Tournon (1984) also found three principal facies of the ash-flow unit based on welding characteristics, color, and the nature of the pumice clasts and lithics. Kussmaul (1988) analyzed four pumice samples that were high-K andesites transitional to shoshonitic dacites with silica content ranging from 59 and 67 wt %. A sample of black glassy scoria had a basaltic andesite composition with a silica content of 54 wt %.

2.2 General Stratigraphy

Figure 3A is a geologic map that includes the Valle Central, Costa Rica, which is the most densely populated area in Costa Rica. In the Valle Central sampling is restricted to quarries and the occasional road-cut. The majority of sampling was done in active

quarries, where there was access to all different levels of the tuff; in some quarries, all layers of the tuff were exposed. In the central part of the Valle Central, the ash-flow sheet is sandwiched between two lava flows, the Intercanyon lavas and postavalanche lavas (Williams, 1952). In this study, Perez (in prep.) and I found no paleosols in any of the deposits. Echandi (1981) has recorded their presence. Ash-flow tuff deposits from the Valle Central have also been found in numerous boreholes (Echandi, 1981; Perez, in prep).

Depending on location, the Valle Central Tuff has different characteristics, based on color, size, and degree of welding of pumice clasts present in the section. These variations are not all necessarily vertical; there are lateral variations as well. Figure 3B is a simplified stratigraphic section of volcanic units in both the Valle Central and in the Cordillera Central. For the purposes of this discussion, I will distinguish between sections of the Valle Central Tuff that are in the Valle Central, and the sections that extend west and north into the Cordillera Central.

Ubiquitous throughout the Valle Central Tuff is a crystalline and lithic-rich, white ash- and pumice-fall deposit. This pumice-fall deposit ranges between 20 cm and 2 m in thickness, depending on the location (Figure 3B). The pumice-fall deposit lies over both the Intercanyon lava flows and on Tertiary sedimentary rocks (e.g. near the city of Colón), depending on the location (Figure 4). Within the Valle Central, above the white-ash fall is a massive unit, VC 3, with a dark gray matrix and abundant large black pumice clasts (the majority are 5 x 5cm, some as large as 12 x 4 cm), gray pumice, banded pumice, and minor amounts of white pumice. Banding of pumice fragments was observed both at hand sample and thin-section scale. This tuff consists of 60% matrix,

30% pumice, and 10% lithics. In some locations it is evident that there is a densely welded unit at the base, with small fiammes. This unit has been described as a "tuff lava" (Echandi, 1981); a dark-gray, welded ash-flow tuff. In some locations the tuff is approximately 80% matrix.

The tuff in the west corner of the Valle Central, closer to the Cordillera Central, has a slightly different stratigraphy. First, the white ash and pumice fall unit is not present. At the base of the tuff is a unit, VC 1, called "La Garita Tuff," with the type locality at Tajo La Garita. The La Garita tuff is lithic rich; consisting of 60-70% matrix, 25-30% pumice fragments, and 10-15% lithics. The matrix of VC 1 is gray, poorly to moderately welded, and consists of plagioclase and pyroxene phenocrysts. Pumice fragments are black, gray, banded, and white. Black pumice fragments are very large (the largest is 30 cm x 32 cm x 11 cm, the average size is 12 x 4 cm) and they appear as two types: crystal rich and crystal poor. Some of the vesicles in large black pumice fragments have partially collapsed. Most black pumice samples are angular. Gray pumice clasts are generally smaller (7 cm x 5 cm) and well rounded, by the white clasts are the smallest (the largest sample is 5 cm x 2 cm, 2 cm x 2 cm on average). This unit contains abundant fummerolic pipes, evidence that degassing took place (Figure 5). The major difference between VC 1 and VC 3 facies is that the "La Garita Tuff"-type (VC 1) has a larger percentage and size of white pumice clasts.

VC 3 extends into the northwestern part of the Central Valle, and overlies the VC 1 in most locations. However, at several locations there are lenses of fluidized pyroclastic material between the VC 1 and VC3 (Peréz, in prep). This material consists of large, rounded black and white pumice clasts, small, banded pumice, and delicate

flattened pumice fragments. These deposits are referred to as VC2. The unit can only be identified clearly in the quarries on the western edge of the Central Valley, and separates the local VC1 with the main body of the tuff, VC3. This unit shows clear evidence of fluidization behavior, with little to no matrix trapped between the pumice clasts. Black pumice clasts are both phenocryst rich and phenocryst poor. White pumice clasts are phenocryst poor. As discussed below, the pumice clasts from this unit have identical chemical variations as pumice clasts from either VC1 or VC3. For more detail on the stratigraphy of the Valle Central Tuff, see Peréz (in preparation).

There are few localities where all three units of the Valle Central tuff are present. They occur on the northwestern edge of the Valle Central (Figure 3, Table 1; Tajo Río Grande, Tajo La Garita, Tajo Río Virilla). Based on field observations, there are more white pumice clasts (high-silica pumice) at the base of the tuff deposit, in VC1. Therefore, respective to major element chemistry, the Valle Central Tuff is a zoned tuff, with the base of the flow much more silica rich than the top.

Isopleth and isopach maps (Pérez, in prep), together with stragraphical correlation, suggest that different units within the Valle Central tuff erupted in one event, or as pulses of the same event, mainly from one composite caldera located in the Barva shield volcano. The ash-flow traveled at least 80 km to the west from its source. The original area of ash-flow deposits was estimated to be about 785 km^2 (Pérez, in prep). The total volume of material erupted is equivalent to 50 km^3 (22 km^3 DRE). A major uncertainty is the volume of tephra scattered very far from the source.

2.3 Geochemistry

2.3.1 Sampling

Figure 3 is a geologic map that includes the Valle Central, Costa Rica. Samples were taken during the 1997-1998 field season (early December through January). Table 1 is a list of each sampling location. The majority of samples were from active quarries, where there was access to all levels of the tuff. Samples were taken from each unit, and as discussed earlier, these units were distinguished based on physical characteristics of the pumice within the unit. The pumice clasts sampled represented the variation among glassy pumice clasts present within each unit.

2.3.2 Methods

Whole rock major-element and selected trace-element concentrations were determined by X-ray fluorescence spectrometry (XRF) for all samples. Additional whole rock trace element and rare earth element concentrations were determined for selected samples, using laser ablation Inductively Coupled Plasma Mass Spectrometer. The major-element chemical compositions of phenocrysts were determined by electron microprobe analyses (EMPA) at Indiana University.

For whole rock chemical analyses, samples were ground with ceramic flat plate grinder, after passing them through a chipmunk. Two different techniques were used for preparation of glass disks: a high dilution fusion (HDF) and a low dilution fusion (LDF). Glass disks were made by diluting finely ground rock powder with lithium tetraborate and ammonium nitrate as an oxidizer. The proportion for HDF were 1 gm rock, 9 gms lithium tetraborate and 0.25 gms ammonium nitrate; for LDF these proportions were

3:9:0.50. Only the LDF glass disks were used for LA-ICP-MS. These materials were then mixed and fused at 1000° C in a platinum crucible for at least 30 minutes and then poured into platinum molds. Glass disks were then analyzed by XRF and LA-ICP-MS methods. Major and selected trace elements (Cr, Cu, Zr, Ba, Sr, Ni, Cu, Rb, Y, Nb, and Zn) were analyzed by XRF on a Rigaku, SMAX. Other trace elements, including the rare earth elements, were analyzed by laser ablation Inductively Coupled Plasma Mass Spectrometer (LA-ICP-MS), on a Micromass Platform ICP with a hexapole collision cell (Patino et al., 1999). The laser system is a UV laser (Cetac LSX 200).

XRF major-element analyses were reduced by the fundamental parameter data reduction method (Criss, 1980) using XRFWIN software (Omni Instruments). XRF trace-element analyses were reduced by standard linear regression techniques. For LA-ICP-MS results, calcium was used as the internal standard. Prior to any calculation the background signal was subtracted from standards and samples. The concentration of the REE in the samples was calculated based on linear regression techniques using BHVO-1, W-2, JB-2, JA-3, BIR-1 standards. Strontium and neoudymium isotopes were analyzed in a VG Sector thermal ionization mass spectrometer at Rutgers University.

2.3.3 Major Elements

Raw major element and trace element data for over 70 pumice samples of The Valle Central Tuff are listed in Table 2. Data is from only the pumice samples; whole-rock and ash-fall data are not used because they are lithic rich. Pumce clasts are hydrated, so all major element values are reported using normalized values in discussion and figures. The Valle Central Tuff pumice samples range from basaltic andesites and

trachy andesites to dacites, trachytes and trachydacites, with SiO_2 ranging from 53.9 wt. % to 68.9 wt. %. They are enriched in potassium, falling in both the high K and shoshonitic fields (Figure 6 and 20): K_2O ranges from 2.20 wt. % to 5.49 wt. %.

Samples from the Valle Central Tuff fall into three groups based on both chemistry and pumice types, as shown in a plot of K_2O and SiO_2 (Figure 6A and 6B). The first group, the "low-silica group" has silica ranging from 54 wt. % to 63 wt. %. Black and gray pumice fragments fall within the low-silica group. The second group, the "high-silica group" has silica ranging from 65 wt. % to 69 wt. %. White, gray, and collapsed pumice fragments fall within the high-silica group. The high-silica group also includes white pumice samples from the plinian ash-fall seen at the base of the ash-flow in the Valle Central. The third group, a "mingled group" has a chemistry that is intermediate between the low-silica group and the high-silica group (silica ranging from 57 wt % to 66 wt %). The mingled group contains only banded pumice samples (banding is observed both in hand-sample and thin section scales). Using these three groupings, major element oxide trends are shown in Figure 7.

There are many chemical differences between the high-silica group and the low-silica group. First, samples from the low-silica group have a large chemical variation shown by the silica spread (54 wt. % to 63 wt. % SiO_2; Figure 6). Most major element oxides have a linear relationship with silica (except MnO, which has a change of slope around 61 wt % silica). In contrast, samples from high-silica group have a small chemical variation (65 wt. % to 69 wt. % SiO_2). In the plots of SiO_2 versus K_2O, TiO_2, CaO, and MnO there are clear breaks, or "gaps", between each of the two silica groups.

Plots of SiO_2 versus MgO, Al_2O_3, P_2O_5 and FeO simply display a break in slope at the transition between the two groups (Figure 7).

With the exception of K_2O and TiO_2, the concentrations of most major element oxides decrease sharply in the high-silica group. In particular, the concentration of P_2O_5 drops below the detection limit of the XRF in the high-silica group. CaO, MgO, Al_2O_3, Fe_2O_{3T} concentrations in the high-silica group decrease by over 25% (in some cases over 50%) in comparison to concentrations in the most mafic samples of the low-silica group (Figure 7).

Pumice chemistry is directly correlated to pumice colors (Figure 6). For example, the high-silica group consists of white pumice clasts and light gray pumice clasts. In the highly welded sections of the tuff there are fiammes, which are obsidian fragments, representing collapsed white pumice fragments. The low-silica group consists of black and dark gray pumice clasts. Within black pumice clasts, as silica content increases, phenocryst content decreases. Banded pumice fragments are intermediate in chemistry between the low and high-silica groups. The thickness of the bands of black glass and white glass has a direct correlation with the average silica content of the sample.

2.3.4 Trace Elements

Trace element abundances for all pumice clasts are listed in Table 2, and variation for some elements is illustrated in Figure 8. Most trace elements show a linear relationship with silica content (Figure 8). The high-silica group is enriched in the large ion LILs (Ba, Rb) as well as Y, and Ta compared to the low-silica group. However, the middle rare earth elements (MREE) and heavy rare earth elements (HREE) do not show a

linear relationship with silica (e.g. Sm and Yb in Figure 8). The high-silica group is depleted in the MREE and HREE compared to the low-silica group.

Figure 9 is a spider diagram (normalized to primitive mantle concentrations) of selected Valle Central Tuff pumice fragments representing the high-silica group, low-silica group, and the mingled group. The overall composition of the Valle Central Tuff samples is consistent with subduction zone environments; enrichment in the large ion lithophile (LILs) and depletion in the high field strength (HFS) elements (Carr et al., 1990). The rare earth element (REE) patterns for all groups are similar (Figure 10) and show a steep pattern for light rare earth elements (LREE) and MREE with a flat HREE pattern. La/Yb for low-silica group samples ranges from 3.58 to 4.63, while La/Yb ratios for the high-silica group ranges from 3.19 to 5.19 (Figure 10).

2.3.5 Sr and Nd Isotopes

Pumice samples from the high and low-silica groups have an indistinguishable isotopic compositions (Figure 11). For the low-silica group, $^{87}Sr/^{86}Sr$ values range from 0.70372 to 0.70373. For the high-silica group, $^{87}Sr/^{86}Sr$ have a slightly larger spread, ranging from 0.70371 to 0.70375. The $^{143}Nd/^{144}Nd$ isotope ratios are equally well constrained. Values range from 0.512932 ± 32 to 0.512951 ± 9. Figure 11 is a plot comparing Sr and Nd isotopes for the Valle Central Tuff to isotopes from other volcanics in the Costa Rica. The Valle Central Tuff samples plot well within the range of isotopic variation and is consistent with the isotopic composition seen in other volcanic products (mainly lavas) from the Valle Central. However, there is a distinct difference in the isotopic composition of volcanic products from the Valle Central (including the Valle

Central Tuff) with volcanic products from northern Costa Rica, such as lavas and tuffs from Rincon de la Vieja (Figure 11).

2.3.6 Petrography

The pumice types in the Valle Central tuff (black, gray, white, and banded) low- and high-silica magmas and mingling between the two. As previously outlined in Figure 6A and 6B, black and gray pumice fragments are basaltic-andesites and trachy-andesites, and belong to the low-silica group (LeBas et al., 1986).. White and light gray pumice fragments are trachy-dacites and trachytes and belong to the high-silica group (LeBas et al., 1986). Banded pumice fragments represent the mingling between the end-members and belong to the mingled group (Figure 6A). Mineral chemistry for phenocrysts in each group are displayed in Table 3.

The black pumice fragments consist of basaltic andesites, andesites, and dacites. Sample 13-2 (Figure 12) is representative of the basaltic andesites (54.83 wt. % SiO_2). Black pumice fragments range from crystal rich to crystal poor. Phenocryst content is inversely proportional to silica content (Figure 13). Crystal-rich, low-silica black pumices are 67% glass, 28% plagioclase, 4% pyroxene, and less than 1% olivine and oxides by volume. Representative point counts are listed in Table 4. Crystal rich samples have abundant plagioclase, olivine, and orthopyroxene and clinopyroxene phenocrysts, with minor amounts of magnetite and illmenite (Figure 12A).

Crystal-poor samples have the same phase assemblages but in significantly reduced amounts. The most silica-rich black pumice (62 wt. % SiO_2) has 97% glass, 2% plagioclase, and 1% pyroxene. Oxides are present in only trace amounts, well below 1%

by volume (Table 4; Figure 13). In all low-silica group samples, pyroxene crystals are euhedral, and no glomerophyric clots are present. Plagioclase crystals have abundant melt inclusions. Vesicles within the glass of low-silica group pumice clasts are well rounded (Figure 12). Olivine phenocrysts within the low-silica group are euhedral, and are often altered to iddingsite.

The high-silica group consists dominantly of crystal poor rhyolites, from both the ash-fall and the ash-flow tuff. Figure 14 is a photomicrograph of sample 18-2, representative of the high-silica group. Most white pumice samples are nearly aphyric, with 0 to 2% crystals by volume. Phenocrysts that do occur appear within glomopheric clots (Figure 14A &B). Glomopheric clots include plagioclase, pyroxene (both clinopyroxene and orthopyroxene), and oxides (dominantly magnetite, with minor illmenite). Vesicles within the glass of high-silica group pumice clasts are collapsed and stretched (Figure 14C).

Banded pumice fragments are transitional in composition between the low and high-silica groups, and this is reflected by whole rock chemistry (Figure 7 & 8). Phenocrysts within the banded pumice clasts include plagioclase, clinopyroxene, orthopyroxene, abundant oxides, and minor olivine. The banded pumice clasts are interpreted to be the result of mingling between the high and low-silica magmas. Viscosity contrasts between the low and high-silica magmas most likely prevented mixing. Textural evidence includes flow banding of brown and white glass, and broken, rotated phenocrysts (Figure 15A and 15B).

2.3.7 Mineral Chemistry

Table 3 lists electron-microprobe analysis for phenocrysts from pumice samples.

Plagioclase. There is a large variation in the anorthite content of plagioclase phenocrysts from the Valle Central Tuff (Figure 16). The lowest silica black pumice (54 wt. % SiO_2) contains a xenocryst of plagioclase of An_{96}. Plagioclase phenocrysts in the low-silica group fall into two populations. Plagioclase phenocrysts in the low-silica group fall into two populations. Pumice clasts with a whole rock composition of 54 wt. % SiO_2 have plagioclase phenocrysts with an average content of An_{76}. Pumice clasts with a whole rock composition of 57 wt. % SiO_2 have plagioclase phenocrysts with an average content An_{50}. Plagioclase phenocrysts in the low-silica group are not strongly zoned. Variations seen in rim to core are less than 2% An. Plagioclase textures in the low-silica group vary dramatically. The majority of plagioclase phenocrysts exhibit "sieve" texture full of melt or glass inclusions (Figure 12B). This texture could represent crystals that have grown very quickly, or reabsorption textures. Remaining phenocrysts are euhedral laths of plagioclase.

Sieve texture in plagioclase phenocrysts from the high-silica group is not as predominant, although present in minor amounts. Plagioclase compositions have a continuous range of compositions, and do not fall into distinct populations ($An_{34} - An_{60}$) in the high-silica group as in the low-silica group (Figure 16). As with the low-silica group, plagioclase phenocrysts in the high-silica group are not strongly zoned. Variations are less than 1.5% An for individual phenocrysts.

Alkali Feldspar. Two pumice samples, one banded, and one white pumice clast (67 wt. % SiO_2) have alkali feldspar present (sanidine), with a composition of Ab_{48} Or_{43} An_8. In both cases, the alkali feldspars are in glomopheric clots.

Clinopyroxene. All clinopyroxene phenocrysts in low-silica group samples have a very similar chemistry (Figure 17 and 18A), augites averaging a composition of Wo_{47} En_{44} Fs_9. Clinopyroxene phenocrysts are euhedral. For ferro-magnesian minerals, equilibrium can be tested by calculated an observed mineral/host lava FeO/MgO partition coefficient (K_d) and then comparing it to published K_d values. For all equilibrium calculations, it was assumed that FeO represented 0.87 of total ferric iron (Sisson and Grove, 1993). The K_d values used for comparison are 0.23 to 0.26 for augite in a basaltic andesite (Sisson and Grove, 1993). K_d values for clinopyroxene phenocrysts from the low-silica group pumices average 0.202, which is slightly low, but within the error bars for augite crystallizing from a basaltic andesite melt.

Clinopyroxene compositions in the high-silica group are remarkably similar to that of the low-silica group (Figure 18A). This is unusual, because with the large difference in silica content of the low and high-silica groups, it would be expected that the pyroxene compositions would record the whole rock variation in silica. Instead, all the clinopyroxenes from the Valle Central Tuff are tightly grouped, with a composition of $Wo_{42\text{-}46}$ $En_{43\text{-}47}$ $Fs_{8\text{-}12}$. Fs compositions do not vary with silica content (Figure 18A & B). The clinopyroxenes in the high-silica group are also out of equilibrium with a rhyolitic liquid, as compared to calculated K_D values from the literature (Mills et al., 1997).

Orthopyroxene. As expected from the olivine-out/orthopyroxene-in phase boundary, the high-silica group does contain orthopyroxene (Figure 17). Orthopyroxene

compositions are Wo_{3-6} En_{69-75} Fs_{22-29}. As previously stated, in general, phenocrysts in the banded pumice clasts do not show strong evidence for resorption. However, in one banded pumice clast (sample 16-1) there is a set of orthopyroxene phenocrysts with clear evidence for reaction rims. These can be seen using back-scattered electron images (Figure 19A and B). While the orthopyroxene cores are typical of other orthopyroxenes within the high-silica group, averaging Wo_{3-6} En_{69-75} Fs_{22-29}, the reaction rims have a higher iron content. The reaction rims have a uniform chemistry, Wo_3 En_{54} Fs_{43}.

Olivine. Only low-silica group samples have olivine phenocrysts (Fo_{70-73}) present in trace amounts.

Fe-Ti Oxides. Low-silica group pumices have minor amounts of accessory magnetite, and ilmenite. In the low-silica group there are no magnetite and ilmenite phenocrysts that share edges, and we do not have electron microprobe analysis for phenocrysts of magnetite and ilmenite in the same low-silica group pumice (thin section). Therefore, geothermometry in the low-silica group is difficult. Howeveer, in the high-silica group there are several magnetite/ilmenite pairs for which we have electron microprobe data. There is little variation in magnetite Mg/Mn ratios, but there is significant variation in illmenite Mg/Mn ratios.

Apatite. There are small apatite phenocrysts present in both the low and high-silica group pumices in trace amounts.

Glass. Glass compositions from black pumice averages 60 wt. % SiO_2. Vesicles within black (or brown) glass from black pumice clasts are always rounded and abundant (Figure 10A). Gray pumice clasts with whole pumice chemistry within the low-silica group do not have as many vesicles. Glass from high-silica group pumice clasts has 68-

70 wt. % SiO_2, again, richer in silica than the whole pumice chemistry. In contrast to the low-silica group, the vesicles in the high-silica group are collapsed and stretched (Figure 14B and 14C).

Electron microprobe analyses of the glass within the pumice fragments demonstrates that the high and low-silica groups remained chemically distinct during magma mingling. The brown glass has a silica content ranging between 59 % and 62 %, while the white glass has a silica content ranging between 68% and 71%. Even in banded pumices, the vesicles of brown glass versus white glass retain their original characteristics. Vesicles in brown glass are well rounded and abundant (Figure 12A and B) and vesicles within white glass are collapsed and stretched (Figure 14A and B).

2.3.8 Comparison with Central American Volcanic Arc

The Valle Central Tuff is distinctive when compared to lavas from the Central American Volcanic Arc. It has long been recognized that Costa Rican volcanic products have a distinct chemistry when compared to the rest of the arc, and the Valle Central Tuff is no exception (Patino, 1997; Feigenson and Carr, 1993). The CENTAM database represents lavas from throughout Central America; these lavas in turn represent Pleistocene and Quaternary evolution and arc-history from many volcanic edifices. One of the major distinctions of the Valle Central Tuff is that it has higher potassium contents than the lavas and tuffs from the entire Central American Volcanic arc (Figure 20).

While clearly enriched in silica and potassium, other major and trace element concentrations of the Valle Central Tuff samples can also be used to characterize the chemical variations of the volcanic products in the central valley of Costa Rica. The REE

elements are can be used to compare the chemistry of the Valle Central Tuff and other volcanic rocks from other parts of the volcanic arc.

For example, Nicaraguan lavas have nearly flat REE patterns (Walker et al., 1990), while those of El Salvador and northern Costa Rica are slightly enriched (Carr et al., 1990). Those of Guatemala and central Costa Rica are strongly LREE enriched (Feigenson and Carr, 1993). The samples from the Valle Central Tuff (both high and low-silica groups), are LREE enriched, which is similar to other lavas from the central valley of Costa Rica. La/Yb ratios are two to three times higher for the Valle Central Tuff than values for the rest of the arc, but similar to La/Yb values from lavas from the same area.

Another trace element ratio useful in characterizing trace element patterns is Ba/La. The Valle Central Tuff chemistry is consistent with lavas from the Central Valley in Costa Rica, which have the lowest ranges in Ba/La values recorded in Central America. While the low-silica and high-silica groups of the Valle Central Tuff have a similar chemical signature compared to other volcanic products within Central Costa Rica, they both have much higher concentrations of potassium, especially the high-silica group. Other elements, such as Zr, Rb, La, Ba, Eu, Ce, Pr, Nd, Sm, and Gd are also enriched (Figure 21).

DISCUSSION

3.1 Fractional Crystallization

Within the low-silica group, trends in major element variation are consistent with magma evolution via crystal fractionation of a magma body (i.e. Gill, 1981); MgO, FeO, and CaO abundance's decrease systematically as SiO_2 content increases, and K_2O concentration increases. There is strong negative correlation between Al_2O_3 and SiO_2 (Figure 4), especially in the low-silica group, which may be due to plagioclase fractionation. In contrast, potential fractionation trends are not as well defined for the high-silica group (Figure 4). There are no fractionation trends for the mingled group, as they represent the physical mingling of the low and high-silica group magmas.

3.1.1 Low-silica Group

The entire range of major and trace element compositions within the low-silica group can be modeled using batch fractional crystallization. These models were completed using multiple linear regression of major element oxides (Bryan et al., 1969; Wright et al., 1970). Once the amount of each crystallizing phase was determined, using the partition coefficients for trace elements listed in Table 5, we were able to determine the expected concentrations for the daughter.

For our models of crystal fractionation in the low-silica group, we assumed sample 13-2, with 55 wt. % SiO_2 and 2 wt. % K_2O to be the parental composition. Sample 13-2 has the lowest silica sample from which we have microprobe data for the mineral phase assemblages Additional evidence for using sample 13-2 is parent is that

this pumice clast includes plagioclase phenocrysts of An_{96}. Other workers have also found anorthsitic rocks as xenoltihs, at V. Arenal and V. Poás, in Costa Rica, by Cigolini et al. (1991), Cigolini (1998) and Sachs and Alvarado (1996).

Table 6 lists selected modeling runs for both major and trace elements, using steps A and B in Figure 22A. The sum of the squares of the residual in modeling runs ranged from 0.03 to 0.091, well below accepted of a Σr^2 less than 0.5. The Σr^2 values are based on major element oxides only. The fractionating phases are plagioclase (An_{73}), olivine, clinopyroxene ($Wo_{44}\,En_{47}\,Fs_9$), magnetite, and apatite. Models can reproduce the entire chemical variation within the low-silica group with 38% crystal fractionation. Plagioclase feldspar is the dominant phase crystallizing out of the liquid. Batch fractional crystallization for major elements reproduced the observed trace elements well (calculated concentrations averaged 91% of the observed concentrations), as seen in spider diagrams of calculated and observed parent rock values (Figure 22B).

3.1.2 High-silica Group

The evolution of high-silica rocks within a mature island arc environment has long been a controversy. In most island arc settings, abundant high-silica magmas are rare due to the absence of continental crust. In continental arcs, it is possible to assimilate continental crust or melt in order to achieve high proportions of silica in the melt (70 wt. %). However, in Costa Rica, which lacks a continental crust, that is not a possible mechanism for producing the high-silica group pumice fragments. There are two generally accepted models in the literature to explain the existence of high-silica magmas in calc-alkaline island arcs. The first is the fractional crystallization of basalt, or

basaltic andesite melts (Sisson and Grove, 1993; Feely and Davidson, 1994; Brophy et al., 1999). The second model to explain the origin of the high-silica group is the partial melting of previously emplaced arc-related igneous rocks (Beard and Lofgren; 1991; Roberts and Clemens, 1993). We will discuss fractional crystallization models first.

Recently, studies have proposed a combination of convection-driven crystal fractionation, solidification fronts, and liquid segregation to explain compositional gaps such as the one seen between the low- and high-silica groups in the Valle Central Tuff (Marsh, 1984; Brophy, 1999). In basaltic magma bodies, convection prevents large-scale crystal settling, which can drive magma chamber differentiation (Marsh, 1984). Therefore, other mechanisms occurring within the magma body need to explain magma differentiation.

Brophy et al. (1999) propose the following model. They state that as fractional crystallization occurs, a solidification front descends downward into the magma body. At roughly 50% crystallization of a basaltic magma, convection above the solidification ceases, although convection still occurs below the solidification front. Above the solidification front, the crystal-liquid becomes rigid, and can be fractured. If these fractures occur, they can drain evolved interstitial liquids out from the mush, that migrate upwards by buoyancy driven liquid/crystal segregation (Brophy et al., 1999). These evolved liquids represent a high-silica magma that is related to a lower silica magma by fractional crystallization. These evolved liquids can accumulate in a magma chamber, which can also be fractionated by a similar process.

To test this model, several multiple linear regressions were performed (methods described above) for both major and trace elements to see if it is possible to simulate the

evolution of the low-silica magma into a high-silica melt. It is possible to model the chemical variation of major and trace elements in the high-silica group from the low-silica group. This was done by using the most evolved low-silica sample, 990710-2 (63 wt % SiO_2) as the parent melt and fractionating it to form the high-silica group (Figure 22A, steps C and D). Fractionating phases dominantly consist of plagioclase (An_{42}), followed by clinopyroxene ($Wo_{44}\,En_{46}\,Fs_{10}$), orthopyroxene ($Wo_3\,En_{53}\,Fs_{44}$), magnetite, and illmenite, in decreasing order. The sum of the squares of residuals ranges from 0.008 to 0.085, well below accepted values (Table 5B). It is interesting to note, however, that there seem to be two possible trends that a liquid can follow when evolving from the low-silica group to the high-silica group, Steps C and D in Figure 22A. Both steps have several samples that fall along the liquid line of decent (Figure 22A).

One of the problems of using fractional crystallization models to explain the origin of high-silica magmas is the large amounts of fractionation required to attain high-silica melts. Our models are faced with this same problem, requiring over 55% crystallization of plagioclase to evolve the melt from the least silicic sample (13-2) to the most silicic sample (1-7). Results of fractionation models are listed in Table 5b and shown in Figure 22C and 22D. Another problem with our fractional crystallization models is that these results can be slightly misleading, especially in the REE plots. The spread of REE elements within both the high-silica group and the low-silica group is very small. This is because incompatible elements do not change significantly with crystal fractionation until well over 50% of a phase has crystallized out of the liquid. The amount of plagioclase fractionation required to evolve the lowest silica magma to the

highest silica magma of the Valle Central Tuff is not enough to change the concentrations of most incompatible elements (with the exception of Eu, which is discussed below).

As discussed earlier, fractional crystallization models for producing the high-silica group from the low-silica group require large amounts of plagioclase fractionation. In this scenario, as increasing amounts of plagioclase fractionate from the melt, then increasing amounts of Eu^{2+} should be partitioned into plagioclase, resulting in an inverse relationship of Eu/Eu* and SiO_2 (or any other index of fractionation). Eu anomalies can be evaluated by calculating Eu#, which is the value of Eu calculated from the linear equation of the line connecting Sm and Tb on a REE plot (Appendix C). Eu/Eu* is a measure of the Eu anomaly. Logically, then, the high-silica group should have a larger Eu/Eu* anomaly than the low-silica group. In the Valle Central Tuff, this is not the case (Figure 10).

The Eu/Eu* for the high-silica group is much smaller than would be expected if crystal fractionation is the dominant process (Figure 10). Other volcanic rhyolites, in both continental and island arcs, have Eu anomalies that are much more pronounced, indicating large degrees of plagioclase fractionation (Brophy et al., 1996). Figure 23A, a plot of Eu/Eu* vs. SiO_2, the high-silica group and the low-silica group fall in two distinct populations that can not be related simply through fractional crystallization. If the high-silica group is fractionating from the low-silica group, one would expect the linear trend of the low-silica group in this plot to continue without breaks. It does not; instead, the Eu/Eu* for the lowest high-silica group sample (sample 2-1) is higher (0.83) than that of the least-mafic low-silica group sample (sample 990713-4c, 0.71; Figure 23A). This is a

simple but powerful test to reject pure crystal fractionation as the mechanism for producing the high-silica group magma from the low-silica group magma.

3.2 Partial Melting

Whereas crystal fractionation clearly is the dominant mechanism controlling the chemical variation within the low-silica group, this is not the case for the high-silica group. A possible origin for the high-silica magma is the partial melting of a previously emplaced and metamorphosed rock (e.g. amphibolite; Beard and Lofgren,1991; Roberts and Clemens, 1993).

In many studies, Sr and Nd isotopes are used to determine source for compositionally different magma batches. For example, if the Sr and Nd isotopes for each magma are unique, this indicates these magmas have sources of different ages. In the Valle Central Tuff, the Sr and Nd isotopes for both the high and low-silica magmas are very similar (Figure 11). This implies that the low and high silica group magmas do not originate from sources of different ages. The isotopic data rejects the possibility that the high-silica magma represents a partial melt of an older oceanic crust. If it were, the $^{87}Sr/^{86}Sr$ and $^{143}Nd/^{144}Nd$ isotopes for the low and high-silica group would be very different. However, the $^{87}Sr/^{86}Sr$ and $^{143}Nd/^{144}Nd$ isotopes do not either support nor reject partial melting as a mechanism that relates the high- or low-silica magmas. The isotopic data does not reject the possibility that the high-silica magma represents a partial melt of a young oceanic crust, such as the lower Caribbean crust, where the $^{87}Sr/^{86}Sr$ and $^{143}Nd/^{144}Nd$ isotopes have not had time to evolve.

A strong argument in favor of partial melting is the behavior of the middle rare earth elements (MREE) within the high-silica magma. The light rare earth elements (LREE) such as La and Ce behave incompatibly in both the low and high-silica groups (Figure 23B). The MREE and HREE elements, from Sm through Yb, do not behave the same way in the low and high-silica groups. In the low-silica groups, the MREE behave as incompatible elements, increasing with silica content (Figure 23C). This is consistent with a magma that is undergoing fractional crystallization. However, MREE in the high-silica group are depleted, behaving as compatible elements in terms of liquid/crystal equilibrium (Figure 23C). We interpret this data to suggest that the origin of the high-silica group is separate from the origin of the low-silica group, and the two groups are not related through fractional crystallization.

Another test for the petrogenesis of the high-silica group is to evaluate Rb/Hf ratios. If there has been any involvement with older, altered crust, then a melt should have elevated Rb/Hf ratios. Crustal melts generally have higher Rb/Hf ratios than mantle melts. In Figure 23D, is evident that the Rb/Hf ratios for the low-silica group are nearly constant, while Rb/Hf ratios for the high-silica group are elevated. This would be consistent with the low-silica group evolving from a mantle melt via crystal fractionation (as discussed earlier) and a high-silica group could represent melts of an altered lower crust (Geist et al., 1998; Price et al., 1999).

Within this model, the high-silica group can be the result of one of three processes. First, that the high-silica group represents the partial melt of a young, subducted slab. Second, that either hornblende or clinopyroxene are residual phases in the partially melted source, as both clinopyroxene and hornblende are compatible with

the MREE. Third, that magma that has fractionally crystallized and has interacted with a hydrated crust. We also recognize that both of these processes could work in concert; for example, liquid from a partially melted source can accumulate, undergo minor amounts of fractional crystallization, as well as interact with hydrated country rock.

The first hypothesis is unlikely. The Y concentrations in the Valle Central Tuff are greater than 15 ppm, and the Sr/Y ratios is less than 50 ppm, suggesting that the high-silica group rhyolites are not the adakitic rhyolites of Defant and Drummand (1990). The third hypothesis is equally unlikely. There are two reasons to reject this third hypothesis. The first is based on the lack of large Eu anomalies within the high-silica group. The spread in Eu/Eu* ratios is not large. While there appears to be a slight decreasing trend of Eu/Eu* with SiO_2 (or any fractionation index) from the least silicic sample within the high-silica group (2-1) to the most silicic (3-2), it does not present convincing evidence that crystal fractionation has occurred. Second, if the high-silica group magma interacted with a hydrated crust, one would expect hydrous phases in the magma, such as amphibole. The Valle Central Tuff does not have any of these hydrous phases. It is possible that this issue can be further resolved with additional data, especially δO^{18} analysis and/or the analysis of melt inclusions.

3.3 Magma Mingling and Mixing

The high and low-silica groups erupted together in El Valle Central Tuff. Textural evidence from banded pumice clasts indicates that there were two distinct magma batches that did not mix or equilibrate *in situ*, rather, that mingling occurred during evacuation of the magma chamber and resulted in banded pumice fragments.

The chemical variation of the mingled group can be duplicated by a mixing curve between the high and low-silica group end-members. Tests for mixing were carried out by using a simple ratio-ratio plots of four separate elements. For example, Figure 24A is a plot of Sr/Y versus Ti/P, and if the mixing occurred these data should plot on a hyperbola with the end-members (low and high-silica groups) plotting on the ends of the curve. A further test is the plot of the denominators of the original ratios pairs (e.g. P/Y) plotted against one of the original ratios (e.g. Sr/Y). If the data from banded pumice clasts fall on a straight line, with the same two end-members on the previous plot, then this provides additional support that magma mixing or mingling has occurred.

These plots can also be used to test if the chemical variation of either the low- or high-silica magmas can be reproduced through homogeneous magma mixing. Figure 24B is a plot of Y/Sm versus Ta/Ti and Y/Sm vs. Ti/Sm. In these plots it is clear that while the mingled pumice fragments fall on mixing lines between the two end-members, the chemical variation in neither the low-silica or high-silica group can be explained using magma mixing. These relationships are consistent when MREE and HREE are used in the mixing plots, as the behavior of the MREE and HREE in the high-silica magma are inconsistent with mixing of the low and high-silica magma to produce these trends.

In addition, temperature differences between these two magma batches could not have been maintained for any length of time in a magma chamber (Turner and Campbell, 1986; Martin et al., 1987). Instabilities in the thermal regime makes it unlikely that the low-silica magma and the high-silica magma co-existed in the magma chamber for a long period of time.

3.4 K_2O Trends

There are many hypothesis to explain potassium enrichment in subduction derived volcanics. Early hypothesis included pressure-dependent variation in partition coefficients for concentration in slab melts (Marsh and Carmicheal, 1974), variation in the degree of slab melting with depth (Jakes and White, 1972), enrichment of K in fluids or melts by wall-rock interaction (Best, 1975), and fractional crystallization of orthopyroxene and not olivine basaltic magma at high pressure (Meen, 1987). As discussed earlier is this study, it is unlikely that The Valle Central Tuff represents a slab melt. Other, more recent, hypothesis discuss variations of the thickness of the melting column in the mantle wedge (Plank and Langmuir, 1988), variation in the degree of melting within the mantle wedge (Stern et al., 1993), and the influence of sediment derived fluids (Le Bel et al., 1985). These fluids are often enriched in "fluid-mobile" elements such as Ba, Rb, K, and Sr, and consequently influence the character of the subarc mantle (Tatsumi et al., 1986). However, low values for trace element ratios such as Ba/La and Ba/Th, make it highly unlikely that slab input have played a large role in the petrogenesis of The Valle Central Tuff magmas.

An alternative model is that partial melting of amphibolite has played a role in K-enrichments (Price et al., 1999). This would be consistent with the petrogenesis of the high-silica group through partial melting of amphibolite. Further work with melt inclusions within phenocrysts is required to investigate these models, but is not within the scope of this project.

4. Origin of the Chemical Zonation in the Valle Central Tuff

The Valle Central tuff formed from two chemically, mineralogically and thermally distinct magma batches. Basaltic-andesite and rhyolitic magmas have distinct rheological and thermal properties. Temperature differences between these two magma batches could not have been maintained for any length of time in a magma chamber (e.g. Turner and Campbell, 1986; Martin et al., 1987) and therefore the eruption occurred almost immediately after the emplacement of the separate magma batches in the chamber.

Figure 25 is a cartoon of our model. We propose that the low-silica magma represents a mantle melt that has undergone fractional crystallization, creating a continuous range of silica contents from 53 wt % to 63 wt %. Black pumice fragments are both crystal-rich and aphyric. Low-silica, phenocryst rich black pumice fragments represent the early stages of fractional crystallization.. The low-silica magma is a zoned magma, because both pumice types are co-erupted. The higher-silica (aphyric) low-silica magam has a lower liquidous temperature, thus fewer crystals. Fractional crystallization occurred through both side-wall fractional crystallization and a descending solidification front.

The high-silica magma represents a partial melt of an amphibolite. Based on uniform potassium enrichments, tight constraints on the REE values, and the isotope composition, it is clear that the high-silica magma and the low-silica magma are inter-related, although different Rb/Hf ratios suggest that they have a slightly different source. We suggest that the high-silica group originated from partially melted meta-igneous rock

(amphibolite; explaining the different Rb/Hf ratios), but with original chemical composition very similar to the low-silica group within the Valle Central Tuff.

5. CONCLUSIONS

The Valle Central Tuff is one of the most potassic and silicic calc-alkaline volcanic deposits along the Central American Volcanic Arc. Within the tuff are three chemical groups; the low-silica group, the high-silica group, and the mingled group. The low-silica group and the high-silica group represent two distinct magmas, which, based on their temperature differences, could not have evolved in the same magma chamber. The mingled group represents the physical and chemical mixing between these two magmas.

Based on comparisons with other volcanic products along the Central America Volcanic arc, it is possible to make inferences as to the mantle sources and deep crustal processes operating beneath the central valley of Costa Rica. Based on trace element ratios such as La/Yb, the mantle beneath central Costa Rica is an enriched mantle that has not been largely modified by slab input (fluids from subducted sediments; Patino et al., 1997). Potassium enrichments in the Valle Central Tuff can be accounted for by the interaction of a hydrous mafic melt with wall rocks at the base of the oceanic crust followed by incongruent melting of wall rock amphibole. This produces potassic liquids that mix with the magma and any amphibole crystallized earlier in the system is reabsorbed back into the melt.

We propose that the low-silica magma represents a mantle melt that has undergone fractional crystallization, creating a continuous range of silica contents from

53 wt % to 63 wt %. The high-silica magma represents a partial melt of an amphibolite. Based on uniform potassium enrichments and tight constraints on the REE values and REE pattern, it is clear that the high-silica magma and the low-silica magma are inter-related. We suggest that the high-silica group partially melted from amphibolite, which had original chemical characteristics very similar to the low-silica group within the Valle Central Tuff.

APPENDIX A

Tables

Table 1. Site Locations in El Valle Central Tuff

Site	West*	North*	Topographic Quandrangle	Site
1	498.3	218.3	Rio Grande	Tajo La Garita
2	527	216.9	Abra	Tajo La Roca
3			Abra	Tajo Santo Tomás
4	515.6	217.25	Abra	Tajo Santa Ana
5	515.85	217.1	Abra	Tajo Ramírez-Crexpo
6	499.3	218.5	Rio Grande	Tajo Polvorón
7	506	213.4	Rio Grande	Tajo del MOPT
8	496.4	222.35	Naranjo	Tajo Río Colorado
9	490	228.5	Naranjo	Tajo Buenos Aires
11	496.4	222.35	Naranjo	Tajo Río Colorado
13	521.6	216.8	Abra	Tajo Barreal
16	521	216.05	Abra	Tajo Electriona
17	521.5	215.9	Abra	Tajo del Virilla
18	497.1	216.05	Rio Grande	Tajo Río Grande
19	504.6	216.05	Rio Grande	Corte en Calle Vueltas
990710	498.3	218.3	Rio Grande	Tajo La Garita
990710-2	498.3	218.3	Rio Grande	Tajo La Garita
990711-3	498.3	218.3	Rio Grande	Tajo La Garita
990712-4	496.4	222.35	Naranjo	Tajo Río Colorado
990713-2	498.8	218.8	Rio Grande	Tajo La Aduana
990713-3	498.8	218.8	Rio Grande	Tajo La Aduana
990713-4	498.8	218.8	Rio Grande	Tajo La Aduana

*** Units in Lambert**

Table 2 **Major and Trace Elements**

	6-1:122197	6-2:122197	6-3:122197	6-3B:122197	6-4:122197
Color	black	light gray	black	white	black
Site	Polvorón	Polvorón	Polvorón	Polvorón	Polvorón
SiO_2 (%)	60.20	65.30	53.80	66.00	54.40
TiO_2	1.08	0.76	0.88	0.71	0.86
Al_2O_3	15.80	15.10	19.60	15.20	19.60
Fe_2O_{3T}	6.17	3.44	7.16	3.07	6.83
MnO	0.16	0.11	0.11	0.11	0.11
MgO	1.69	0.58	2.09	0.59	1.69
CaO	3.96	1.46	7.25	1.70	7.17
Na_2O	3.66	3.51	3.02	3.56	2.85
K_2O	3.28	5.29	2.28	5.42	2.20
P_2O_5	0.41	0.14	0.52	0.12	0.51
TOTAL	96.41	95.69	96.71	96.48	96.22
Cr (ppm)	3	9	11	1	17
Ni	19	20	35	15	20
Cu	8	3	90	1	83
Zn	73	58	84	56	79
Rb	90	128	55	129	63
Sr	623	311	867	276	907
Y	38	43	23	44	29
Zr	320	428	204	447	225
Nb	23	30	7	37	11
Ba	1258	1619	873	1694	836
La	-	-	-	-	-
Ce	-	-	-	-	-
Pr	-	-	-	-	-
Nd	-	-	-	-	-
Sm	-	-	-	-	-
Eu	-	-	-	-	-
Gd	-	-	-	-	-
Tb	-	-	-	-	-
Dy	-	-	-	-	-
Ho	-	-	-	-	-
Er	-	-	-	-	-
Yb	-	-	-	-	-
Lu	-	-	-	-	-
Hf	-	-	-	-	-
Ta	-	-	-	-	-
Pb	-	-	-	-	-
Th	-	-	-	-	-

Table 2 continued

	6-5:122197	6-6:122197	11-1:122397	11-3:122397	11-4:122397
Color	black	white	black	black	whole rock
Site	Polvorón	Polvorón	Río Colorado	Río Colorado	Río Colorado
SiO_2 (%)	56.70	65.80	63.00	61.30	58.10
TiO_2	0.92	0.74	1.05	1.14	1.26
Al_2O_3	19.30	15.20	15.90	16.10	17.10
Fe_2O_{3T}	6.46	3.23	4.87	5.98	8.63
MnO	0.13	0.12	0.13	0.14	0.12
MgO	1.78	0.69	0.96	1.34	1.03
CaO	6.43	1.82	2.79	3.55	4.38
Na_2O	3.80	3.54	3.18	3.10	3.90
K_2O	2.71	5.21	3.84	3.47	2.45
P_2O_5	0.48	0.13	0.27	0.35	0.61
TOTAL	98.71	96.48	95.99	96.47	97.58
Cr (ppm)	17	19	6	19	24
Ni	28	14	8	7	6
Cu	49	6	35	33	91
Zn	63	60	80	82	67
Rb	72	134	96	81	70
Sr	864	298	448	533	778
Y	31	41	44	41	31
Zr	247	444	374	327	243
Nb	15	38	27	23	16
Ba	1055	1621	1534	1392	1243
La	-	-	-	-	-
Ce	-	-	-	-	-
Pr	-	-	-	-	-
Nd	-	-	-	-	-
Sm	-	-	-	-	-
Eu	-	-	-	-	-
Gd	-	-	-	-	-
Tb	-	-	-	-	-
Dy	-	-	-	-	-
Ho	-	-	-	-	-
Er	-	-	-	-	-
Yb	-	-	-	-	-
Lu	-	-	-	-	-
Hf	-	-	-	-	-
Ta	-	-	-	-	-
Pb	-	-	-	-	-
Th	-	-	-	-	-

Table 2 continued

	11-5:122397	16-4:010298	16-6:010298	5-1:122097	7-1:122197
Color	banded	dark gray	banded	banded	banded
Site	Río Colorado	Electriona	Electriona	Ramírez-Crexpo	MOPT
SiO_2 (%)	63.90	55.10	59.60	57.80	56.80
TiO_2	1.00	0.90	1.19	1.00	0.96
Al_2O_3	16.20	18.70	16.30	17.90	20.60
Fe_2O_{3T}	4.17	7.13	6.41	6.58	6.74
MnO	0.12	0.12	0.16	0.14	0.11
MgO	1.13	2.14	1.88	2.00	0.58
CaO	2.96	6.87	4.16	5.75	5.56
Na_2O	3.80	3.26	4.24	3.98	3.77
K_2O	4.16	2.47	3.64	3.03	2.58
P_2O_5	0.22	0.54	0.44	0.53	0.54
TOTAL	97.66	97.23	98.02	98.71	98.24
Cr (ppm)	4	22	1160	BD	1
Ni	7	39	106	4	15
Cu	21	171	42	64	91
Zn	74	55	88	79	58
Rb	108	50	96	78	51
Sr	479	837	656	761	777
Y	44	30	34	30	25
Zr	369	234	319	319	270
Nb	32	17	23	19	17
Ba	1611	1079	1345	1178	1165
La	-	-	-	74.5	65.2
Ce	-	-	-	131.0	118.2
Pr	-	-	-	17.1	14.5
Nd	-	-	-	62.7	52.0
Sm	-	-	-	10.99	9.06
Eu	-	-	-	2.48	2.32
Gd	-	-	-	9.71	8.00
Tb	-	-	-	1.25	0.97
Dy	-	-	-	6.38	4.88
Ho	-	-	-	1.35	1.02
Er	-	-	-	3.73	2.83
Yb	-	-	-	3.18	2.38
Lu	-	-	-	0.50	0.36
Hf	-	-	-	-	-
Ta	-	-	-	-	-
Pb	-	-	-	-	-
Th	-	-	-	-	-

Table 2 continued

	8-1:122297	16-1:010298	16-3:010298	16-5:010298	1-2:121897
Color	banded	dark gray	black	black	black
Site	Río Colorado	Electriona	Electriona	Electriona	La Garita
SiO_2 (%)	63.70	60.90	56.40	55.20	55.60
TiO_2	1.06	0.97	0.96	0.95	1.04
Al_2O_3	16.10	17.70	19.40	19.30	19.70
Fe_2O_{3T}	5.07	5.66	6.38	7.17	7.94
MnO	0.13	0.12	0.12	0.13	0.14
MgO	1.11	1.70	2.10	2.47	2.18
CaO	2.97	4.96	6.93	7.41	5.58
Na_2O	3.71	3.88	3.89	3.66	2.71
K_2O	4.16	3.46	2.62	2.46	2.10
P_2O_5	0.30	0.40	0.54	0.52	0.38
TOTAL	98.31	99.75	99.34	99.27	97.37
Cr (ppm)	BD	BD	BD	BD	0
Ni	19	0	7	42	4
Cu	63	169	197	104	123
Zn	87	64	68	72	79
Rb	104	88	66	62	66
Sr	451	680	865	848	758
Y	36	30	27	28	28
Zr	430	273	223	215	206
Nb	32	24	15	14	23
Ba	1500	1324	1085	988	950
La	84.9	72.9	66.2	59.6	56.0
Ce	152.3	134.6	121.1	110.3	106.3
Pr	18.5	16.6	14.9	13.6	13.2
Nd	65.7	60.8	55.9	50.7	49.1
Sm	11.65	10.63	9.82	9.42	8.98
Eu	2.46	2.42	2.36	2.16	2.16
Gd	11.20	7.26	7.06	6.68	6.55
Tb	1.42	1.10	1.02	0.97	0.95
Dy	7.76	5.71	5.40	5.11	5.04
Ho	1.66	1.22	1.13	1.12	1.02
Er	4.99	3.18	3.00	2.91	2.96
Yb	4.11	3.38	2.87	2.66	2.55
Lu	0.66	0.48	0.42	0.45	0.43
Hf	-	-	-	-	5.73
Ta	-	-	-	-	1.33
Pb	-	-	-	-	7.07
Th	-	-	-	-	13.12

Table 2 continued

	1-3:121897	1-4:121897	1-5:121897	1-6:121897	1-7:121897
Color	light gray	light gray	black	light gray	white
Site	La Garita	La Garita	La Garita	La Garita	La Garita
SiO_2 (%)	65.90	65.70	61.50	66.60	66.20
TiO_2	0.75	0.79	1.05	0.74	0.74
Al_2O_3	15.60	15.50	16.30	15.40	15.50
Fe_2O_{3T}	3.21	3.29	5.70	3.16	3.09
MnO	0.11	0.11	0.15	0.11	0.11
MgO	0.65	0.65	1.65	0.62	0.61
CaO	1.76	1.77	3.84	1.74	1.71
Na_2O	4.20	3.95	4.40	4.40	4.43
K_2O	5.25	5.34	3.77	5.24	5.32
P_2O_5	0.13	0.13	0.42	0.13	0.13
TOTAL	97.56	97.23	98.78	98.14	97.84
Cr (ppm)	BD	BD	BD	BD	BD
Ni	BD	BD	BD	BD	11
Cu	19	10	21	8	19
Zn	66	68	84	68	67
Rb	137	136	101	132	135
Sr	294	302	595	283	273
Y	41	42	36	42	42
Zr	406	405	309	403	412
Nb	49	55	38	53	55
Ba	1818	1833	1465	1807	1766
La	78.4	78.7	86.1	76.8	77.0
Ce	191.5	186.3	158.1	187.1	186.3
Pr	19.2	18.1	19.7	18.0	18.3
Nd	62.1	57.8	71.2	58.2	60.2
Sm	10.68	10.43	12.27	10.20	11.07
Eu	2.34	2.24	2.65	2.23	2.22
Gd	8.41	7.93	9.28	7.56	8.15
Tb	1.01	1.00	1.28	1.03	1.08
Dy	6.00	5.44	6.90	5.55	5.50
Ho	1.28	1.17	1.48	1.21	1.25
Er	3.35	3.27	3.88	3.31	3.07
Yb	3.38	3.40	3.69	3.25	3.32
Lu	0.52	0.51	0.56	0.52	0.51
Hf	8.12	8.95	9.1	8.88	9.29
Ta	2.54	2.87	2.22	2.69	2.89
Pb	18.76	14.73	11.33	23.83	25.58
Th	20.21	22.31	22.13	21.41	22.38

Table 2 continued

	1-8:121897	1-9:121897	18-1:010498	18-1b:010498	18-2:010498
Color	white	white	banded	banded	white
Site	La Garita	La Garita	Río Grande	Río Grande	Río Grande
SiO_2 (%)	64.40	66.00	61.40	64.10	66.70
TiO_2	0.74	0.77	1.14	0.97	0.74
Al_2O_3	15.60	15.40	16.20	16.00	15.40
Fe_2O_{3T}	3.44	3.23	5.46	4.32	3.21
MnO	0.12	0.11	0.15	0.13	0.11
MgO	0.64	0.65	1.57	0.96	0.58
CaO	1.71	1.75	3.57	2.38	1.56
Na_2O	4.52	4.44	4.36	4.04	3.85
K_2O	5.34	5.15	3.89	4.76	5.49
P_2O_5	0.13	0.13	0.39	0.19	0.13
TOTAL	96.64	97.63	98.13	97.85	97.77
Cr (ppm)	745	BD	BD	BD	BD
Ni	79	BD	BD	BD	1
Cu	21	7	18	28	18
Zn	70	68	87	76	62
Rb	140	132	98	121	140
Sr	280	280	580	413	284
Y	42	41	36	39	41
Zr	413	404	316	369	404
Nb	55	56	42	50	53
Ba	1819	1784	1489	1617	1878
La	78.2	78.3	89.8	85.8	80.2
Ce	189.1	185.5	167.1	172.1	195.8
Pr	18.7	18.5	20.1	19.2	18.9
Nd	59.9	60.8	72.5	66.4	59.6
Sm	10.17	11.01	12.57	11.08	10.97
Eu	2.18	2.21	2.77	2.54	2.11
Gd	7.78	8.27	9.05	8.55	7.91
Tb	1.03	1.08	1.34	1.20	1.02
Dy	5.89	5.34	7.23	6.51	5.89
Ho	1.29	1.23	1.55	1.35	1.30
Er	3.33	3.22	4.01	3.64	3.30
Yb	3.41	3.11	3.85	3.62	3.99
Lu	0.56	0.54	0.58	0.56	0.41
Hf	8.95	8.43	8.72	9.04	9.26
Ta	2.78	2.8	2.26	2.69	2.93
Pb	24.87	24.54	12.01	15.4	12.84
Th	22.43	21.34	21.02	23.02	22.45

Table 2 continued

	18-3:010498	18-4:010498	18-5:010498	13-1:122997	13-2:122997
Color	banded	collapsed	whole rock	black	black
Site	Río Grande	Río Grande	Río Grande	Barreal	Barreal
SiO_2 (%)	66.10	64.50	61.30	56.70	54.80
TiO_2	0.77	0.88	1.01	0.95	0.93
Al_2O_3	15.60	16.00	17.50	19.10	19.70
Fe_2O_{3T}	3.36	3.92	5.48	6.66	7.00
MnO	0.10	0.12	0.13	0.13	0.13
MgO	0.59	0.82	1.12	2.08	2.37
CaO	1.61	2.19	3.79	6.97	7.61
Na_2O	3.87	3.84	4.04	3.77	3.56
K_2O	5.45	4.99	3.67	2.56	2.38
P_2O_5	0.14	0.17	0.29	0.53	0.52
TOTAL	97.59	97.43	98.33	99.45	99.00
Cr (ppm)	BD	BD	BD	BD	BD
Ni	BD	6	BD	10	2
Cu	11	26	38	297	91
Zn	53	75	80	80	76
Rb	142	127	97	66	61
Sr	313	382	589	873	918
Y	38	39	32	26	26
Zr	400	377	312	288	261
Nb	54	55	41	13	9
Ba	1895	1758	1500	1111	1010
La	79.0	74.8	82.7	71.7	65.0
Ce	186.4	180.0	151.0	127.4	113.3
Pr	17.9	17.6	17.7	14.4	13.1
Nd	57.4	58.2	62.3	55.2	49.8
Sm	9.85	10.10	10.78	9.86	8.95
Eu	2.07	2.35	2.42	2.32	2.20
Gd	7.37	7.53	7.89	8.36	7.88
Tb	0.98	1.07	1.10	1.11	1.00
Dy	5.11	4.93	6.31	5.07	5.14
Ho	1.15	1.11	1.38	1.04	0.99
Er	3.08	3.09	3.59	3.14	2.83
Yb	3.69	3.06	3.30	2.63	2.49
Lu	0.45	0.53	0.53	0.43	0.40
Hf	8.82	8.33	8.52	-	-
Ta	2.96	2.63	2.15	-	-
Pb	10.16	23.46	11.97	-	-
Th	23.06	21.86	20.54	-	-

Table 2 continued

	13-3:122997	13-4:122997	9-1:122397	9-2:122397	17-1:010298
Color	black	black	banded	banded	dark gray
Site	Barreal	Barreal	Buenos Aires	Buenos Aires	Virilla
SiO_2 (%)	55.90	55.70	60.10	60.90	56.49
TiO_2	0.94	0.94	1.07	1.11	0.87
Al_2O_3	19.30	19.30	17.50	16.50	19.35
Fe_2O_{3T}	7.00	6.73	6.10	6.08	6.84
MnO	0.13	0.13	0.14	0.15	0.14
MgO	2.29	2.22	1.52	1.71	2.08
CaO	7.15	7.13	4.13	4.05	7.16
Na_2O	3.47	3.66	3.67	4.09	3.63
K_2O	2.44	2.58	3.43	3.63	2.42
P_2O_5	0.48	0.53	0.38	0.44	0.49
TOTAL	99.10	98.92	98.04	98.66	99.47
Cr (ppm)	BD	BD	BD	BD	BD
Ni	BD	BD	BD	BD	BD
Cu	56	63	31	23	95
Zn	78	76	82	85	78
Rb	63	68	88	91	60
Sr	868	876	629	616	783
Y	26	27	36	36	29
Zr	240	252	375	379	225
Nb	10	12	21	22	15
Ba	1046	1090	1426	1392	956
La	60.6	64.3	88.0	86.4	57.1
Ce	112.1	117.9	151.3	150.4	104.2
Pr	14.2	15.0	19.4	19.0	12.7
Nd	51.1	53.5	69.0	69.0	48.2
Sm	8.86	9.45	12.07	11.92	8.64
Eu	2.21	2.33	2.74	2.69	2.11
Gd	8.01	8.19	11.09	10.93	7.50
Tb	1.02	1.05	1.41	1.44	0.94
Dy	5.13	5.25	7.34	7.44	4.80
Ho	1.02	1.11	1.55	1.59	0.96
Er	3.03	3.12	4.52	4.68	2.93
Yb	2.66	2.76	3.91	3.69	2.58
Lu	0.40	0.42	0.62	0.60	0.39
Hf	-	-	-	-	-
Ta	-	-	-	-	-
Pb	-	-	-	-	-
Th	-	-	-	-	-

Table 2 continued

	17-2:010298	17-3:010298	19-1:010498	19-3:010498	19-4:010498
Color	banded	gray	black	black	whole rock
Site	Virilla	Virilla	Calle Vueltas	Calle Vueltas	Calle Vueltas
SiO_2 (%)	58.39	58.07	58.87	58.66	59.95
TiO_2	0.89	1.00	1.05	1.01	1.03
Al_2O_3	18.27	18.26	16.76	18.43	17.58
Fe_2O_{3T}	6.27	6.18	6.07	6.74	5.96
MnO	0.14	0.14	0.15	0.14	0.14
MgO	1.74	1.76	1.46	1.90	1.66
CaO	6.36	4.79	3.44	5.67	4.18
Na_2O	3.91	4.03	4.46	3.69	4.26
K_2O	2.83	2.96	3.60	2.86	3.33
P_2O_5	0.46	0.49	0.41	0.45	0.43
TOTAL	99.26	97.68	96.27	99.55	98.52
Cr (ppm)	BD	BD	1109	BD	BD
Ni	BD	BD	110	BD	BD
Cu	54	26	35	64	32
Zn	74	76	79	74	75
Rb	75	82	103	78	91
Sr	744	648	570	685	589
Y	32	33	35	28	32
Zr	271	311	372	281	332
Nb	17	19	20	16	21
Ba	1111	1250	1461	1155	1314
La	66.0	72.3	81.9	67.1	74.9
Ce	118.0	134.4	156.4	124.8	140.4
Pr	14.1	15.6	18.6	15.8	16.7
Nd	54.0	58.2	64.0	55.5	58.3
Sm	9.79	10.22	10.93	9.62	9.93
Eu	2.30	2.37	2.43	2.21	2.31
Gd	8.08	8.71	10.42	8.58	9.57
Tb	1.05	1.16	1.27	1.08	1.19
Dy	5.25	5.46	6.65	5.45	5.77
Ho	1.03	1.12	1.41	1.13	1.25
Er	3.07	3.41	4.02	3.17	3.55
Yb	2.79	3.01	3.51	2.85	3.16
Lu	0.45	0.47	0.56	0.44	0.50
Hf	-	-	-	-	-
Ta	-	-	-	-	-
Pb	-	-	-	-	-
Th	-	-	-	-	-

Table 2 continued

	3-1:121997	3-2:121997	3-3:129197	4-1:122097	4-2:122097
Color	whole rock	collapsed	collapsed	ash fall	ash fall
Site	Santo Tomás	Santo Tomás	Santo Tomás	Santa Ana	Santa Ana
SiO_2 (%)	65.98	67.19	68.88	63.42	66.78
TiO_2	0.84	0.80	0.77	1.06	0.86
Al_2O_3	16.03	15.76	15.69	15.86	15.38
Fe_2O_{3T}	4.29	3.89	3.49	4.58	3.70
MnO	0.12	0.11	0.11	0.14	0.12
MgO	0.92	0.79	0.68	1.18	0.79
CaO	2.68	2.16	1.93	2.85	2.05
Na_2O	4.42	4.53	4.48	3.78	3.40
K_2O	4.35	4.71	4.94	4.19	4.84
P_2O_5	0.17	0.14	0.13	0.16	0.14
TOTAL	99.80	100.08	101.10	97.22	98.06
Cr (ppm)	BD	BD	BD	BD	BD
Ni	BD	BD	BD	BD	BD
Cu	47	21	39	4	33
Zn	70	70	58	80	79
Rb	115	127	131	115	131
Sr	402	330	317	487	317
Y	39	41	42	39	42
Zr	426	424	436	347	393
Nb	32	34	36	50	54
Ba	1611	1697	1772	1664	1708
La	83.6	84.0	84.6	80.6	70.6
Ce	162.4	175.3	184.6	164.0	174.6
Pr	16.6	16.6	16.5	18.1	16.6
Nd	57.9	56.2	56.5	61.1	54.7
Sm	10.09	10.05	9.93	10.59	9.80
Eu	2.15	2.16	2.08	2.46	2.14
Gd	8.82	8.47	8.27	7.56	7.30
Tb	1.16	1.15	1.15	1.09	1.00
Dy	5.62	5.48	5.19	5.48	5.16
Ho	1.13	1.13	1.13	1.27	1.27
Er	3.57	3.65	3.53	3.34	3.22
Yb	3.30	2.75	3.46	3.40	3.01
Lu	0.58	0.55	0.53	0.55	0.48
Hf	-	-	-	7.5	8.04
Ta	-	-	-	2.45	2.53
Pb	-	-	-	18.86	23.67
Th	-	-	-	20.14	19.64

Table 2 continued

	4-3:122097	4-4:122097	990710-1	990710-2	990711-3a1
Color	ash fall	ash fall	black	white	white
Site	Santa Ana	Santa Ana	La Garita	La Garita	La Garita
SiO_2 (%)	65.94	67.30	67.29	62.37	67.28
TiO_2	0.89	0.79	0.72	1.15	0.74
Al_2O_3	15.71	15.49	15.46	16.15	15.49
Fe_2O_{3T}	3.93	3.43	3.12	6.13	3.13
MnO	0.12	0.11	0.11	0.15	0.11
MgO	0.92	0.68	0.63	1.91	0.64
CaO	2.46	1.75	1.76	4.19	1.81
Na_2O	3.45	3.38	4.54	4.43	4.22
K_2O	4.53	5.31	5.22	3.54	5.23
P_2O_5	0.15	0.12	0.12	0.44	0.12
TOTAL	98.10	98.36	98.97	100.46	98.77
Cr (ppm)	BD	BD	BD	BD	BD
Ni	BD	BD	BD	BD	3
Cu	4	46	11	12	BD
Zn	73	79	67	86	69
Rb	120	144	131	88	130
Sr	400	272	264	602	277
Y	41	44	42	35	40
Zr	373	407	423	295	417
Nb	47	53	57	37	59
Ba	1725	1787	1803	1462	1818
La	73.1	80.9	74.6	75.0	72.9
Ce	169.8	188.2	168.9	136.1	165.6
Pr	17.0	18.3	17.1	17.2	16.7
Nd	55.9	61.9	54.2	62.5	53.3
Sm	9.86	10.82	10.40	11.58	9.45
Eu	2.27	2.24	2.06	2.59	1.98
Gd	6.93	7.82	9.62	10.72	8.74
Tb	1.07	1.09	1.07	1.24	0.97
Dy	5.52	5.75	5.38	6.58	5.65
Ho	1.18	1.27	1.16	1.23	1.05
Er	3.24	3.45	3.17	3.50	2.90
Yb	3.84	3.68	3.39	3.40	3.17
Lu	0.50	0.55	0.54	0.54	0.50
Hf	8.95	8.58	8.45	7.8	8.13
Ta	2.53	2.74	2.84	1.97	2.81
Pb	19.68	28.95	20.64	8.23	20.2
Th	21.63	21.93	23.73	20.36	23.07

Table 2 continued

	990711-3A2	990711-3b1	990711-3B2	990711-3c	990711-3e
Color	white	white	black	banded	banded
Site	La Garita	La Garita	La Garita	La Garita	La Garita
SiO_2 (%)	64.49	66.95	67.38	56.36	66.49
TiO_2	0.75	0.77	0.73	0.87	0.86
Al_2O_3	15.40	15.56	15.55	19.19	15.67
Fe_2O_{3T}	3.66	3.36	3.22	6.62	3.73
MnO	0.12	0.11	0.11	0.12	0.12
MgO	0.68	0.67	0.64	1.70	0.81
CaO	1.77	1.91	1.83	6.86	2.10
Na_2O	4.22	4.27	4.27	3.25	4.46
K_2O	4.96	5.25	5.32	2.43	4.89
P_2O_5	0.13	0.13	0.13	0.45	0.16
TOTAL	96.18	98.98	99.18	97.85	99.29
Cr (ppm)	BD	3	BD	3	BD
Ni	6	10	8	3	4
Cu	27	29	18	85	3
Zn	76	71	69	68	74
Rb	128	130	130	66	120
Sr	275	296	279	832	328
Y	41	40	42	25	41
Zr	414	409	417	220	399
Nb	39	58	53	25	56
Ba	1851	1834	1780	1094	1798
La	58.1	71.5	74.9	54.5	70.7
Ce	-	165.0	163.5	104.9	160.4
Pr	-	16.1	16.4	12.8	15.6
Nd	-	52.8	53.7	46.5	51.3
Sm	-	9.32	9.86	8.74	9.75
Eu	-	2.01	1.94	2.04	2.14
Gd	-	9.12	8.79	7.42	9.05
Tb	-	0.98	1.01	0.92	0.91
Dy	-	4.98	5.47	4.87	5.56
Ho	-	1.00	1.13	0.93	1.13
Er	-	2.82	2.99	2.49	2.90
Yb	-	3.22	3.39	2.46	3.22
Lu	-	0.48	0.54	0.38	0.47
Hf	-	8.28	8.92	5.55	8.22
Ta	-	2.71	2.71	1.29	2.66
Pb	-	19.94	19.43	5.76	18.74
Th	-	21.73	23.37	14.33	21.76

Table 2 continued

	990711-3f	990712-4c	990713-2b	990713-2d	990713-2f
Color	banded	gray	gray	light gray	banded
Site	La Garita	Río Colorado	La Aduana	La Aduana	La Aduana
SiO_2 (%)	66.69	60.89	64.85	66.41	61.88
TiO_2	0.81	1.24	0.84	0.77	1.16
Al_2O_3	15.61	16.30	15.81	15.25	15.99
Fe_2O_{3T}	3.44	8.15	4.03	3.31	5.30
MnO	0.12	0.15	0.11	0.11	0.15
MgO	0.70	1.70	0.76	0.54	1.52
CaO	1.90	5.00	2.11	1.42	3.45
Na_2O	4.23	3.71	3.87	3.85	4.05
K_2O	5.18	2.75	4.84	5.34	3.90
P_2O_5	0.13	0.63	0.20	0.13	0.34
TOTAL	98.81	100.52	97.42	97.13	97.74
Cr (ppm)	BD	311	BD	BD	BD
Ni	6	44	1	5	BD
Cu	38	89	17	5	23
Zn	68	86	58	57	85
Rb	128	71	118	129	97
Sr	289	676	368	281	541
Y	37	29	41	40	37
Zr	413	244	379	416	321
Nb	57	27	56	63	42
Ba	1800	1239	1773	1886	1552
La	68.1	61.0	68.0	73.4	73.4
Ce	164.0	111.5	158.3	179.9	143.3
Pr	15.6	14.8	15.3	17.3	17.2
Nd	49.8	56.1	49.0	51.4	61.3
Sm	9.36	10.55	8.73	9.68	11.30
Eu	2.04	2.49	1.99	2.00	2.45
Gd	8.25	9.22	8.17	8.93	9.56
Tb	0.96	1.15	0.90	1.03	1.11
Dy	5.17	6.30	4.89	5.30	6.04
Ho	1.03	1.19	0.98	1.02	1.18
Er	2.88	3.19	2.74	2.69	3.15
Yb	3.23	3.32	3.16	3.04	3.23
Lu	0.47	0.49	0.45	0.51	0.50
Hf	7.93	6.51	7.31	8.11	7.58
Ta	2.77	1.54	2.54	2.98	2.17
Pb	19.72	4.56	11.17	10.67	9.51
Th	21.41	15.35	20.32	21.56	20.4

Table 2 continued

	990713-2h	990713-3b	990713-4a	990713-4b	990713-4c
Color	light gray	banded	banded	black	black
Site	La Aduana	La Aduana	La Aduana	La Aduana	La Aduana
SiO_2 (%)	63.12	63.29	64.30	56.77	62.62
TiO_2	1.10	1.03	1.05	0.86	1.08
Al_2O_3	16.15	16.11	15.94	18.39	15.67
Fe_2O_{3T}	5.31	4.84	4.83	6.27	6.46
MnO	0.14	0.13	0.13	0.12	0.15
MgO	1.35	1.27	1.27	1.76	1.88
CaO	3.08	3.02	3.05	6.47	4.38
Na_2O	4.05	3.94	3.99	3.19	3.80
K_2O	4.03	4.04	4.10	2.69	3.39
P_2O_5	0.33	0.26	0.27	0.43	0.47
TOTAL	98.66	97.93	98.93	96.95	99.90
Cr (ppm)	BD	BD	BD	BD	1479
Ni	1	4	0	BD	166
Cu	25	13	8	68	30
Zn	73	75	78	70	94
Rb	100	104	106	72	90
Sr	548	448	455	770	637
Y	37	38	38	28	34
Zr	316	346	346	237	296
Nb	42	43	45	27	36
Ba	1573	1580	1619	1138	1455
La	75.2	71.3	73.3	56.5	71.4
Ce	141.9	139.9	150.0	105.9	139.3
Pr	17.2	16.7	17.0	13.3	17.8
Nd	60.7	57.4	59.1	48.5	64.7
Sm	11.00	9.98	10.87	8.90	11.92
Eu	2.36	2.26	2.40	2.07	2.70
Gd	9.44	9.19	9.47	7.80	10.05
Tb	1.18	1.07	1.13	0.96	1.21
Dy	6.39	6.11	5.98	5.05	6.44
Ho	1.20	1.16	1.10	0.97	1.24
Er	3.22	3.25	3.17	2.57	3.40
Yb	3.33	3.29	3.25	2.65	3.44
Lu	0.49	0.52	0.49	0.41	0.51
Hf	8.07	8.33	7.82	5.95	7.35
Ta	2.23	2.33	2.27	1.43	1.87
Pb	8.09	12.12	12.82	8.26	8.54
Th	21.05	21.9	21.31	14.91	18.75

Table 2 continued

	990713-4d
Color	white
Site	La Aduana
SiO_2 (%)	65.09
TiO_2	0.81
Al_2O_3	15.90
Fe_2O_{3T}	4.23
MnO	0.13
MgO	1.05
CaO	2.76
Na_2O	3.53
K_2O	4.66
P_2O_5	0.16
TOTAL	98.32
Cr (ppm)	BD
Ni	3
Cu	24
Zn	72
Rb	117
Sr	363
Y	39
Zr	372
Nb	34
Ba	1172
La	63.3
Ce	-
Pr	-
Nd	-
Sm	-
Eu	-
Gd	-
Tb	-
Dy	-
Ho	-
Er	-
Yb	-
Lu	-
Hf	-
Ta	-
Pb	-
Th	-

Table 3 **Phenocryst Compositions**

Clinopyroxene	SiO_2	TiO_2	Al_2O_3	FeO	MnO	MgO	CaO	Na_2O
13-2.1-core-cpx	50.71	0.60	2.07	10.44	0.39	15.25	19.71	0.42
13-2.1-rim-cpx	50.40	0.51	2.38	8.48	0.34	15.48	20.22	0.40
13-2.1-int-cpx	51.34	0.61	1.96	10.89	0.33	15.42	20.06	0.41
13-2.4-1-rim-cpx	50.13	0.58	2.46	7.09	0.28	15.50	20.92	0.38
13-2.41-int-cpx	50.08	0.56	2.39	8.79	0.30	15.57	20.83	0.36
13-2.4-1-rim-cpx	50.96	0.70	2.26	10.37	0.44	15.57	20.47	0.43
13-2.4-2-rim-cpx	50.39	0.56	2.34	8.09	0.33	15.51	21.03	0.38
13-2.4-2-core-cpx	50.90	0.55	2.12	9.65	0.29	15.71	20.92	0.38
11-5.1-cpx	51.29	0.48	1.42	9.42	0.71	15.23	20.96	0.43
1-3.3-rim-cpx	52.10	0.46	1.32	9.57	0.72	15.03	20.63	0.45
1-3.3-int-cpx	52.17	0.41	1.09	8.70	0.64	15.57	20.08	0.43
1-3.3-core-cpx	51.24	0.68	1.83	9.52	0.67	14.83	20.53	0.47
1-3.3-rim-cpx	51.44	0.45	1.23	10.02	0.72	15.05	20.34	0.40
1-3.3-rim-cpx	51.84	0.61	1.52	10.01	0.64	15.10	20.26	0.47
16-3.3-core-cpx	50.32	0.62	2.14	8.68	0.30	15.33	20.08	0.39
16-3.3-int-cpx	50.85	0.60	2.35	10.33	0.30	15.29	20.18	0.41
16-3.3-rim-cpx	50.81	0.63	2.66	9.20	0.37	15.39	20.40	0.40
16-6.3-core-cpx	51.61	0.66	1.86	10.72	0.78	15.08	20.39	0.42
16-6.3-rim-cpx	52.69	0.26	0.83	10.67	1.03	14.31	20.90	0.47
16-6.4-int-cpx	52.88	0.27	0.91	9.68	0.90	14.54	21.37	0.42
16-6.4-int2-cpx	52.43	0.31	0.85	10.09	0.88	14.13	21.32	0.49
16-6.4-core-cpx	52.93	0.37	1.26	9.63	0.68	15.01	21.02	0.49
16-6.4-core2-cpx	52.68	0.45	1.21	9.14	0.77	14.91	21.22	0.43
1-7.1-rim-cpx	54.51	0.19	0.51	19.75	1.27	24.82	1.49	0.16
1-7.1-rim2-cpx	53.93	0.23	0.60	16.76	1.40	25.30	1.45	0.12
1-7.2-rim-cpx	51.61	0.46	1.37	8.20	0.74	15.09	20.80	0.44
1-7.2-core-cpx	51.12	0.54	2.13	10.32	0.75	14.76	20.30	0.46
1-7.3-rim-cpx	51.10	0.54	1.44	8.87	0.71	15.01	20.89	0.46
1-7.3-int-cpx	51.89	0.42	1.06	10.35	0.84	14.71	20.81	0.45
1-7.3-core-cpx	51.72	0.44	1.45	8.18	0.72	15.15	21.02	0.46
18-2.4-1rim-cpx	51.35	0.41	1.25	9.41	0.72	15.13	20.86	0.46
18-2.4-1core-cpx	51.31	0.48	1.19	9.94	0.71	15.10	20.63	0.41
18-2.4-2rim-cpx	50.56	0.48	1.31	7.80	0.71	15.16	20.95	0.41
18-2.4-2core-cpx	51.32	0.43	1.19	10.64	0.78	14.93	20.76	0.41
18-2.4-2rimrpt1-cpx	49.96	0.58	1.53	8.26	0.77	14.60	20.58	0.49
18-2.4-2rimrpt2-cpx	51.08	0.44	1.12	11.06	0.75	14.92	20.71	0.41
18-2.4-2int-cpx	50.84	0.41	1.33	8.80	0.68	14.99	20.82	0.40
18-2.4-3int-cpx	50.39	0.50	1.29	8.84	0.81	14.81	20.62	0.47
18-2.3-core-cpx	57.16	0.04	25.56	4.52	0.02	0.01	7.97	6.12
18-2.3-rim-cpx	56.17	0.02	25.47	0.47	0.00	0.00	8.36	5.92
6-3B.2-Inplrim-cpx	51.23	0.59	1.68	5.27	0.75	15.32	20.65	0.45

Table 3 Continued **Phenocryst Compositions**

Orthopryoxene	SiO_2	TiO_2	Al_2O_3	FeO*	MnO	MgO	CaO	Na_2O
1-3.1-rim-opx	52.94	0.26	0.54	18.61	1.26	24.84	1.41	0.12
1-3.1-core-opx	52.71	0.36	0.99	18.94	1.37	24.36	1.52	0.17
18-2.1-rim-opx	53.57	0.25	0.68	16.18	1.34	24.90	1.42	0.12
18-2.1-core-opx	53.12	0.29	0.62	17.22	1.33	24.98	1.32	0.14
18-2.1-othrim-opx	53.50	0.22	0.57	18.95	1.19	25.00	1.42	0.12
6-3B.1-rim-opx	52.35	0.36	1.00	16.43	1.22	24.88	1.96	0.13
6-3B.1-core-opx	52.03	0.21	0.67	18.15	1.33	25.02	1.38	0.17
6-3B.1-2core-opx	52.74	0.26	0.71	19.00	1.18	25.26	1.43	0.11
6-3B.1-2rim-opx	52.10	0.35	1.03	18.25	1.24	24.78	1.48	0.13
11-5.1-opx	53.85	0.32	0.94	19.28	0.61	24.95	1.87	0.12
11-5.1-opx	52.85	0.31	0.89	16.26	0.55	24.64	2.92	0.14
16-1.4-1opx-a-opx	52.01	0.16	0.32	27.30	1.04	18.32	1.48	0.11
16-1.4-iopx-b-opx	50.90	0.13	0.34	27.31	1.07	18.35	1.41	0.10
16-1.4-1opx-c-opx	52.88	0.32	1.14	16.48	0.54	26.20	1.82	0.14
16-1.4-1opx-d-opx	53.33	0.31	1.18	16.09	0.56	26.19	1.73	0.08
16-1.4-1opx-e-opx	53.14	0.30	1.15	16.65	0.63	26.29	1.68	0.10
16-1.4-2opx-a-opx	51.54	0.10	0.21	27.13	0.97	18.83	1.28	0.10
16-1.4-2opx-b-opx	51.93	0.09	0.20	27.92	0.76	18.49	1.38	0.15
16-1.4-2opx-c-opx	53.39	0.27	1.22	13.25	0.58	26.57	1.74	0.15
16-1.4-2opx-c-opx	54.15	0.23	0.90	17.20	0.57	26.63	1.74	0.12

Table 3 Continued **Phenocryst Compositions**

Plagioclase	SiO_2	Al_2O_3	FeO	CaO	Na_2O	K_2O
13-2.2-rim-pl	49.61	31.20	0.71	14.89	2.90	0.21
13-2.2-int-pl	49.29	31.76	0.71	15.05	2.86	0.19
13-2.2-int/core-pl	49.07	31.99	0.62	15.20	2.61	0.15
13-2.2-core-pl	48.06	32.35	0.85	15.84	2.43	0.08
13-2.3-rim-pl	49.34	2.53	8.20	20.95	0.44	0.02
11-5.1-pl	52.99	29.32	0.76	12.36	4.13	0.46
11-5.1-pl	54.27	29.09	0.75	11.70	4.54	0.49
11-5.1-pl	63.80	16.60	1.55	1.19	5.26	4.70
11-5.3-pl	58.01	26.13	0.42	8.01	6.23	0.78
11-5.3-pl	57.63	26.10	0.56	8.16	6.26	0.79
11-5.3-pl	56.91	27.05	0.45	9.30	5.88	0.61
1-3.1-rim-pl	59.44	25.50	0.51	7.21	6.66	0.97
1-3.1-core-pl	58.37	25.59	0.32	7.93	6.51	0.86
1-3.3-rim-pl	57.83	26.24	0.52	8.15	6.19	0.81
1-3.3-core-pl	58.68	25.70	0.42	7.78	6.43	0.93
16-1.3-rim-pl	49.77	32.22	0.73	15.10	3.01	0.17
16-1.3-int-pl	48.76	32.31	0.55	15.53	2.73	0.15
16-1.3-core-pl	48.02	32.37	0.67	16.04	2.50	0.17
16-1.3-core2-pl	48.11	32.22	0.59	15.99	2.37	0.16
16-1.3-core3-pl	47.68	32.36	0.72	16.25	2.44	0.11
16-1.3-int-pl	48.16	31.92	0.63	16.01	2.51	0.10
16-1.4-rima-pl	60.49	23.72	0.39	6.29	6.87	1.38
16-1.4-rimb-pl	60.99	23.65	0.42	6.22	6.76	1.70
16-1.4-corec-pl	48.35	32.40	0.68	15.83	2.46	0.17
16-1.4-cored-pl	49.31	31.24	0.71	15.10	2.85	0.18
16-3.2-rim-pl	57.96	26.46	0.51	8.77	6.18	0.65
16-3.2-int-pl	55.39	28.04	0.65	10.61	5.31	0.49
16-3.2-core-pl	54.81	28.42	0.31	10.75	5.11	0.46
16-3.2-otrim-pl	55.20	27.99	0.53	10.41	5.31	0.46
16-6.1-a-pl	58.58	26.13	0.47	7.74	6.46	0.86
16-6.1-b-pl	59.17	25.23	0.52	7.33	6.65	0.89
16-6.1-c-pl	57.68	26.44	0.49	8.40	6.05	0.72
16-6.1-d-pl	57.84	26.47	0.55	8.68	6.00	0.72
16-6.1-e-pl	58.42	26.32	0.64	8.52	6.26	0.76
16-6.1-f-pl	54.94	28.78	0.52	11.04	5.13	0.51
16-6.1-g-pl	54.88	28.49	0.52	10.71	5.03	0.45
16-6.1-h-pl	54.83	28.93	0.38	10.73	5.19	0.49
16-6.1-I-pl	54.80	28.84	0.41	11.26	4.84	0.40
16-6.1-i2-pl	54.65	28.15	0.35	10.87	5.04	0.41
16-6.1-k-pl	59.42	25.92	0.43	7.63	6.47	0.93
16-6.1-L-pl	59.56	25.60	0.40	7.34	6.52	0.85
16-6.1-m-pl	58.28	26.66	0.37	8.07	6.29	0.83
16-6.1-n-pl	57.37	26.92	0.54	9.12	5.96	0.66
16-6.1-o-pl	57.99	27.32	0.42	8.90	6.00	0.69
16-6.1-p-pl	58.93	26.20	0.39	8.05	6.30	0.76
16-6.1-q-pl	57.19	26.39	0.49	8.64	6.09	0.68
16-6.2-rim-pl	57.77	26.33	0.44	8.60	6.17	0.86
16-6.2-int-pl	57.69	26.34	0.50	8.20	6.17	0.77
16-6.2-core-pl	58.51	25.76	0.48	7.86	6.39	0.78
1-6.1-core-pl	53.28	29.34	0.49	12.11	4.46	0.37
1-6.1-int-pl	54.92	28.17	0.42	10.91	5.02	0.51
1-6.1-rim-pl	58.20	25.29	0.42	7.74	6.36	0.94

Table 3 Continued **Phenocryst Compositions**

Plagioclase	SiO_2	TiO_2	Al_2O_3	FeO*	CaO	Na_2O	K_2O
1-6.2-rim-pl	57.95	0.00	25.78	0.49	8.49	6.15	0.71
1-7.1-rim-pl	58.59	0.00	25.74	0.45	7.78	6.43	0.87
1-7.1-intb-pl	60.09	0.00	24.71	0.33	6.40	6.94	1.25
1-7.1-intc-pl	57.73	0.00	26.09	0.30	8.27	6.24	0.79
1-7.1-intc-pl	57.80	0.00	26.37	0.45	8.32	6.14	0.74
1-7.1-core-pl	58.77	0.00	25.92	0.50	7.69	6.55	0.83
1-7.2-rim-pl	59.22	0.00	24.29	0.41	6.45	6.83	1.04
1-7.2-rim2-pl	59.16	0.00	24.37	0.48	6.69	6.90	1.05
1-7.2-rim3-pl	58.06	0.00	25.13	0.43	7.79	6.45	0.85
1-7.2-core-pl	58.93	0.00	25.12	0.46	7.44	6.49	1.01
1-7.2-othrim-pl	59.23	0.00	25.86	0.55	7.70	6.42	0.79
18-2.4-1rim-pl	57.18	0.00	25.64	0.36	8.04	6.39	0.80
18-2.4-1rimrpt-pl	59.98	0.00	24.71	0.38	6.83	6.94	1.11
18-2.4-1int-pl	58.08	0.00	26.09	0.45	7.94	6.26	0.81
18-2.4-1int2-pl	57.55	0.00	26.17	0.46	8.37	6.03	0.75
18-2.4-1core-pl	57.79	0.00	26.85	0.50	8.89	6.05	0.73
18-2.4-1othrim-pl	57.19	0.00	26.73	0.37	8.88	6.08	0.61
18-2.4-2rim-pl	58.53	0.00	24.90	0.33	7.34	6.41	1.00
18-2.4-2int-pl	56.91	0.00	26.07	0.38	8.51	6.07	0.72
18-2.4-2core-pl	56.49	0.00	26.43	0.40	9.00	5.85	0.58
18-2.4-pl	57.00	0.00	26.46	0.47	8.68	6.06	0.70
18-2.3-rim-pl	56.95	0.00	25.11	0.46	7.78	6.45	0.85
18-2.2-rim2-pl	56.60	0.00	27.47	0.57	9.34	5.56	0.56
18-2.2-int-pl	56.99	0.00	26.79	0.61	8.82	6.00	0.67
18-2.2-othrim-pl	67.12	0.00	14.96	2.13	1.24	4.20	5.49
18-2.2-othrim2-pl	67.54	0.00	14.99	2.12	1.24	4.19	5.61
18-2.2-rimd-pl	57.35	0.00	26.34	0.52	8.98	6.03	0.78
18-2.1-rim--pl	57.98	0.00	25.56	0.31	7.66	6.52	0.90
18-2.1-core-pl	58.44	0.00	25.62	0.37	7.67	6.53	0.87
18-2.1-int-pl	58.93	0.00	25.13	0.44	7.13	6.65	0.95
18-2.1-othrim-pl	58.76	0.00	25.61	0.50	7.77	6.43	0.95
6-3B.1-rim-pl	61.30	0.00	21.12	0.97	5.38	5.61	2.34
6-3B.1-rimrpt-pl	56.91	0.00	26.38	0.43	8.53	6.09	0.76
6-3B.1-int-pl	57.18	0.00	26.24	0.44	8.43	6.25	0.76
6-3B.1-core-pl	56.85	0.00	26.71	0.46	9.01	5.94	0.73

Table 3 Continued	Phenocryst Compositions						
K-Feldspar	SiO_2	TiO_2	Al_2O_3	FeO*	CaO	Na_2O	K_2O
6-3B.2-rim-fld	58.67	0.00	25.77	0.39	7.83	6.29	0.77
6-3B.2-int-fld	56.51	0.00	26.46	0.57	8.88	6.02	0.62
6-3B.2-core-fld	57.36	0.00	25.86	0.55	8.34	6.14	0.71
6-3B.2-corerpt-fld	57.11	0.00	25.94	0.72	8.31	6.14	0.80

Table 3 Continued **Phenocryst Compositions**

Olivine	SiO_2	TiO_2	Al_2O_3	FeO*	MnO	MgO	CaO
13-2.3b-rim-ol	37.09	0.01	0.00	25.30	0.49	36.69	0.14
13-2.3b-int-ol	36.82	0.01	0.04	25.68	0.45	36.94	0.13
13-2.3b-core-ol	37.06	0.05	0.03	25.59	0.57	36.87	0.19
13-2.4-1-rim-ol	37.03	0.02	0.02	25.45	0.53	36.74	0.18
13-2.4-1-int-ol	37.19	0.01	0.01	25.26	0.50	36.77	0.16
13-2.4-1-core-ol	36.99	0.00	0.00	25.20	0.48	36.43	0.16
13-2.4-1-rim-ol	36.98	0.02	0.05	25.51	0.46	37.04	0.15
13-2.4-2-rim-ol	36.97	0.01	0.00	25.48	0.56	36.75	0.14
13-2.4-2-int-ol	36.90	0.00	0.05	25.22	0.49	37.00	0.21
13-2.4-2-core-ol	37.04	0.02	0.03	25.13	0.46	36.87	0.23
13-2.4-2-rim-ol	37.15	0.00	0.03	25.11	0.47	37.19	0.20
16-1.2-rim-ol	37.94	0.04	0.03	25.18	0.54	36.61	0.14
16-1.2-int-ol	37.35	0.03	0.01	25.71	0.53	36.45	0.15
16-1.2-core-ol	37.37	0.05	0.02	24.94	0.53	36.69	0.13
16-1.1-core-ol	37.36	0.02	0.05	25.81	0.45	36.66	0.15
16-1.1-rim-ol	37.28	0.02	0.00	25.21	0.54	36.77	0.19
16-1.4-rimonopx-ol	51.07	0.17	0.34	27.30	0.97	18.55	1.34
16-1.4-rim-ol	36.91	0.00	0.04	26.51	0.63	35.40	0.14
16-3.4-rim-ol	36.81	0.01	0.02	24.75	0.46	37.01	0.14
16-3.4-int-ol	36.73	0.00	0.02	24.19	0.45	37.40	0.16
16-3.4-int2-ol	36.49	0.02	0.02	24.68	0.54	37.31	0.17
16-3.4-core-ol	37.31	0.00	0.01	24.51	0.45	37.29	0.13
16-3.4-rim2-ol	36.80	0.00	0.02	24.65	0.49	37.65	0.16

Table 3 Continued	Phenocryst Compositions						
Magnetite-Ilmenite Pairs	SiO_2	TiO_2	Al_2O_3	FeO*	MnO	MgO	CaO
1-3.1 il	0.02	45.53	0.25	49.84	1.08	3.95	0.04
1-3.1-mt	0.08	12.16	2.14	82.55	0.94	2.66	0.02
16-3.1-il	0.03	43.42	0.22	48.78	1.11	3.38	0.02
16-3.1-mt	0.08	10.58	1.84	86.11	0.50	0.88	0.04
16-6.3-a-il	0.00	53.55	0.02	42.21	0.51	3.76	0.00
16-6.3-mt	0.04	12.29	2.19	83.19	0.97	2.64	0.05
16-6.3-b-il	0.05	45.53	0.25	50.38	1.19	3.39	0.02
16-6.3-b-mt	0.20	12.52	2.09	80.48	0.99	2.34	0.10
18-2.1-il	0.03	44.94	0.24	51.47	1.18	3.41	0.01
18-2.1-a-mt	0.07	12.28	2.24	82.32	0.94	2.56	0.01
18-2.1-b-il	0.01	44.85	0.26	50.78	1.04	3.27	0.09
18-2.1-b-mt	0.07	12.06	2.26	82.32	0.95	2.51	0.02
6-3B.1-core-il	0.04	44.88	0.26	50.67	1.10	3.88	0.04
6-3B.1-core-mt	0.06	12.36	2.23	82.76	0.87	2.71	0.01
6-3B.1-rim-il	0.00	44.83	0.28	50.41	1.05	3.98	0.04
6-3B.1-rim-mt	0.08	12.12	2.23	82.37	0.92	2.69	0.06

Table 3 Continued	Phenocryst Compositions						
Other Magneite and Illmenites	SiO_2	TiO_2	Al_2O_3	FeO^*	MnO	MgO	CaO
16-3.1-dmt	0.09	10.65	1.74	86.24	0.42	0.88	0.04
16-3.1-cmt	0.09	10.58	1.63	87.61	0.38	0.89	0.01
6-3B.1-corerpt-mt	0.05	12.25	2.31	82.91	0.85	2.70	0.00
6-3B.1-corerpt2-mt	0.04	12.16	2.30	82.51	1.00	2.65	0.00
16-6.3-c-il	0.00	45.73	0.23	50.46	1.00	3.54	0.05
1-7.3-a-il	0.02	45.49	0.22	50.23	1.04	3.98	0.18
1-7.3-b-il	0.03	45.39	0.27	49.34	1.13	3.93	0.17
1-7.3-2-il	0.00	45.56	0.22	49.40	1.18	3.91	0.03

Table 4. Point Counting: By volume phenocryst content

	54 wt.%		58 wt.%		62 wt. %	
	Counts	*%Volume*	*Counts*	*%Volume*	*Counts*	*%Volume*
matrix	382	67	610	80	540	97
plagioclase	162	28	116	15	5	2
pyroxene	21	4	23	3	0	1
olivine	4	0.70	1	0.13	0	0
oxides	1	0.18	8	1.06	1	0.18
total	570	100	758	100	546	100

Values based on an average of 600 point counts; 8% error.

Table 5 PARTITION COEFFICIENTS

A. RHYOLITIC MELT

el/min	PL	CPX	OPX	MT	IL
Rb	0.041	0.032	0.003	0	0
Sr	4.4	0.516	0.009	0	0
Ba	0.308	0.131	0.003	0	0
K	0.1	0.037	0.002	0	0
Y	0.1	4	1	2	0
Ti	0.05	0.7	0.4	12.5	0
Zr	0.1	0.6	0.2	0.8	0
Nb	0.06	0.8	0.8	2.5	0
Ce	0.27	0.5	0.15	0	1.64
Nd	0.21	1.11	0.22	0	2.267
Sm	0.013	1.67	0.27	0	2.833
Eu	2.15	1.56	0.17	0	1.013
Gd	0.097	1.85	0.34	0	0
Dy	0.064	1.93	0.46	0	2.633
Er	0.055	1.8	0.65	0	0
Yb	0.049	1.58	0.86	0	1.467
Lu	0.046	1.54	0.9	0	0
Ni	0	0	0	10	0
V	0	0	0	30	109
Cr	0	0	0	32	10.633
Sc	0.053	53	18	0	32
Mn	0.365	32.667	45.5	0	0

B. ANDESITIC MELT

Element	PL	CPX	OPX	OL	MT
Rb	0.07	0.02	0.022	0	0.01
Sr	1.8	0.08	0.032	0	0.01
Ba	0.16	0.02	0.013	0	0.01
K	0.11	0.02	0.014	0	0.01
Y	0	1.5	0.45	0.01	0.5
Ti	0	0.4	0.25	0.03	9
Zr	0.01	0.27	0.1	0.01	0.2
Hf	0	0.25	0.1	0	0
Nb	0	0.3	0.35	0.01	1
Ta	0	0	0	0	0
Th	0.01	0.01	0.05	0.01	0.1
La	0.302	0.047	0.031	0	0
Ce	0.2	0.25	0.05	0	0.2
Sm	0.11	0.75	0.1	0	0.3
Eu	0.31	0.8	0.12	0	0.25
Yb	0.05	0.9	0.46	0	0.25
Ni	0.01	6	8	58	10
Co	0.01	3	6	0	8
V	0.01	1.1	1.1	0.08	30
Cr	0.01	30	13	34	32
Sc	0.01	3	3	0.3	2

Table 6A Fractional Crystallization Models for the Low Silica Group

STEP A					COMBINED STEP A AND STEP B				
Parent	13-2:122997				Parent	13-2:122997			
Daughter	19-3:010498				Daughter	990710-2			
%	Min/Rock				%	Min/Rock			
18.3	Plagioclase				31.7	Plagioclase			
1.8	Olivine				3.1	Olivine			
1.5	Clinopyroxene				2.3	Magnetite			
1.1	Magnetite				0.06	Apatite			
0.05	Apatite				0.03	Clinopyroxene			
0.765 Liquid Remaining					0.62 Liquid Remaining				
Sum of the squares of the residuals= 0.091					Sum of the squares of the residuals= 0.03				
	Daughter	13-2; Rock	13-2;Calc	Residual		Daughter	13-2; Rock	13-2;Calc	Residual
*SiO2	59.33	55.75	55.92	0.17	*SiO2	62.47	55.75	55.81	0.06
TiO2	1.02	0.95	0.95	0	TiO2	1.15	0.95	0.95	0
Al2O3	18.64	20.04	20.04	0	Al2O3	16.17	20.04	20	0.04
FeO	6.13	6.41	6.41	0	FeO	5.52	6.41	6.41	0
MnO	0.14	0.13	0.16	0.03	MnO	0.15	0.13	0.16	0.03
MgO	1.92	2.41	2.38	0.03	MgO	1.91	2.41	2.4	0.01
CaO	5.73	7.74	7.70	0.04	CaO	4.2	7.74	7.73	0.01
Na2O	3.73	3.62	3.39	0.23	Na2O	4.44	3.62	3.67	0.05
K2O	2.89	2.42	2.25	0.17	K2O	3.55	2.42	2.26	0.16
P2O5	0.46	0.53	0.58	0.05	P2O5	0.44	0.53	0.55	0.02
Prediction based on distribution coefficients					Prediction based on distribution coefficients				
Rb	79.00	62.00	61.40	0.6	Rb	88.4	62	56.4	5.6
Sr	692.30	933.90	774.20	159.7	Sr	603.3	933.9	767.4	166.5
Ba	1167.60	1027.70	924.40	103.3	Ba	1464.6	1027.7	968.1	59.6
Y	28.50	26.30	22.50	3.8	Y	34.8	26.3	22	4.3
Zr	284.30	265.30	219.60	45.7	Zr	295.2	265.3	185	80.3
Nb	16.30	9.56	12.70	3.14	Nb	37.5	9.56	24	14.44
La	67.90	66.10	55.40	10.7	La	75.1	66.1	52.5	13.6
Ce	126.30	115.30	101.40	13.9	Ce	136.3	115.3	92.1	23.2
Sm	9.73	9.10	7.75	1.35	Sm	11.6	9.1	7.6	1.5
Eu	2.24	2.24	1.86	0.38	Eu	2.59	2.24	1.84	0.4
Tb	2.88	2.53	2.27	0.26	Tb	3.41	2.53	2.18	0.35

* In multiple linear regression calculations , silica is weighted at 0.4, the rest of the major elements are weighted at 1

Table 6B Fractional Crystallization models for the High Silica Group

Parent	990710-2			
Daughter	1-7:121897			
%	Min/Rock			
21.9	Plagioclase			
5.2	Clinopyroxene			
4	Orthopyroxene			
1.7	Magnetite			
0.09	Ilmenite			
0.662	Liquid Remaining			
Sum of the squares of the residuals= 0.204				
	Daughter	1-7 Rock	1-7 Calc	Residual
*SiO2	67.88	62.47	62.28	0.19
TiO2	0.76	1.15	1.15	0
Al2O3	15.89	16.17	16.47	0.3
FeO	2.85	5.52	5.52	0
MnO	0.11	0.15	0.15	0
MgO	0.63	1.91	2	0.09
CaO	1.75	4.2	4.2	0
Na2O	4.54	4.44	4.38	0.06
K2O	5.45	3.55	3.75	0.2
P2O5	0.13	0.44	0.09	0.35
Prediction based on distribution coefficients				0
Rb	138.4	88.4	92.8	4.4
Sr	279.9	603.3	621.7	18.4
Ba	1810.8	1464.6	1312.1	152.5
Y	42.7	34.8	41	6.2
Zr	422.4	295.2	306.3	11.1
Nb	56.2	37.5	43.6	6.1
Ce	191	136.3	144	7.7
Nd	61.7	62.6	48.1	14.5
Sm	11.4	11.6	8.78	2.82
Eu	2.28	2.59	3.02	0.43
Dy	5.64	6.59	4.53	2.06
Yb	3.4	3.41	2.68	0.73
Lu	0.52	0.54	0.4	0.14

Parent	990710-2			
Daughter	3-2:121997			
%	Min/Rock			
17.7	Plagioclase			
5.2	Clinopyroxene			
2.6	Orthopyroxene			
1.5	Magnetite			
0.09	Ilmenite			
0.717	Liquid Remaining			
Sum of the squares of the residuals= 0.123				
	Daughter	3-2 Rock	3-2 Calc	Residual
*SiO2	67.4	62.47	62.52	0.05
TiO2	0.8	1.15	1.15	0
Al2O3	15.81	16.17	16.16	0.01
FeO	3.51	5.52	5.52	0
MnO	0.11	0.15	0.14	0.01
MgO	0.79	1.91	1.89	0.02
CaO	2.17	4.2	4.19	0.01
Na2O	4.54	4.44	4.37	0.07
K2O	4.72	3.55	3.5	0.05
P2O5	0.14	0.44	0.1	0.34
Prediction based on distribution coefficients				0
Rb	127	88.4	92.1	3.7
Sr	331.2	603.3	620.6	17.3
Ba	1702.6	1464.6	1313.9	150.7
Y	41	34.8	41.2	6.4
Zr	425.7	295.2	330.4	35.2
Nb	34	37.5	27.8	9.7
Ce	175.8	136.3	140.7	4.4
Nd	56.3	62.6	46.6	16
Sm	10.1	11.6	8.35	3.25
Eu	2.17	2.59	2.74	0.15
Dy	5.5	6.59	4.69	1.9
Yb	2.76	3.41	2.3	1.11
Lu	0.55	0.54	0.45	0.09

APPENDIX B

Figures

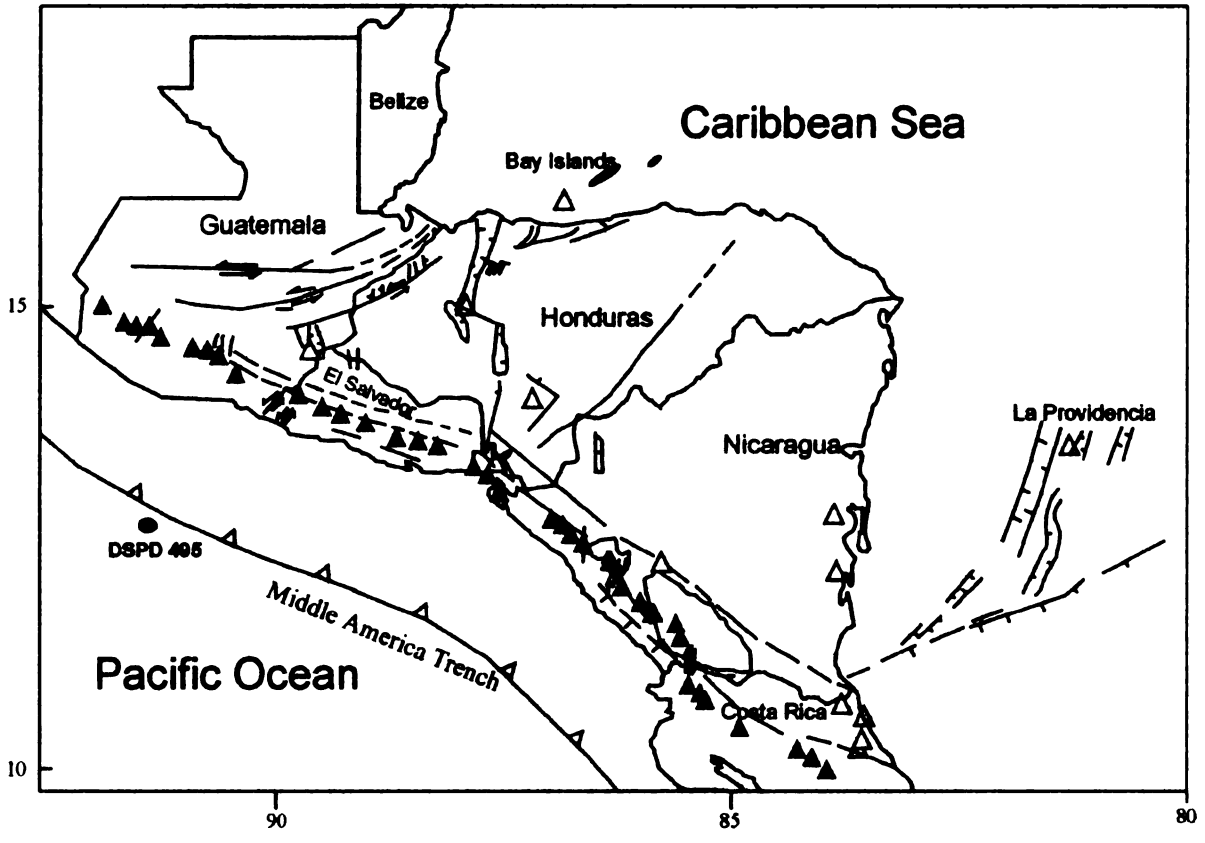

Figure 1. Tectonic map of Central American Volcanic Arc. Red circles are active arc volcanics, blue circles are back arc volcanics.

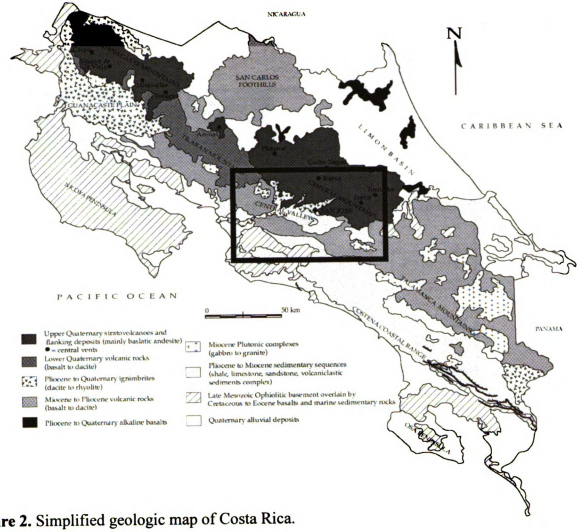

Figure 2. Simplified geologic map of Costa Rica.

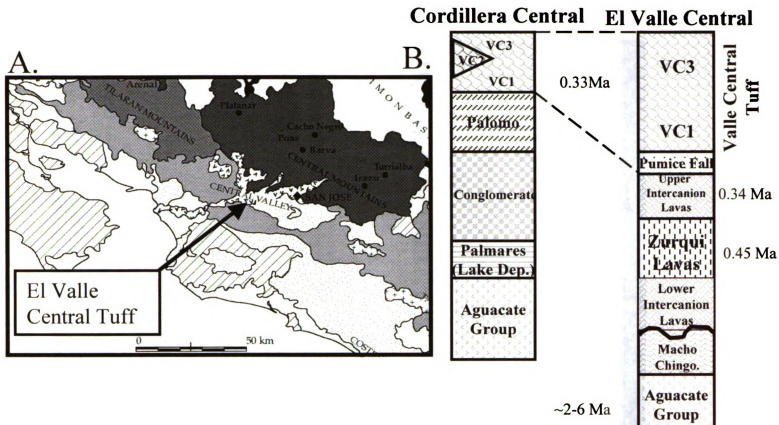

Figure 3. A. Plane view of the central valley of Costa Rica and the extent of the Valle Central tuff. San Jose, the capitol of Costa Rica is to the south-east of the tuff. The volcanoes Platanar, Poas, Barva, Irazu, and Turrialba are along the active arc to the northwest and northeast of the tuff. Modified from Tournon and Alvarado (1995). **B.** Stratigraphic correlation of theValle Central deposits and deposits to the northwest, in the Cordillera Central.

Figure 4. Photograph of the white pumice-fall unit that can be seen throughout the Valle Central.

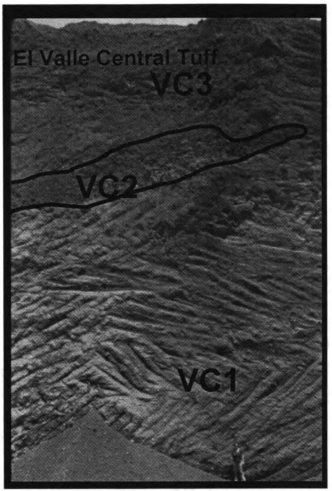

Figure 5. Photograph of the "La Garita Tuff," unit, showing all three units. Includes abundant fumerolic pipes. Person for scale.

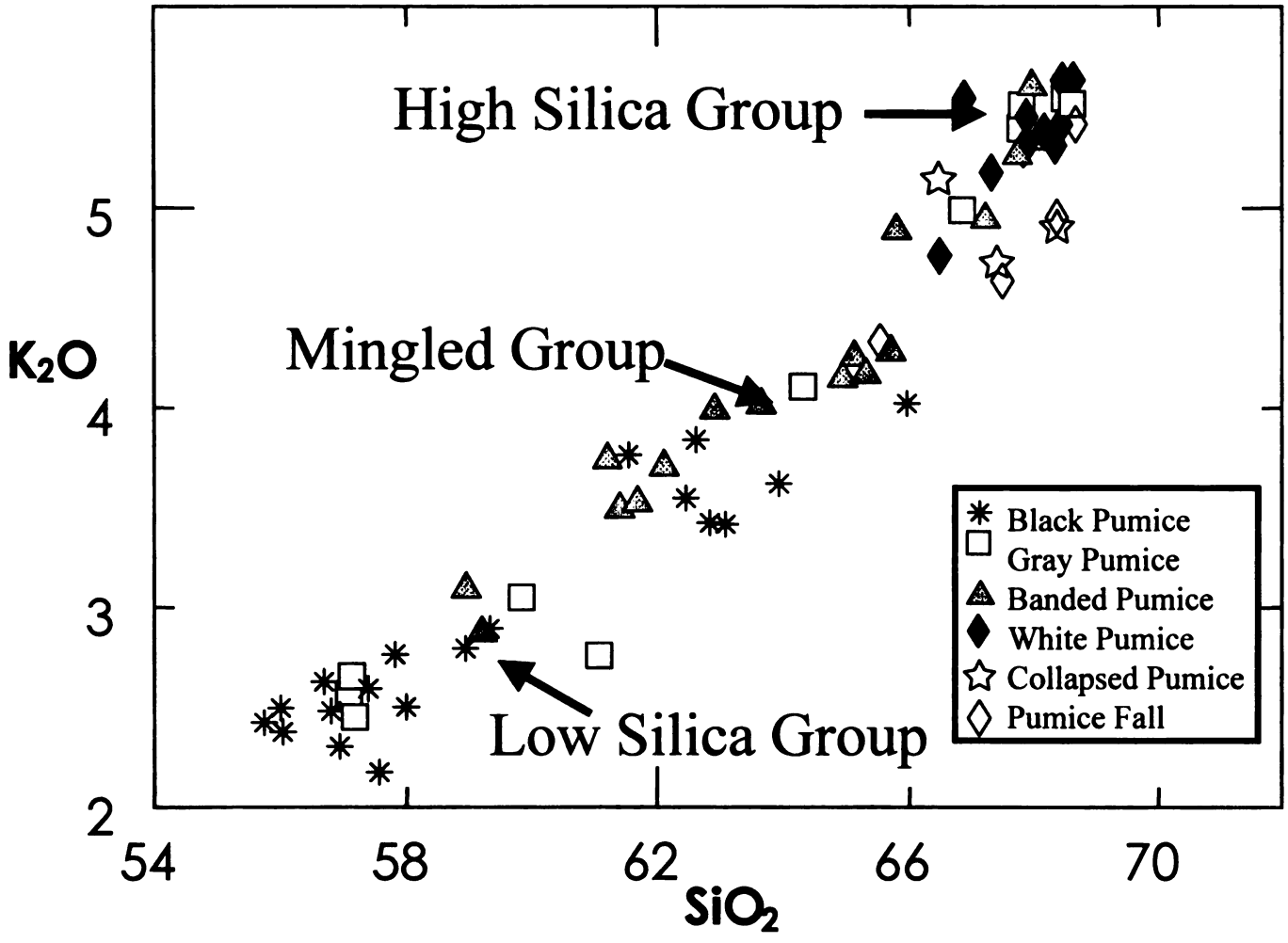

Figure 6A. Variation in pumice clast color with silica and potassium content. Black pumice and dark gray pumice are low in silica. White, light gray, and collapsed pumice are high in silica. All figures use normalized major element values.

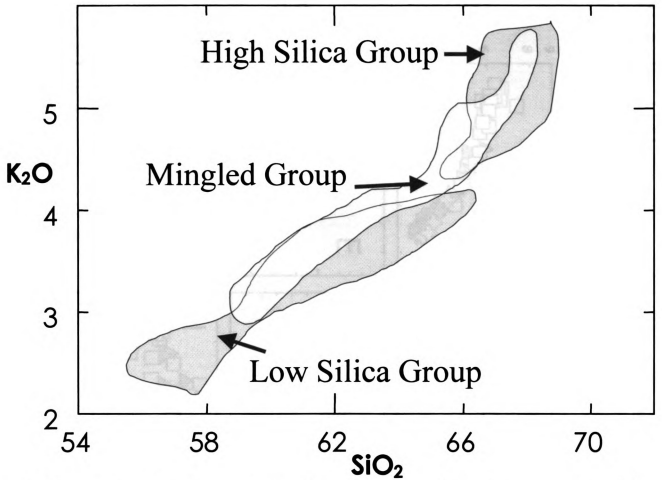

Figure 6B. Classification of pumice samples into the low-silica group, high-silica group, and mingled group within the Valle Central Tuff. Black and dark gray pumice clasts belong to the low-silica group. Banded pumice clasts belong to the mingled group. White, light gray, and collapsed pumice clasts belong to the high-silica group. All figures use normalized major element values.

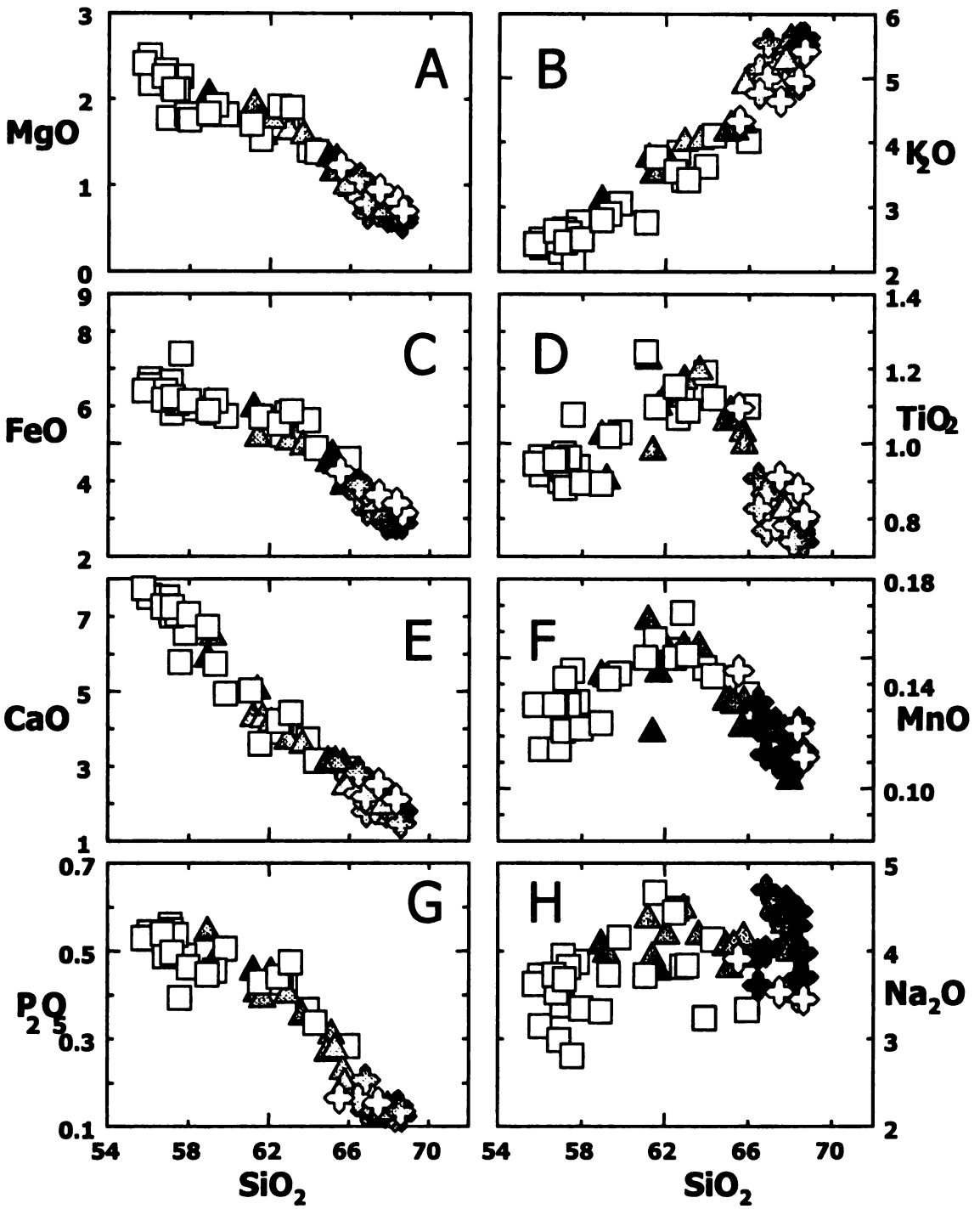

Figure 7. Major element oxide variation plots versus SiO_2 for El Valle Tuff.□ =Low-Silica Group. ◆ =High-Silica Group.▲ =Mingled-Group.

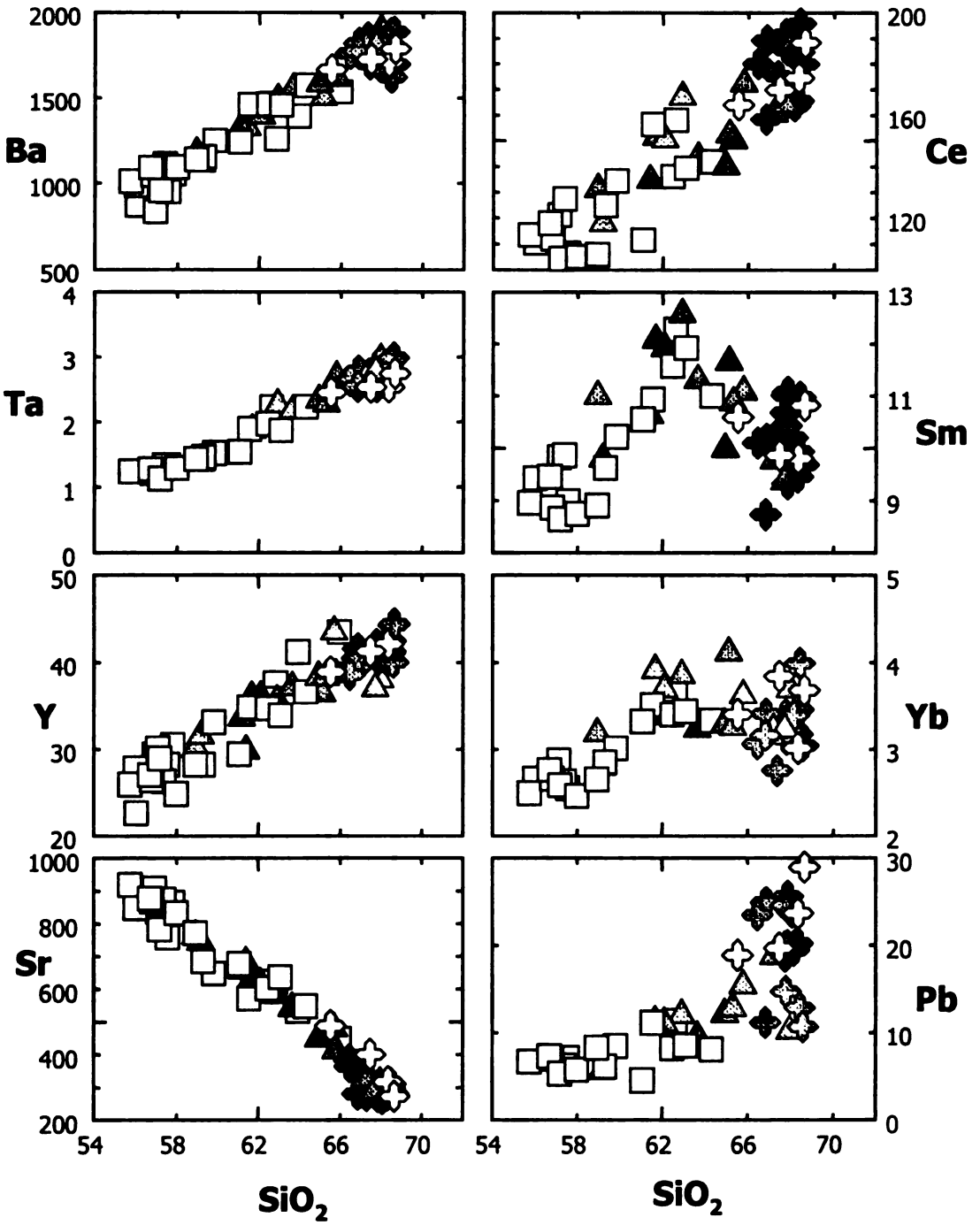

Figure 8. Trace element variation plots versus SiO_2 for El Valle Tuff□ =Low-Silica Group. ◆ =High-Silica Group. ▲ =Mingled-Group.

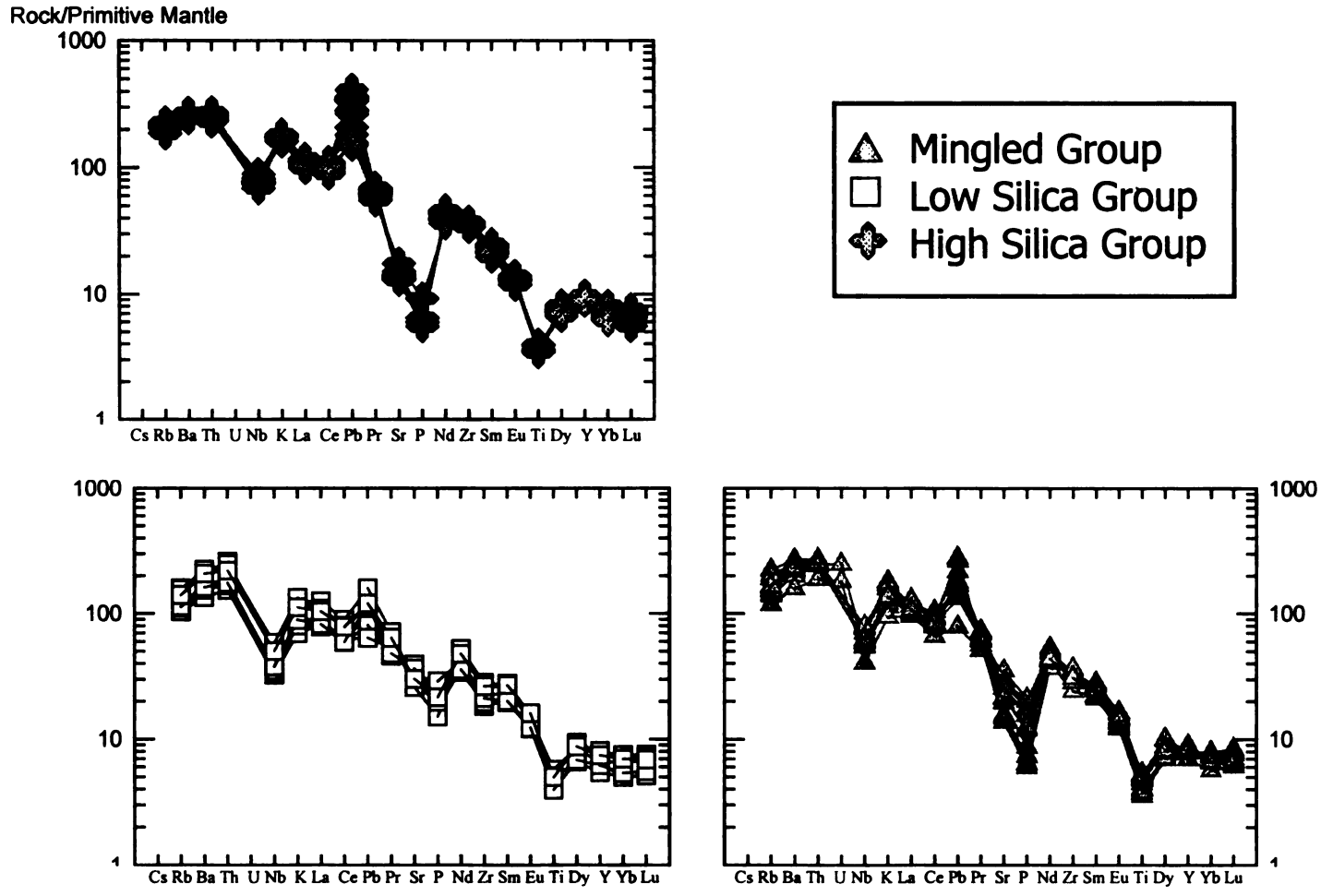

Figure 9. Spider diagram of representitive pumice clasts from the low-silica group, mingled group, and high-silica group. Note that the high silica group has a much greater depletion in P, and is enriched in the large ion lithophiles (Rb, Ba, K, Pb) in comparison to the low silica group. Normalization factors from Sun and McDonough (1989).

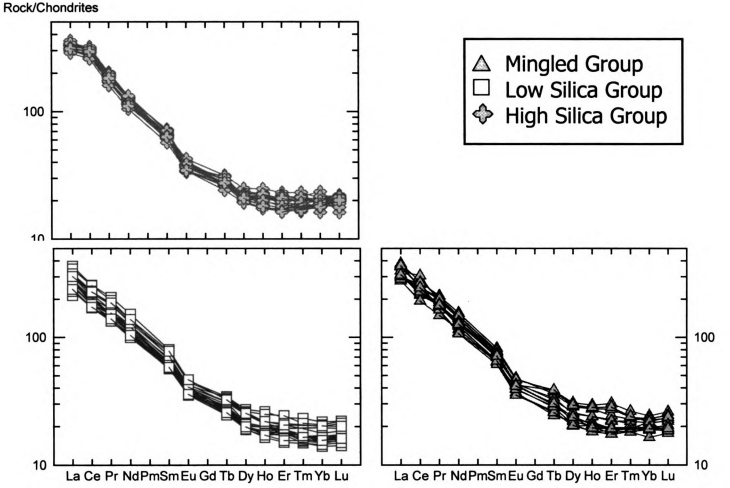

Figure 10. Rare earth element plot for representative samples from the low-silica group, high-silica group, and the mingled group. The REE pattern for all samples within thel Valle Central Tuff is very well constrained, with small degrees of variation. Normalization factors from Sun and McDonough (1989).

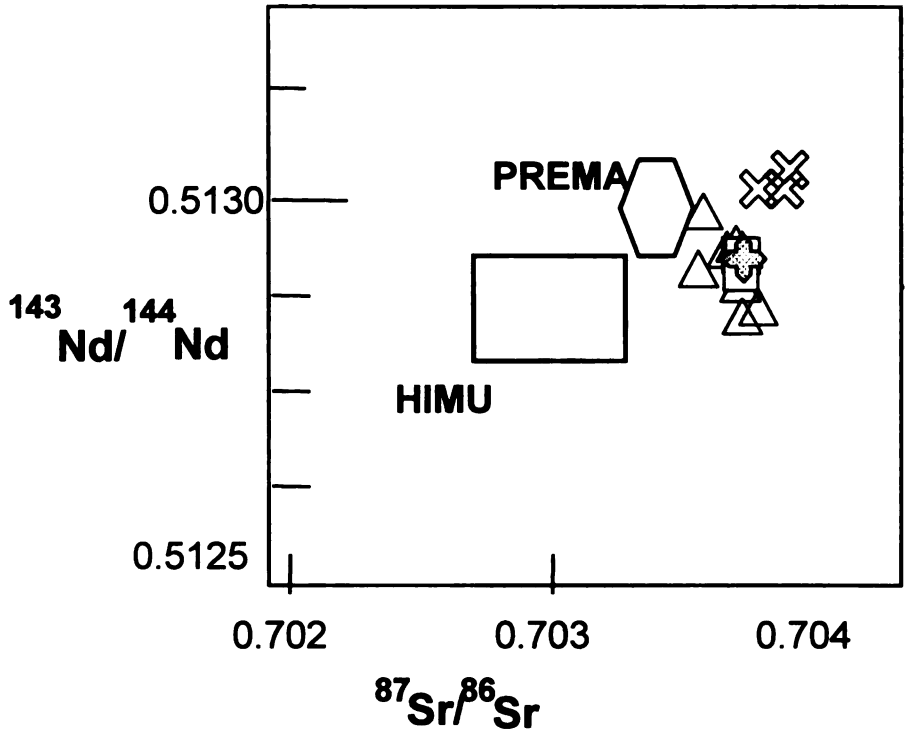

Figure 11. Sr and Nd isotope plot. Ranges indicate the isotopic character of different mantle sources. The range within El Valle Central samples is tightly constrained, regardless of silica content. The Valle Central Tuff samples plot within the range of isotopic variation seen throughout the Valle Central.

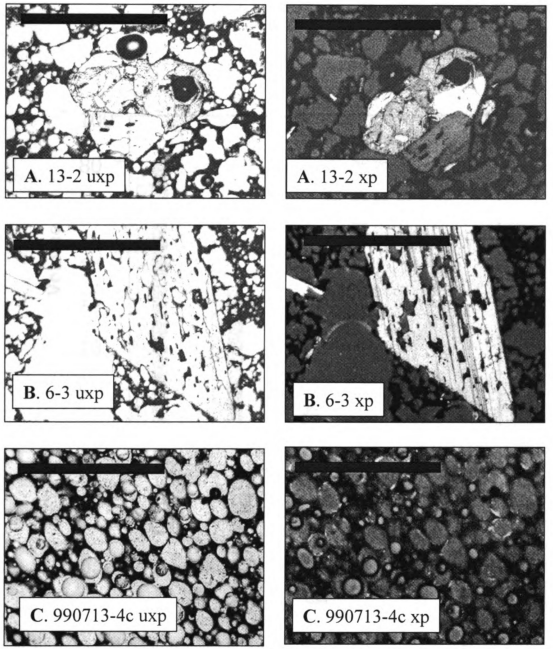

Figure 12. A. Photomicrograph of clinopyroxene phenocrysts from a black pumice clast (54 wt. % SiO_2 within the low silica group. **B**. Photomicrograph of plagioclase phenocryst from the same sample; the pock-marked texture of the crystal is referred to as "sieve" texture. **C.** Rounded vesicules in the brown glass, especially evident in nearly aphyric samples of 62 wt. % SiO_2. In all photomicrographs, the bar scale represents 1 mm. UXP= Uncrossed polars, or plane-polarized light. XP= View using crossed polars.

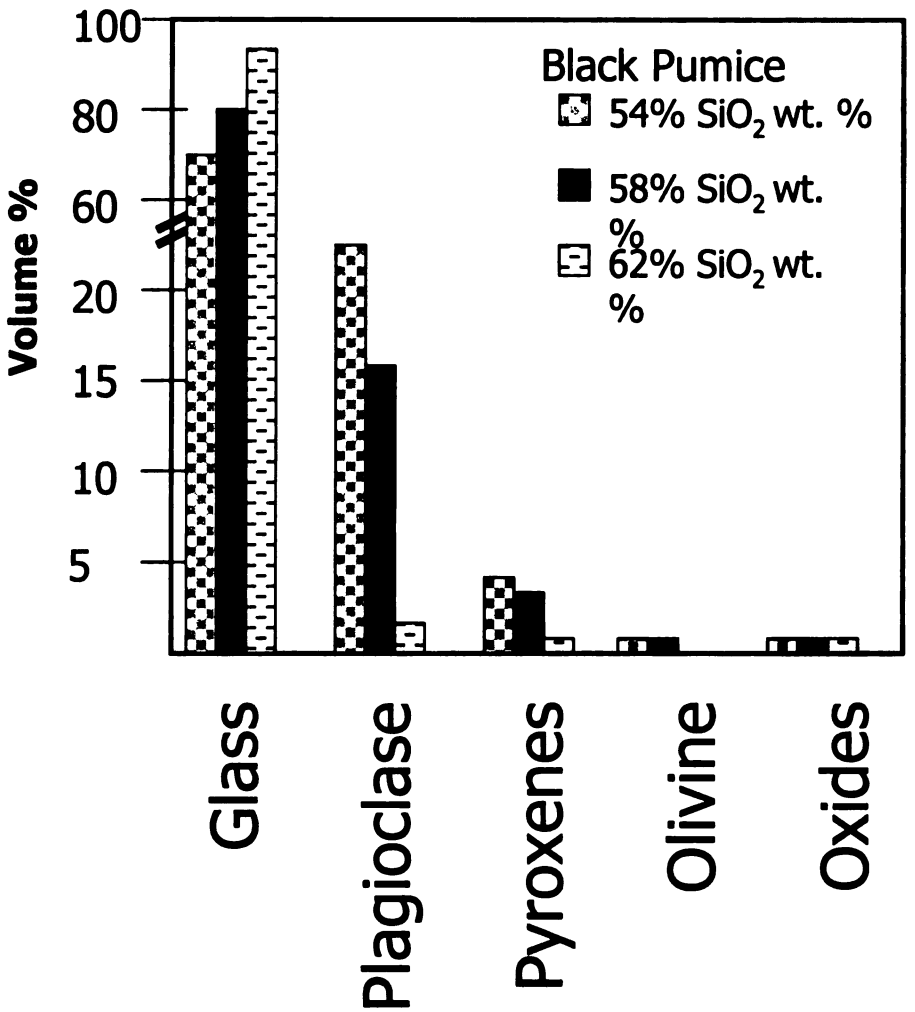

Figure 13. Phenocryst contents and variations in low-silica group black pumice. Dashed lines in vertical axis indicates a change in scale.

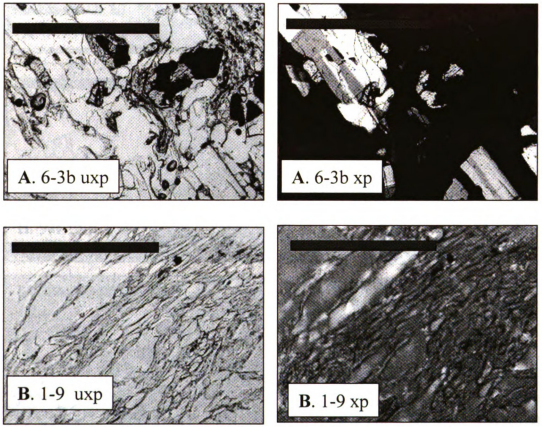

Figure 14. A. Photomicrograph of a glomopheric clot from a white pumice clast from the high silica group. **B**. Photomicrograph of glass from an aphyric, white pumice clast from the high silica group. Note the stretched and collapsed vesicules within the glass. In all photomicrographs, the bar scale represents 1 mm. UXP= Uncrossed polars, or plane-polarized light. XP= View using crossed polars.

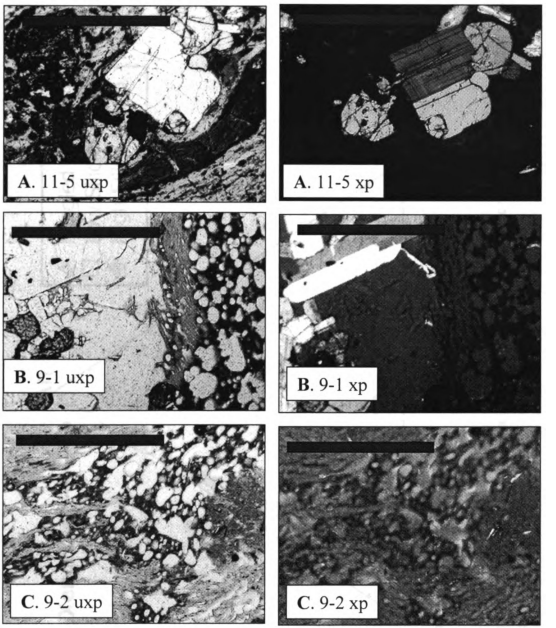

Figure 15. A. Photomicrograph of banded pumice fragments with abundant rotated and broken phenocrysts. **B**. Photomicropgraph of remnant glomopheric clot surrounded by white glass, typical of white pumice of the high-silica group, surrounded by brown glass typical of the low silica group **C.** Photomicrograph of glass in banded pumice fragments. Note that the brown glass (59-60 wt % SiO_2) retains well rounded vesicules while the white glass (69-70 wt% SiO_2) has stretched and collapsed vesicules. In all views, the scale bar represents 1 mm. UXP= Uncrossed polars, or plane-polarized light. XP= View using crossed polars.

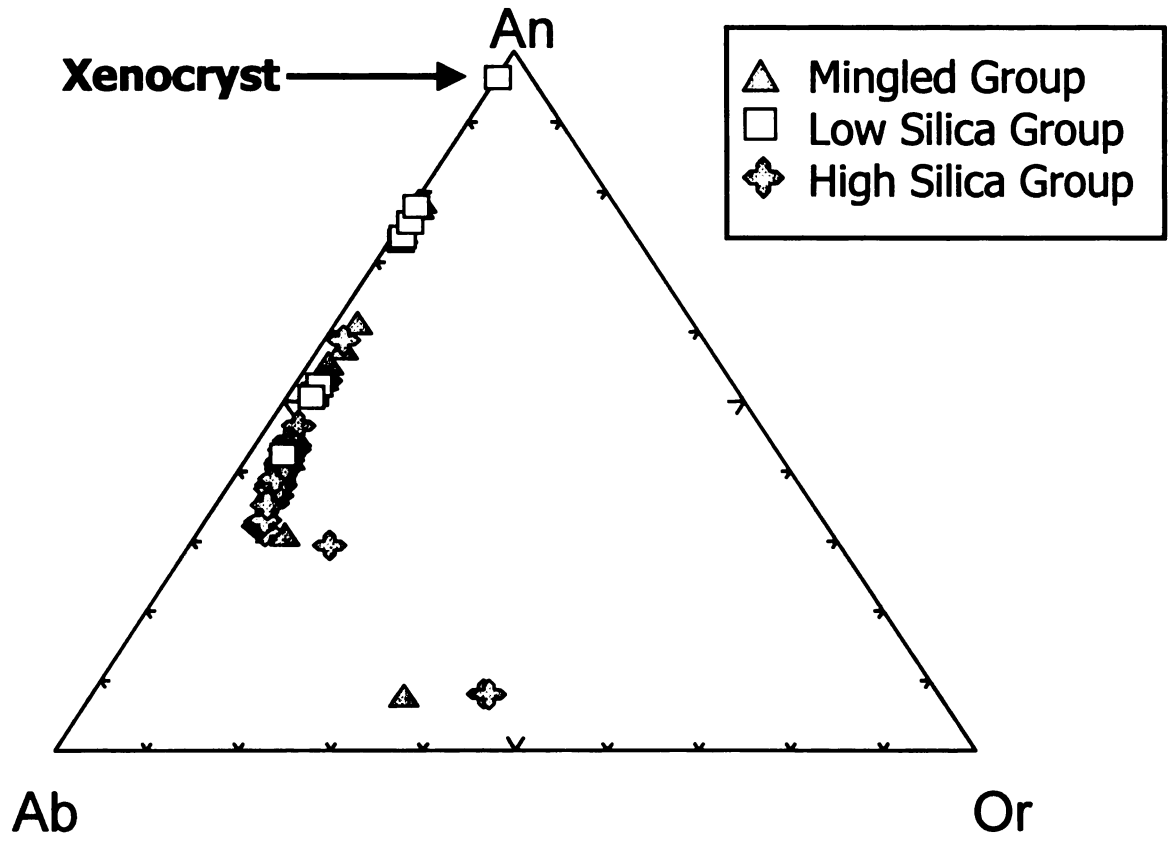

Figure 16. Ternary diagram for feldspar. Note the decrease in anorthite content of phenocrysts with increasing silica content in the whole pumice sample.

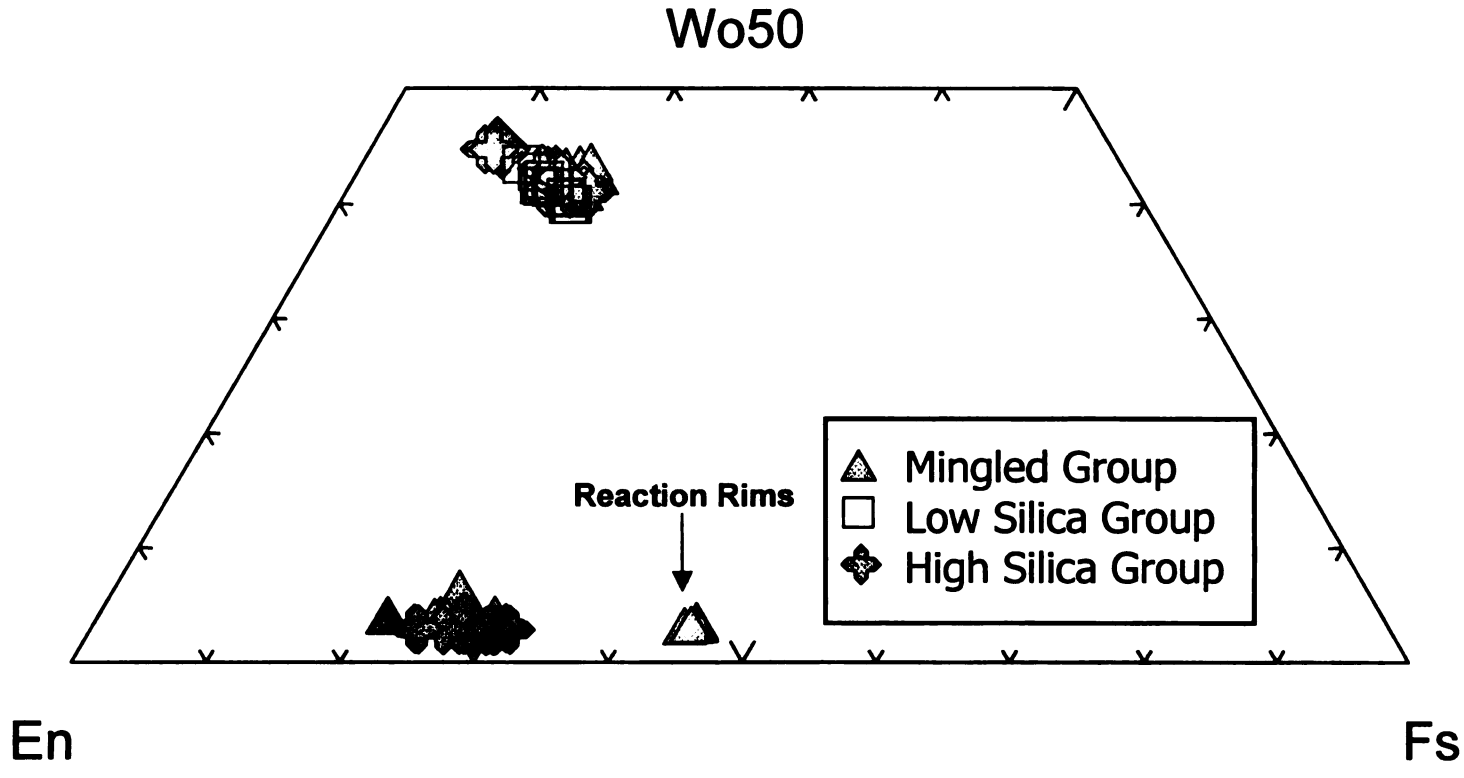

Figure 17. Pyroxene quadrilateral for the Valle Central phenocrysts. Low-silica group and high silica group augite phenocrysts have very similar compositions. High-silica group pumice clasts have orthopyroxene. Rims on orthopyroxene crystals from mingled pumice clasts are enriched in Fs.

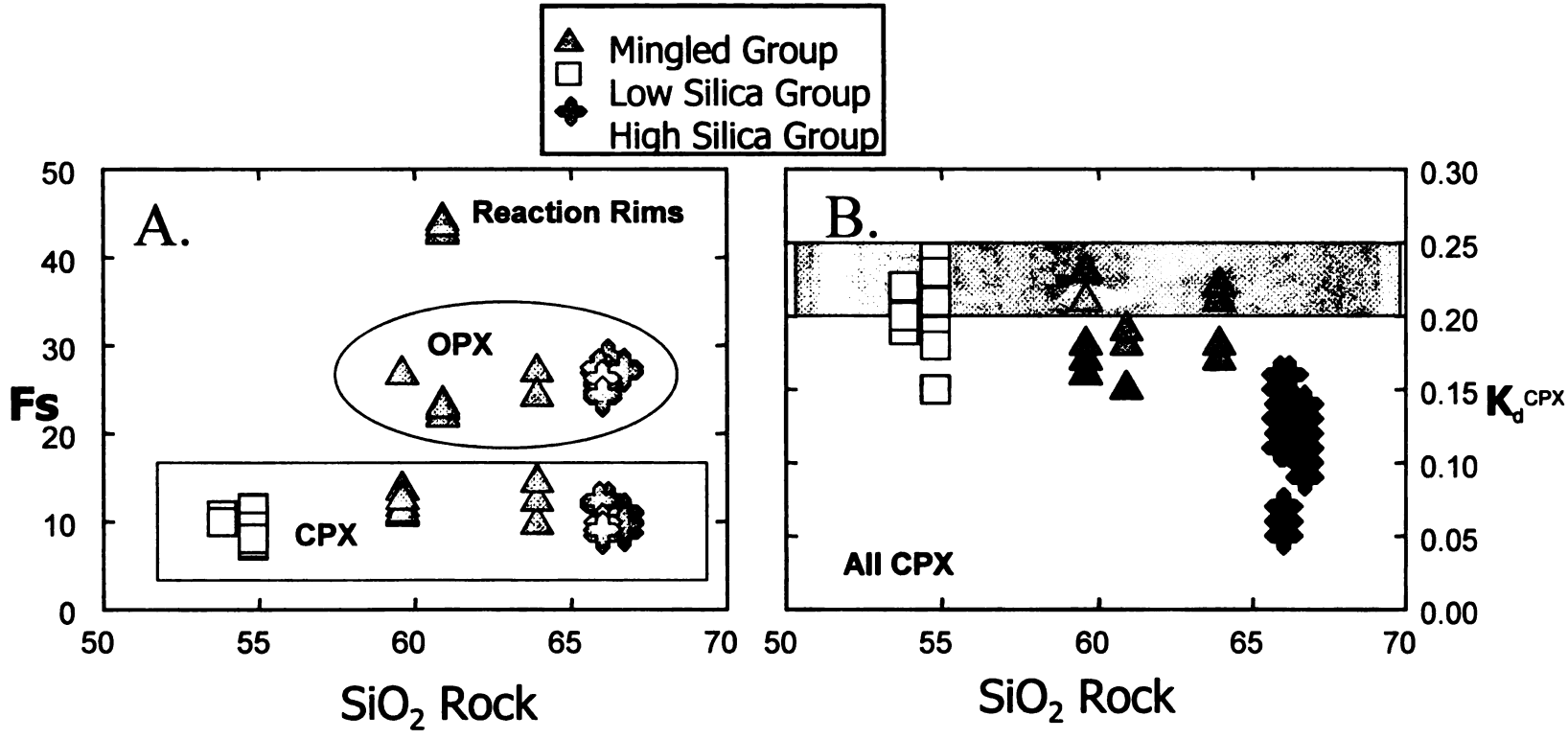

Figure 18. A. Plots of Fs content in pyroxene phenocrysts with silica content in whole pumice samples. The Fs content of pyroxenes in the low silica group (55 wt.% SiO_2) is identical for clinopyroxene phenocrysts in the high silica group (67 wt % SiO_2). Rims from mingled pumice samples are enriched in Fs. **B.** K_d values for all clinopyroxene phenocrysts versus silica content in whole pumice samples. Some phenocrysts in black, grey, and banded pumice clasts from the low silica group are in equilibrium with the liquid.

A.

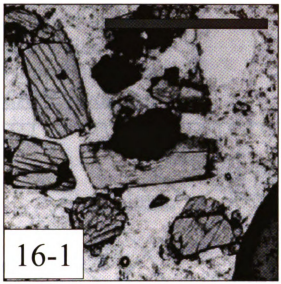

B.

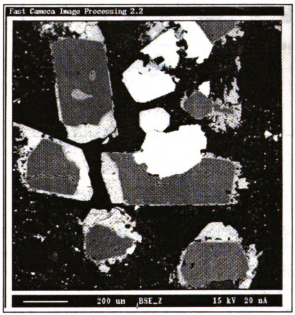

Figure 19. A. Photomicrograph in plane polarized light of a cluster of orthopyroxene phenocrysts within a banded pumice fragment. **B.** Photomicrograph using backscattered electron imaging to see reaction rims around the orthopyroxene phenocrysts. The phenocryst cores are depleted in Fe and enriched in Mg compared to the phenocryst rims.

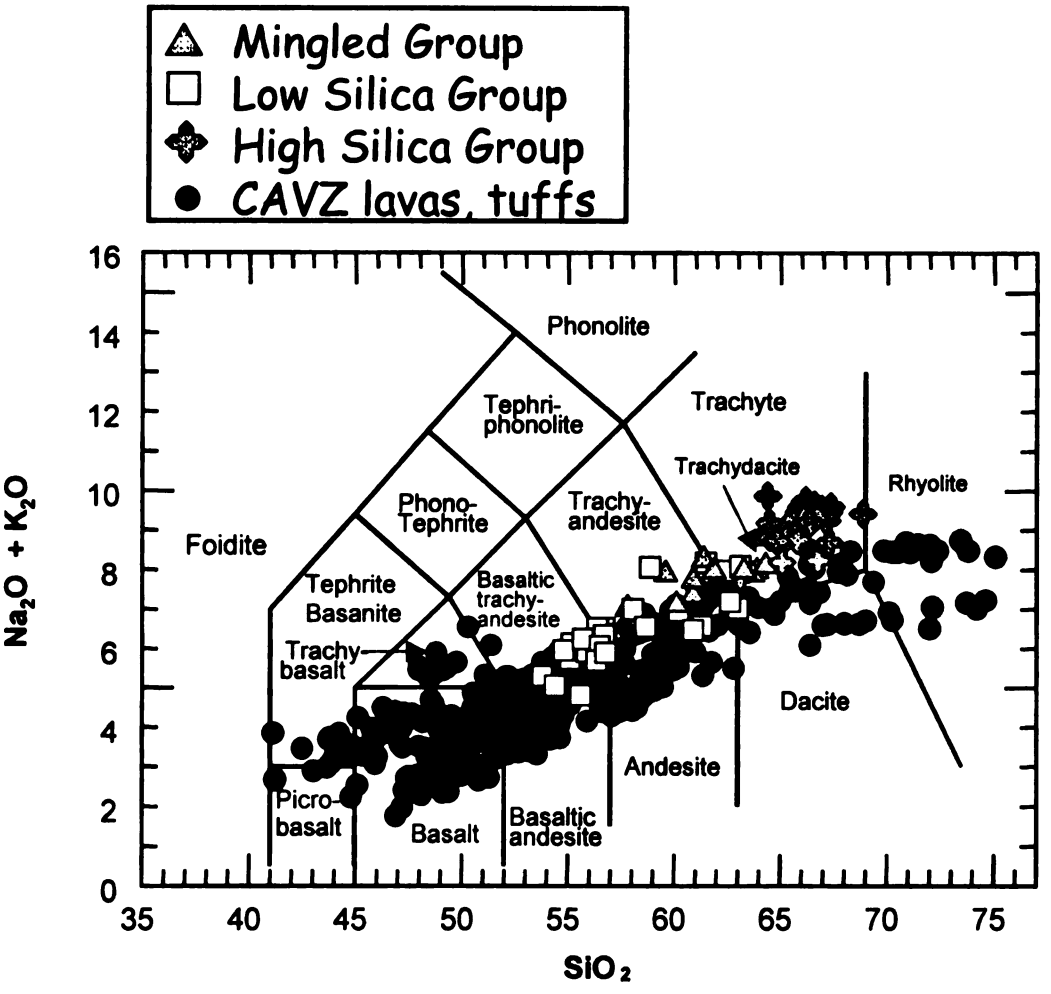

Figure 20. TAS classification of LeBas et al. (1986) for the Central American Volcanic arc, including the Valle Central Tuff. CAVZ indicates basalts, basaltic andesites, andesites, and rhyolites from CENTAM database, and from Kempter (1997). Note that the Valle Central Tuff is enriched in K compared to other volcanic products from along the Central American Volcanic arc.

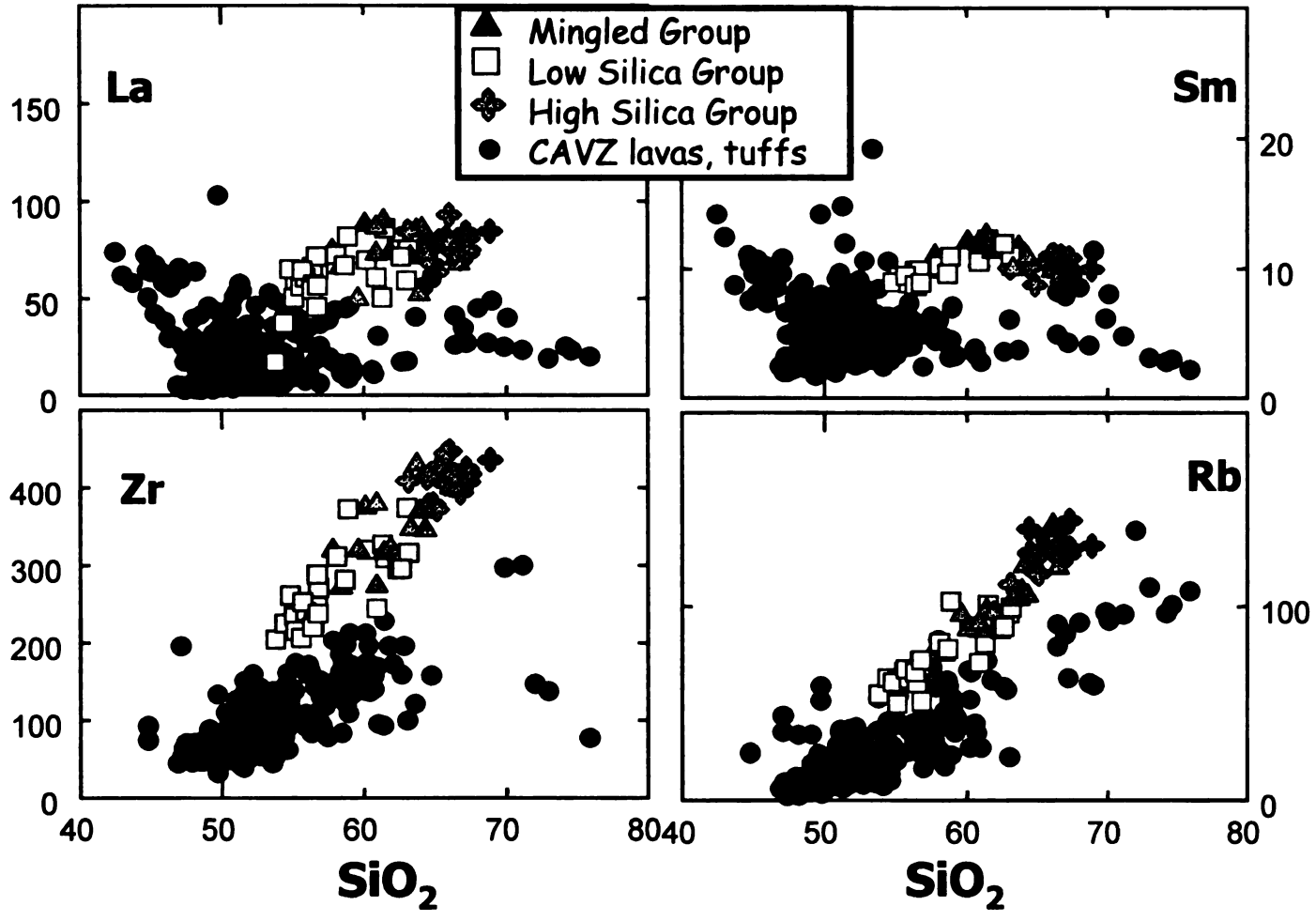

Figure 21. Plots of SiO_2 vs. selected trace elements. CAVZ indicates basalts, basaltic andesites, andesites, and rhyolites from CENTAM database and from Kempter (1997). Note that El Valle Central Tuff is enriched compared to other volcanic products from along the Central American Volcanic arc.

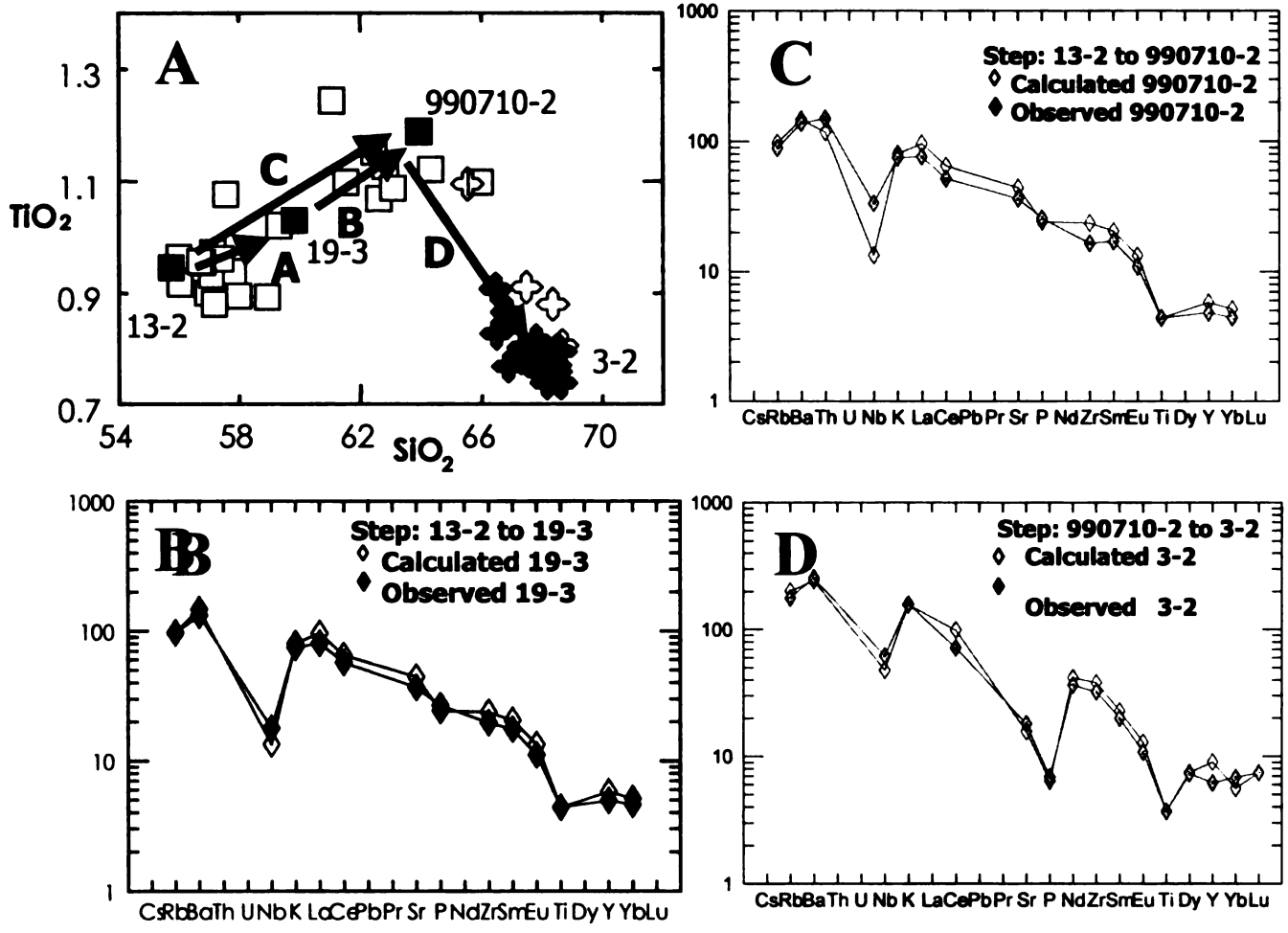

Figure 22. A. Liquid lines of decent for batch fractional crystallization models. **B**. Spider diagram of observed and calculated (based on multiple linear regression) for Steps A and B in A. **C**. Spider diagram of observed and calculated (based on multiple linear regression) for Step C. **D**. Spider diagram of observed and calculated (based on multiple linear regression) for Step D.

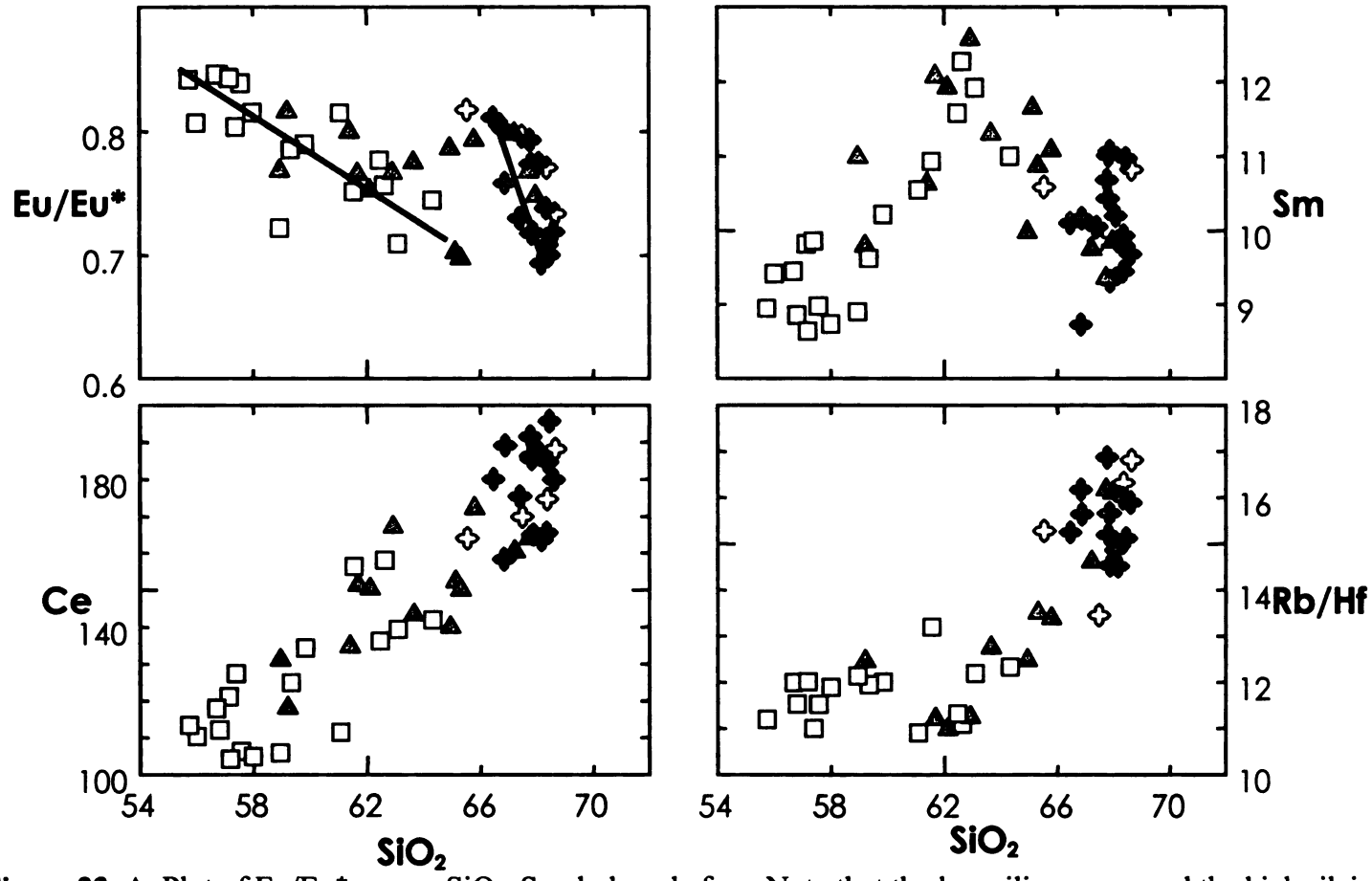

Figure 23. A. Plot of Eu/Eu* versus SiO_2. Symbols as before. Note that the low silica group and the high silcia group plot in two distinct trends, implying that fractional crystallization is not the controlling process on magma differentiation. Lines represent a best fit line for each group. **B.** Ce is representative of other light rare earth elements, incompatible in both the low and high silcia groups. **C.** Sm is representative of the middle rare earth elements; incompatible in the low silica group liquid, but behaving as a more compatible element in the high silica group liquid. **D.** Rb/Hf variation between the two groups could indicate a crustal source for the high-silica group.

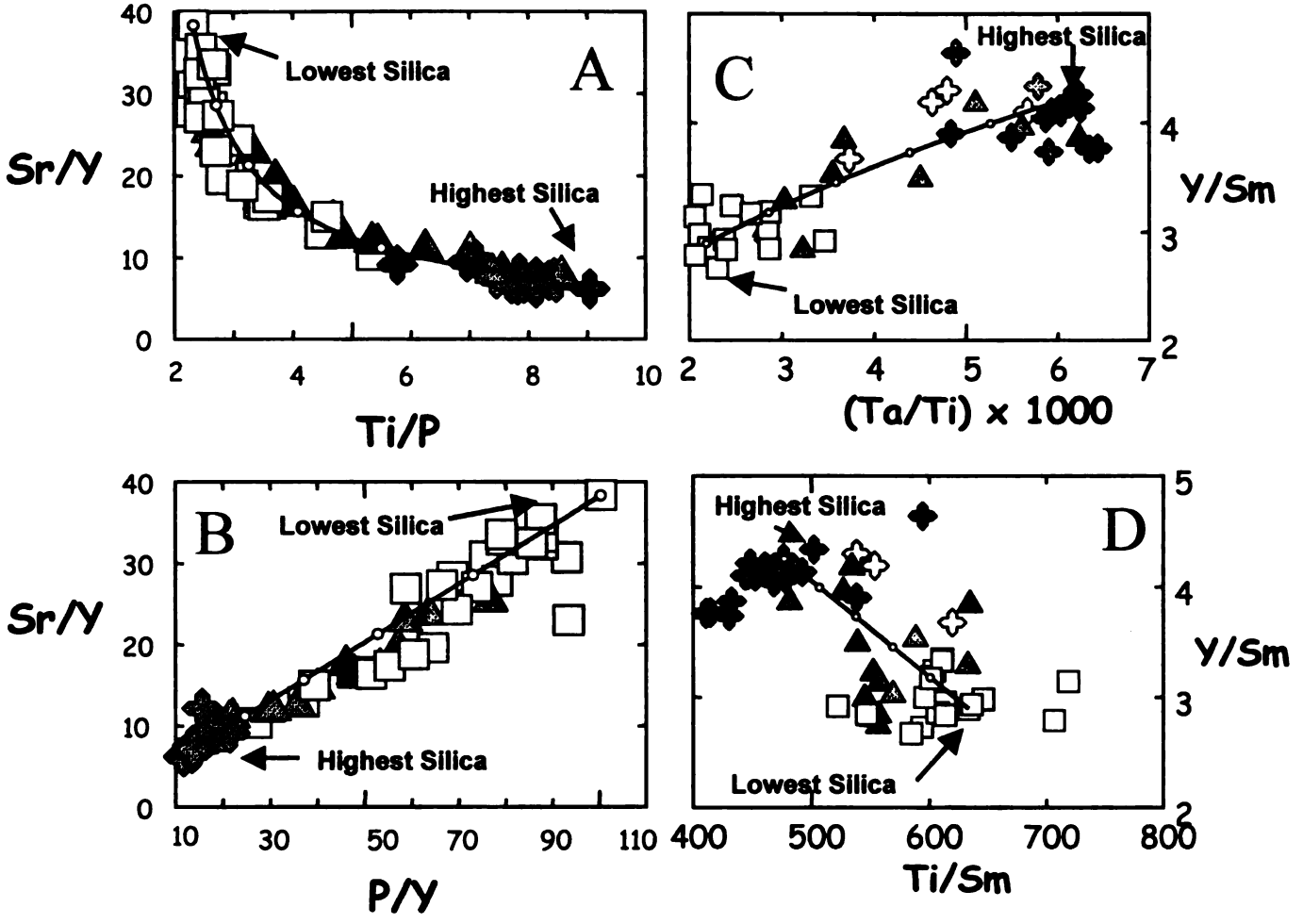

Figure 24. Element ratio-ratio plots as a test for magma mixing. Symbols as before. **A and C**. Plots of Sr/Y vs Ti/P and Ta/Ti vs. Y/Sm. Ta/Ti ratios are multiplied by 1000 for easier plotting. All the banded samples fall on a hyperbola defined by mixing the high and low silica extreme compositions. **B and D.** Plots of Sr/Y vs. P/Y and Y/Sm vs. Ti/Sm. All plots support magma mingling for the Mingled group. 10C and 10D do not support magma mingling for the low or high silica group. Tic marks represent mixing increments of 20%.

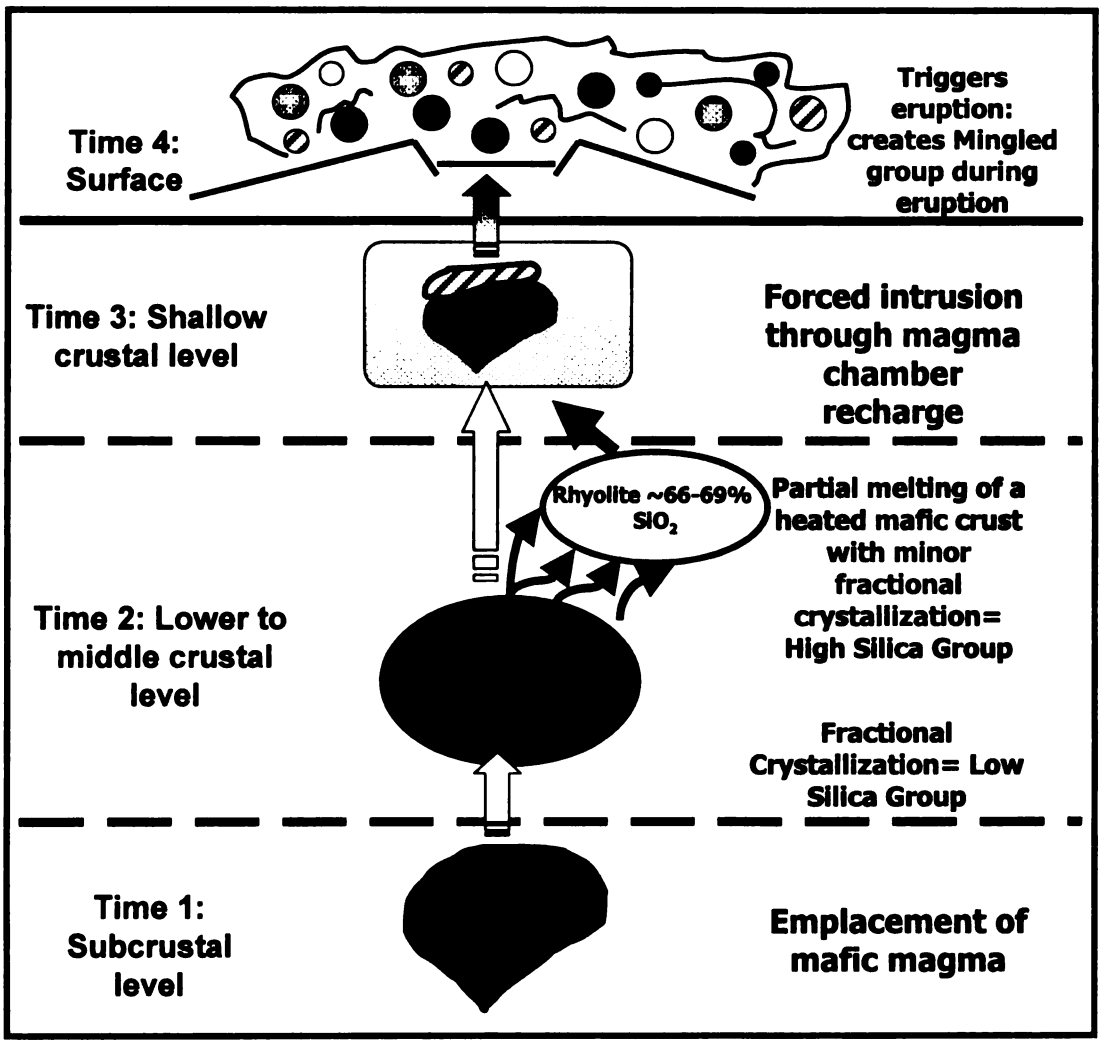

Figure 25. Schematic model of the evolution of El Valle Central Tuff.

APPENDIX C

Equations

Eu anomalies can be evaluated by calculating Eu#, which is the value of Eu calculated from the linear equation of the line connecting Sm and Tb on a REE plot (Appendix C). Eu/Eu* is a measure of the Eu anomaly. To calculate the Eu/Eu* anomaly, it is necessary to use the chondrite normalized values of Sm, Eu, and Tb. Then, given equations 1, 2, and 3, it is possible to determine the **a** (eq. 4) and **b** (eq. 5) for the linear equation of Sm, Eu, and Tb on an REE plot.

$$\log_{10}(\text{Tb}) = \mathbf{a}*65 + \mathbf{b} \tag{1}$$

$$\log_{10}(\text{Eu}^*) = \mathbf{a}*63 + \mathbf{b} \tag{2}$$

$$\log_{10}(\text{Sm}) = \mathbf{a}*62 + \mathbf{b} \tag{3}$$

$$\mathbf{a} = \frac{\log_{10}(\text{Sm}) - \log_{10}(\text{Tb})}{(62-65)} \tag{4}$$

$$\mathbf{b} = \log_{10}(\text{Sm}) - (a*62) \tag{5}$$

Through reorganization and substitution, it is possible to calculate the value of Eu/Eu*, or the measure of the Eu anomaly (eq. 6).

$$\frac{\text{Eu}}{\text{Eu}^*} = \frac{\text{Eu}}{\log^{-1}(\mathbf{a}*63 + \mathbf{b})} \tag{6}$$

BIBLIOGRAPHY

BIBLIOGRAPHY

Alvarado GE, Carr MJ (1993) The Platanar-Aguas Zarcas volcanic centers, Costa Rica: spatial- temporal association of Quaternary calc-alkaline and alkaline volcanism. Bull Volcanol 55:443-453.

Alvarado GE, Kussmaul S., Chisea S. Guillot PY, Appel H., Wörner G, Rundle C (1992): Cuadro cronoestrátigrafico de las rocas ígneas de Costa Rica basado en dataciones radiométricas K-Ar y U-Th. J. of South American Earth Sciences 6/3: 151-168.

Bacon CR, Hirschmann MM (1988) Mg/Mn partitioning as a test for equilibrium between coexisting Fe-Ti oxides. American Mineralogist 73: 57-61.

Baker BH, McBirney AR (1985) Liquid fractionation Part III: Geochemistry of zoned magmas and the compositional effects of liquid fractionation. J. Volc. Geo. Res 24: 55-81.

Beard JS, Lofgren GE (1991) Dehydration melting and water-saturated melting of basaltic and andesitic greenstones and amphibolites at 1, 3, and 6.9kb. J. Petrol 32: 365-401.

Bergantz GW (1989) Underplating and partial melting; Implications for melt generation and extraction. Science 245: 1,093-1,095.

Best MG (1975) Migration of hydrous fluids in the upper mantle and potassium variation in calc-alkalic rocks. Geology 3/8: 429-432.

Borg LE, Clynne MA (1998) The petrogenesis of felsic calc-alkaline magmas from the southernmost Cascades, California: Origin by partial melting of basaltic lower crust, J. Petrol. 39: 1197-1222.

Brophy JG, Whittington CS, Young-Rok P (1999) Sector-zoned augite megacrysts in Aleutian high alumina basalts: implications for the conditions of basalt crystalliztion and the generation of calc-alkaline series magmas. Cont. Min. Pet. 135: 277-290.

Bryan WB, Finger LW, Chayes F (1969) Estimating proportions in petrographic mixing equations by least squares approximation, Science, 163: 926-927.

Carr MJ (1984) Symmetrical and segmented variation of physical and geochemical characteristics of the Central American volcanic front. J. Volc. Geo. Res. 20: 231-252.

Carr MJ, Feigenson MD, Bennett EA (1990) Incompatible element and isotopic evidence for tectonic control of source mixing and melt extraction along the Central American Arc. Cont. Min. Pet. 105: 369-380.

Chiesa S, Civelli G, Gillot PY, Alvarado GE (1992) Explosive volcanic activity associated to Guayabo-Miravalles Cladera Complex (Cordillera de Guanacaste, Costa Rica). International Geological Congress, Abstracts—Congress, 29: 501.

Cigolini C (1998) Intracrustal origin of Arenal basaltic andesite in the light of solid-melt interactions and related compositional buffering. J. Volc. Geo. Res 86: 277-310.

Cigolini C, Kudo AM, Brookins DG, Ward D (1991) The petrology of Poas Volcano lavas; basalt-andesite relationship and their petrogenesis with the magmatic arc of Costa Rica. J. Volc. Geo. Res. 48: 367-384.

Coleman DS, Glazner AF, Miller JS, Bradord KJ, Frost TP, Joye JL, Bachl CA (1995) Exposure of a Late Cretaceous layered mafic-felsic magma system in the central Sierra Nevada batholith, California: Cont. Min. Pet. 120: 129-136.

Criss JW (1980) Fundamental parameters calculations on a laboratory microcomputer, Advances in X-ray Analysis 23: 93-97.

de Boer JA, Drummnond MS, Bordelon MJ, Defant MJ, Bellon H, Maury RC (1995) Cenozoic magmatic phases of the Costa Rican island arc (Cordillera de Talamanca), GSA Special Paper 295:35-55.

Defant MJ, Jackson T, Drummond MS, de Boer JA, Bellon H, Feigenson M, Maury R, Stewart R. (1992) The geochemistry of young volcanism throughout western Panama and southeastern Costa Rica: an overview. J. Geol. Soc. Lon. 149: 569-579.

Defant MJ, Drummond MS (1990), Derivation of some modern arc magmas by melting of young subducted lithosphere. Nature 347: 662-665.
DeMets C, Gordon RG, Argus DF, Stein S (1990) Current plate motions. Geophysical Journal International 101:425-478.

de Silva SL, Wolff JA (1995) Zoned magma chambers: the influence of magma chamber geometry on sidewall convective fractionation. J. Volc. Geo. Res. 65: 111-118.

Echandi E (1981) Unidades volcánicas de la vertiente norte de la cuenca de Río Virilla. Tesís Lic. Escuela de Geología-Universidad de Costa Rica, 123 pp.

Edwards C, Menzies M, Thirlwall M (1991) Evidence from Muriah, Indonesia for the interplay of supra-subdcution zone and intraplate processes in the genesis of potassic alkaline magamas. J. Petrol. 32/3: 555-592.

Feely TC, Davidson JP (1994) Petrology of calc-alkaline lavas at Volcan Ollague and the origin of compositional diversity at central Andean stratovolcanoes. J. Petrol. 35: 1295-1340.

Feigenson MD, Carr MJ (1993) The source of Central American lavas: inferences from geochemical inverse modeling. Cont. Min. Pet. 113: 226-235.

Fournelle JH, Marsh BD, Myers JD (1994) Age character and significance of Aleutian arc volcanism. The Geology of North America V. G-1, The Geology of Alaska, Geological Society of America 723-758.

Geist D, Naumann T, Larson P (1998) Evolution of Galapoagos magmas: mantle and crustal fractionation without assimilation. J. Petrol. 39: 953-971.

Gill J (1981) Orogeneic Andesites and plate tectonics. New York, Springer-Verlag.

Herrstrom EA, Reagan MK, Morris JD (1995) Variations in lava composition associated with flow of asthenosphere beneath southern Central America. Geology 23/7: 617-620.

Hildreth W (1981) Gradients in silicic magma chambers: Implications for lithospheric magmatism. Journal of Geophysical Research 86: 10,153-10,192.

Hildreth W (1983) The compositionally zoned eruption of 1912 in the Valley of Ten Thousand Smokes, Katmai National Park, Alaska. J. Volc. Geo. Res V. 18:1-56.

Jakes P, White A (1972) Major and trace element abundances in volcanic rocks of orogenic areas. Geol. Soci. Amer. Bull. 83:29-40.

Kempter KA (1997) Geologic evolution of the Rincón de la Vieja volcanic complex, NW, Costa Rica. Ph.D. dissertation, University of Texas, Austin, Texas 191pp.

Kolarsky RA, Mann P, Monero W (1995) Island arc response to shallow subduction of the Cocos Ridge, Costa Rica. GSA Special Paper 295: 235-262.

Kussmaul S (1988) Comparación petrológica entre el piso volcánico del Valle Central y la Cordillera Central de Costa Rica. Rev. Ciencia y Tecnologia 12/ 1-2: 109-116.

Kussmaul S, Sprechmann (1982) Estratigrafia de Costa Rica (America Central), II: Unidades litoestratigraficas igneas. Actas, 5, Congr. Latinoameric. Geol., Buenos Aires 1: 73-79.

Kussmaul S, Tournon J, Alvarado GE(1994) Evolution of the Neogene to Quaternary igneous rocks of Costa Rica. Stuttgart, Profil 7: 97-123.

LeBas MJ, Le Maitre RW, Streckeisen A, Zanettin B (1986) A chemical classification of volcanic rocks based on the total alkali-silica diagram. J. Petrol. 27: 745-50.

Le Bel L, Cocherie A, Baubron J, Fouillac A, Hawkesworth C (1985) A high-K, Mantle derived plutonic suite from 'Linga,' near Arequipa (Peru). J. Petrol 26/1: 124-148.

Leeman WP, Carr MJ, Morris JD (1994) Boron geochemistry of the Central American volcanic arc: constraints on the genesis of subduction related magmas. Geochimica Cosmochimica Acta, 58:149-168.

Marsh BD, Carmichael IS (1974) Benioff Zone magmatism. Journal of Geophysical Research 79/8: 1196-1206.

Marsh BD (1984) Mechanics and energetics of magma formation and ascent *in*, Studies in Geophysics, Explosive Volcanism: Inception, Evolution and Hazards, Boyd, F.R., ed., National Academy Press, Washington, D.C.: 67-83.

Marshall JS, Idleman, BD (1999) $^{40}Ar/^{39}Ar$ Age constraints on Quaternary landscape evolution of the Central Volcanic Arc and Orotina Debris Fan, Costa Rica. GSA Annual Meeting Abstracts.

Martin D, Griffiths RW, Campbell IH (1987) Compositional and thermal convection in magma chambers. Cont. Min. Pet. 96: 465-475.

McBirney AR, Nilson RH (1986) Reply to "Liquid collection in sidewall crystallization of magma: A comment on 'liquid fractionation'" by S.A. Morse. J. Volc. Geo. Res. 30: 163-168.

Metcalf RV, Smith EI, Walker JD, Reed RC, Gonzales DA (1995) Isotopic disequilibrium among commingled hybrid magmas: evidence for a two-stage magma mixing-commingling process in the Mt. Perkins pluton, Arizona: J. Geology 103: 509-527.

Meen JK (1987) Formation of shoshonites from calcalkaline basalt magmas: geochemical and experimental constrains from the type locality. Cont. Min. Pet. 97: 333-351.

Mills JG Jr, Saltoun BJ, Vogel TA (1997) Magma batches in the Timber Mountain Magmatic System, Southwestern Nevada volcanic Field, Nevada, USA. J. Volc. Geo. Res. 178: 185-208.

Mittlefehltd D, Miller CF (1983) Geochemistry of the Sweetwater Wash Pluton, California; implications for "anomalous" trace element behavior during differentiation of felsic magmas. Geochimica et Cosmochimica Acta 47: 109-124.

Patino LC (1997) Geochemical characterization of Central American subduction zone: slab input, output from the volcanoes, and slab-mantle interactions. Ph.D. Thesis, Rutgers University. New Brunswick, NJ.

Patino LC, Carr MJ, MD Feigenson, in press. Local and regional variations in Central American lavas controlled by variations in subducted sediment input Cont. Min. Pet

Price R, Stewart R, Woodhead J, Smith I (1999) Petrogenesis of high-K arc magmas: Evidence from Egmont Volcano, North Island, New Zealand. J. Petrol. 40 (1): 167-197.

Plank T, Langmuir C (1988) An evaluation of the global variations in the major element chemistry of arc basalts. Earth Planet. Sci. Lett 90: 349-370.

Protti MF, Guendel, McNally, K (1995): Correlation Between the Age of the Subducting Cocos Plate and the Geometry of the Wadati-Benioff Zone Under Nicaragua and Costa Rica. GSA Special Paper 295: 309-326.

Rapp RP, Watson EB (1995) Dehydration melting of a mteabasalt at 8-32 kbar: Implications for continental growth and crust-mantle recycling. J. Petrol. 36/4: 891-931.

Reagan MK, Gill JB (1989) Coexisiting calcalkaline and high-niobium basalts from Turrialba Volcano, Costa Rica: Implications for residual titanites in arc magma sources. J. of Geophys. Res. 94: 4619-4633.

Reagan MK, Morris JD, Herrstrom EA, Murrell MT, (1994) Uranium series and beryllium isotope evidence for an extended history of subduction modification of the mantle below Nicaragua: Geochimica et Cosmochimica Acta 58: 4199-4212.

Roberts MP, Clemens JD (1993) Origin of high-potassium calc-alkaline, I-type granitoids. Geology 21: 825-828.

Sawyer EW (1994) Melt segregation in the continental crust. Geology 22: 1,019-1,022.

Sachs PM, Alvarado GE (1996) Mafic metaigneous lower crust beneath Arenal Volcano (Costa Rica): Evidence from Xenoltihs. Bol. Obs. Vulc. Arenal 6/11-12: 71-78.

Singer BS, Myers JD, Frost CD (1992) Mid-Pleistocene lavas from Sequam volcanic center, central Aleutian arc: closed-system fractional crystallization of a basalt to rhyodacite eruptive suite. Cont. Min. Pet. 110: 87-112.

Sisson TW, Grove TL (1993) Experimental investigation of the role of H2O in calc-alkaline differentiation and subduction zone magmatisim. Cont. Min. Pet. 113: 143-166.

Spera FJ, Yuen DA, Greer JC, Sewell G (1986) Dynamics of magma withdrawal from stratified magma chambers. Geology 14: 723-726.

Stern R, Jackson M., Fryer C, Ito E (1993) O, Sr, Nd, and Pb isotopic composition of the Kasuga cross-chain in the Marianas arc: a new prespective on the K-h relationship. Earth Planet. Sci. Lett. 119: 459-475.

Smith RL (1979) Ash flow magmatism. GSA Special Paper 180: 5-27.

Sun S, McDonough WF (1989) Chemical and isotopic systematics of oceanic basalts: implications for mantle composition and processes, in Magmatisim in the Ocean Basins, eds: AD Saunders and MJ Norry, GSA Special Publications 42:313-345.

Tatsumi Y, Hamilton DL, Nesbitt RW (1986) Chemical characteristics of fluid phase released from a subducted lithosphere and origin of arc magmas: evidence from high-pressure experiments and natural rocks. J. Volc. Geo. Res. 29: 293-203.

Tournon J (1984) Magmatismes du Mesozoique à l'Actuel en Amérique Centrale: l'exemple de Costa Rica des ophiolites aux andésites. Mémories Sciences Terre., Univ. Pierre et Marie Curie, Paris, Thesis, 355 pp.

Turner JS, Campbell IH (1986) Convection and mixing in magma chambers. Earth-Sci. Rev. 23: 255-352.

Valentine GA, Wohletz KH, Kieffer SW (1992) Effects of topography on facies and compositional zonation in caldera-related ignimbrites. GSA Bulletin 104: 154-165.

Walker JA, Carr MJ, Feigenson MD, Kalamarides RI (1990) The petrogenetic significance of interstratigied high-and low-Ti basalts in centeral Nicaragua. J. Petrol. 31/5: 1141-1164.

Wiebe RA (1994) Silicic magma chambers as traps for basaltic magmas: The Cadillac Mountain Intrusive Complex, Mount Desert Island, Maine: J. Geol. 102: 423-437.

Williams H (1952) Volcanic history of the Meseta Central occidental, Costa Rica. Univ. Calif. Publ. Geol. Sci. 29: 21-46.

Wolf MB, Wyllie PJ (1994) Dehydration-melting of amphibolite at 10kbar: effects of temeprature and time. Cont. Min. Pet. 115: 369-383.

Woodhead J, Eggins S, Gamble J (1993) High field strength and transition elemen systematics in island arc and back-arc basin basalts: evidence for multi-phase melt extraction and a depleted mantle wedge. Earth Planet. Sci. Lett. 114: 491-504.

Woohead J, Johnson R. (1993) Isotopic and trace-element profiles across the New Britain island arc, Papua New Guinea. Cont. Min. Pet. 113: 479-491.

Wright TL, Doherty PC (1970) A linear programming and least squares compter method for solving petrologic mixing problems. Bull. Geol. Soc. Amer. 81: 1995-2000.